Title

The seismic signature of fractures and faults: low-frequency shear anelasticity measurements toward determining stress and frictional conditions of reservoir fractures in situ

Permalink

https://escholarship.org/uc/item/2128c25k

Author

Saltiel, Seth

Publication Date

2017

Peer reviewed|Thesis/dissertation

The seismic signature of fractures and faults: low-frequency shear anelasticity measurements toward determining stress and frictional conditions of reservoir fractures *in situ*

By

Seth A Saltiel

A dissertation submitted in partial satisfaction of the
requirements for the degree of
Doctor of Philosophy
in
Earth and Planetary Science
in the
Graduate Division
of the
University of California, Berkeley

Committee in charge:
Professor Bruce Buffett, Chair
Professor Kurt Cuffey
Professor Roland Burgmann
Dr. Jonathan Ajo-Franklin

Fall 2017

The seismic signature of fractures and faults: low-frequency shear anelasticity measurements toward determining stress and frictional conditions of reservoir fractures *in situ*

Abstract

The seismic signature of fractures and faults: low-frequency shear anelasticity

measurements toward determining stress and frictional conditions of reservoir fractures *in*

situ

by

Seth A Saltiel

Doctor of Philosophy in Earth and Planetary Science

University of California, Berkeley

Professor Bruce Buffett, Chair

Stress conditions, asperity geometry, and frictional properties affect the propagation of high amplitude seismic waves across rock fractures and faults. Laboratory evidence suggests that these properties can be measured in active seismic surveys, potentially offering a route to characterizing these important fracture properties *in situ*. To improve geophysical constraints on the mechanical state of fractures, we modified a unique seismic-frequency (~0.1 - 100 Hz) apparatus to also include key environmental controls (high strain amplitude and low effective stress). By measuring the modulus and attenuation of numerous rocks before and after tensile fracturing under a range of normal stresses (from 0.25 to 15 MPa), we were able to estimate the seismic detectability of fractures under equivalent effective stress conditions, and show that even well-mated fractures could be monitored with repeatable seismic sources. Utilizing a novel pressure sensitive film technique, we mapped the normal stress distribution on the fracture surface asperities, providing the ability to characterize the contact geometry and estimate the real contact area for each applied normal stress. This is crucial information for understanding and modeling the shear mechanics, which is influenced by surface geometry effects. Connecting past work from the rock physics, nonlinear elasticity, and fault friction communities; we suggest seismic field measurements of strain-dependent softening and frictional attenuation across fractures or faults can constrain their *in situ* frictional properties. By measuring how the rock fractures' moduli decrease and attenuation increase with strain amplitude, we inverted for the effective asperity area (consistent with real contact area measurements) and friction coefficient using a simple partial slip model. This model can also be extrapolated to fully sliding asperities, predicting the conditions for failure or the critical slip distance in rate-and-state friction. Since these measurements are made using oscillating shear stresses over a range of frequencies, they also contain information about the dynamic, strain-rate dependent frictional response. In fact, measured strain oscillations show strong nonlinearity due to the transition from static to

dynamic friction on the sliding regions of the fracture surface. Although rate-and-state friction is commonly used to model fault dynamic friction, this formulation is not capable of capturing the reversal of slip observed over the strain oscillations. In order to overcome this difficulty, we used another frictional parameterization, with a similar state variable structure, based on the Dahl model, common in the engineering community. We inverted the model to fit the time-series and frequency dependent behavior, showing that high amplitude shear wave data could provide information on velocity strengthening or weakening behavior of faults and fractures *in situ*. This is particularly exciting because these properties determine whether a fault is expected to slide stably or fail seismically in an earthquake. Our lab measurements show the promise of a field technique to map spatial and temporal heterogeneity in the conditions of failure and the frictional properties determining the behavior during these events, vital information for informing fault modeling and seismic hazard assessment.

Contents:

Acknowledgements:

I had many people advise me in different ways, which were all vital for the completion of this dissertation, but I had three specific advisors who really made my success possible. First, I would like to thank Dr. Jonathan Ajo-Franklin for his continued support, in many forms. He was an essential contributor, scientifically, technically, financially, and in many other ways. Brian Bonner also played a large role. He developed the TorQue apparatus, which is the centerpiece of this work. I am indebted to him for his deep knowledge of the scientific / technical literature, endless wisdom on all things experimental, and his varied personal contacts. He was also a constant source of optimism, without which I would never have completed this work. Lastly, Prof. Bruce Buffett was an ideal academic advisor, always supportive and contributed greatly to this dissertation with his teaching, scientific expertise, writing and presentation suggestions, and general openness. I have really appreciated his availability and willingness to support me in my varied interests and goals, even as they have changed over the last 6 years.

My other committee members were also vital to my success. Prof. Kurt Cuffey was an important source for many discussions scientific and otherwise, always a good sounding board for ideas. His courses, especially in the field, were very important for my scientific development and motivation. Prof. Roland Burgmann and his group were great for receiving feedback on my work and presentations. I have learned much from him, in his course lectures, but also his contributions as a graduate student advisor and member of the Earth and Planetary Science department and Berkeley Seismology Lab.

I would like to thank many other professors who had an important role in my education through courses, advising, and general discussions, in particular Profs. Michael Manga, Rudy Wenk, and Raymond Jeanloz. I also gained much from discussions and technical help from Prof. Steven Glaser and his group, in particular Dr. Paul Selvadurai, who in addition to his direct contributions to this work was vital for many useful discussions about a range of topics related to my dissertation.

Much technical and scientific help was obtained at Lawrence Berkeley National Laboratory, especially from Seiji Nakagawa, Paul Cook, Marco Voltolini, Shan Dou, Jil Geller, Larry Hutchings, Bill Foxall, Yves Guglielmi, Kurt Nihei, Ernie Majer, Tom Daley, Tim Kneafsey, and many more. I am grateful for the administrative and computational support at LBNL and EPS, including Margie Winn, Sara Hefty, Tracy Bigelow, Karen Elliot, Bryan Taylor, and Charley Paffenbarger.

Outside of Berkeley, I received much help and encouragement from the Nonlinear Elasticity of Materials community, including Dr. Paul Johnson, Prof. Robert Guyer, and Dr. T.J. Ulrich, whose ICNEM conferences and summer school were an important part of

1. INTRODUCTION

There is increasing interest in identifying and characterizing fractures (both natural and engineered) in reservoirs, particularly when fractures are the dominant form of permeability [e.g., *Bear* 1972, *Haimson* 1975, *Zoback and Byerlee* 1975, *Selvadurai and Glowacki* 2008]. Most engineering efforts within fractured reservoirs (oil and natural gas extraction, enhanced geothermal systems, carbon dioxide sequestration, etc.) rely heavily on the knowledge of the reservoir permeability to conduct operations (e.g., *Streltsova* 1983]. Seismic imaging is the primary method employed to gain detailed information about reservoir structure, which includes fracture density and orientation [e.g., *Willis et al.,* 2006]. Data obtained from field surveys must be interpreted within the framework of empirical relationships developed from laboratory tests on reservoir cores and informed by our theoretical understanding of rock elasticity and seismic wave propagation [*Mavko et al.,* 1998]. It is important to undertake a range of laboratory experiments to isolate the reservoir processes to be monitored seismically and up-scale these measurements to the conditions in the field.

The geophysical response of open fractures in the subsurface is sensitive to their mechanical state (such as stress, asperity contact area, aperture, friction coefficient, displacement, fluid or proppant-filled) [e.g., *Pyrak-Nolte* 1996]. These fractures can also be the source of observed microseismicity induced by fluid injection or production [e.g., *Rutledge and Phillips* 2003]. Active seismic time-lapse monitoring has the potential to record changes in the signature of the mechanical state with these reservoir engineering activities [e.g., *Daley et al.,* 2007] as well as stress effects on fractures within larger fault zones [e.g., *Niu et al., 2008*]. The mechanisms and seismic sensitivity must first be tested and understood in laboratory scale experiments; such findings should guide design of the next generation of field experiments as well as assist in interpretation of existing field data.

The bulk of laboratory seismic measurements are undertaken using ultrasonic measurement techniques developed over the past decades [e.g., *Birch* 1960, *Nur and Simmons,* 1969, *Winkler and Plona,* 1982, *Lockner et al.,* 1977, *Vanorio et al.,* 2002, *Vialle and Vanorio,* 2011], by propagating elastic waves of wavelength much smaller than the sample size through the specimen to measure travel time and thus wave speeds. This laboratory approach cannot be utilized at lower seismic frequencies (1-100 Hz) because the wavelengths involved are much larger than available core specimens. Resonance techniques allow lower frequencies with long, slender samples [e.g., *Birch and Bancroft,* 1938], but measurements at kilohertz frequencies usually require samples with meter dimensions [e.g., *Winkler and Nur,* 1979] unless a mass loaded resonator is used [e.g., *Cooper* 1979, *Nakagawa* 2011], and then provide data only at the fundamental resonance frequency and high harmonics [e.g., *Katahara et al.,* 1981, *McCann and Sothcott,* 2009]. Since field measurements involve averaging over the scale of a seismic wavelength it can be difficult to distinguish between heterogeneities at the range of scales of the field and lab, and those due to intrinsic dispersion effects [e.g., *Aki and Richards,* 2002, *Wu* 1982, *Pyrak-Nolte and Nolte,* 1992]. A limited number of high bandwidth low-frequency instruments exist capable of probing rocks through use of forced sub-resonance oscillation methods [e.g., *Spencer* 1981, *Jackson et al.,* 1984, *Peselnick and*

Liu, 1987, *Jackson and Paterson,* 1993, *Jackson* 2000, *Batzle et al.,* 2006, *Jackson et al.,* 2011, *Tisato and Madonna,* 2012, *Nakagawa* 2013, *Subramaniyan et al.,* 2014]. These instruments can measure elastic moduli and attenuation in the seismic frequency range to probe processes that may cause relaxation at the lower frequencies used in the field.

The potential to seismically detect frictional dissipation in cracked rocks has long been pursued [e.g., *Birch and Bancroft* 1938, *Walsh* 1966, *White* 1966]. The Kramers-Kronig relations insure that any energy dissipation, or hysteresis, causes frequency dependence in linear anelastic materials [e.g., *O'Donnell et al.,* 1981]. Cyclical loading and unloading on crack interfaces has been shown to cause amplitude dependent seismic attenuation [e.g., *Mavko* 1979]. In fact attenuation, or the inverse of quality factor (Q), was originally referred to as 'internal friction' because it was assumed that energy was frictionally dissipated within materials. Frictional attenuation has been experimentally shown for strains above about 10^{-6} [e.g., *Gordon and Davis* 1968, *McKavanagh and Stacey* 1974]. However crack friction was later discounted as a dominant source of seismic attenuation, because most seismic waves away from the source have strain below 10^{-6}, which will not induce greater than inter-atomic spacing scale (~10 nm) displacement on cracks of length less than 100 μm, a rough upper bound for the majority of crack lengths in intact rock [*Savage* 1969, *Winkler et al.,* 1979]. Frictional attenuation must be revisited as a mechanism when (1) fractures are larger (as in fractured reservoirs and tectonic settings of interest) or (2) higher amplitude seismic waves are used to probe material properties, e.g. close to the seismic source, particularly in borehole geometries. Under these conditions, friction on fracture faces may be detectable seismically, thus providing further field-scale information about interrelated fracture properties including displacement, fracture density, asperity contact area, or friction coefficient. These mechanical properties have been shown to directly relate to important hydrologic properties, in certain circumstances following universal scaling relationships [*Pyrak-Nolte and Morris* 2000, *Pyrak-Nolte and Nolte* 2016]. In this case the frequency dispersion and attenuation could be tied to the rate-dependent frictional properties of the interface.

Previous experimental studies of frictional attenuation [e.g., *Gordon and Davis* 1968, *McKavanagh and Stacey* 1974] have also found non-elliptical stress-strain hysteresis loops, called 'cusps' because they sharpen to a point at each end, are another sign of this nonlinearity observed for rocks under higher strain levels. This nonlinear hysteresis, with end-point memory, has been described using a Preisach-Mayergoyz (PM) model space of hysteretic elements that open and close at different stresses [*Guyer et al.,* 1995, *Guyer et al.,* 1997]. Nonclassical nonlinearity, which cannot be described by traditional theories of nonlinear elasticity [e.g., *Landau and Lifshitz* 1986], has been observed in a range of micro-cracked, but intact, rock types [*Rivière et al.,* 2015] and wave types [*Remillieux et al.,* 2016]. The degree of nonlinearity reported in these studies is more modest than might be expected in a large fracture with no continuous material fully bridging the sample. Assuming the physical mechanisms are similar, studying macroscopic fractures in the lab should allow evaluation of more subtle effects, such as frequency dependence, and characterize the interface geometry that determines the frictional behavior.

Few measurements have focused on the frequency (strain-rate) dependence of non-classical nonlinearity. Frequency dependency has been suggested in the difference between quasi-static and three wave mixing dynamic measurements of nonlinear parameters on sandstones and a limestone [*D'Angelo et al.,* 2008]. In the Dynamic Acousto-Elastic Testing (DAET) approach a lower frequency pump is used to induce nonlinearity while a high frequency probe detects the change in elastic constants with strain amplitude and thus the nonlinear elastic constants can be determined [*Rivière et al.,* 2013]. This method has been used on Berea sandstone to show some constants are sensitive to the frequency of the pump signal between 0.2 - 250 Hz, while others are frequency independent, suggesting at least two physical mechanisms are present in the nonlinearity [*Rivière et al.,* 2016a]. Further experiments showed that some rocks have a preferential relaxation around 0.1s - 1s, or 10 Hz - 1 Hz, which was insensitive to the amplitude of the pump or moisture in the sample [*Rivière et al.,* 2016b]. A few models have been proposed to explain, or predict, frequency or rate dependent nonlinearity [e.g., *Vakhnenko et al.,* 2005, *Gliozzi and Scalerandi* 2014, *Pecorari* 2015, *Favrie et al.,* 2015]. *Gusev and Tournat* [2005] added thermal induced transitions to a PM model space, referred to as Preisach-Arrhenius (PA) model, to explain a frequency as well as amplitude criterion for the onset of nonlinear elasticity. However little research has focused on fully characterizing or understanding the rate-dependence of potential physical mechanisms responsible for elastic nonlinearity in fractured heterogeneous solids. This is necessary to fully understand the mechanisms responsible for the nonlinearity as well as the energy dissipation. Experiments are also needed to predict the sensitivity of various seismic methods to measure these processes in the field.

Frictional behavior on rock fractures is also of fundamental interest for a range of seismic processes, from the earthquake cycle to triggered and induced seismicity. Laboratory and field data have shown precursory decreases in seismic velocity before the full range of slip events [e.g., *Niu et al.,* 2008, *Chen et al.,* 2010, *Rivet et al.,* 2011, *Scuderi et al.,* 2016]. In the lab, these elasticity changes have been attributed to creep and associated grain boundary sliding, particle rolling, and micro-cracking of the fault gouge, while dilation was negligible [*Scuderi et al.,* 2016]. However underlying precursory processes are still not well constrained or quantified. A variety of laboratory studies have characterized the rate-and-state frictional properties of fault rocks and gouge at steady state sliding conditions, after the critical slip distance has been reached [*Marone* 1998]. Unfortunately there are few experimental techniques or parameterizations for the frictional behavior at displacements less than the critical slip distance, the initiation of partial slip on the outside of the asperities before they are fully sliding [e.g., *Boitnott et al.,* 1992]. More studies of this slip regime could help in understanding these precursory signals and the physical processes occurring while the critical slip distance is reached and earthquake nucleation begins. By relating the dominance of fully slipping contacts and the critical slip distance, we measure the stress-displacement behavior of partial slip on mated rock fractures to calculate the critical slip distance using partial slip models [e.g., *Paggi et al.,* 2014, *Selvaduari and Glaser* 2015a]. This technique could be used with high strain field data to predict the approach towards the critical slip distance and thus the displacement or stress conditions at which full slip would nucleate.

Most earthquakes are shear displacements generated by unstable stick-slip in which the fault's interface transitions from static to dynamic friction [*Scholz* 2002].

Friction has been shown to increase with the logarithm of time spent under static conditions, referred to as healing [e.g., *Li et al.,* 2011]. This effect is captured by slide-hold-slide lab experiments, while most other experiments focus on constant load point velocities or velocity steps [e.g., *Marone* 1998]. Only limited laboratory work has explored periodic shear loading [*Savage and Marone* 2007] or transient dynamic stresses [*Savage and Marone* 2008, *van der Elst and Savage* 2015, *Johnson et al.,* 2016]. These experiments probe slide-slip behavior, where the periodic loading is superimposed on top of a constant positive slip velocity, so static friction or reverse slip is never reached. These studies focused on understanding dynamically triggered earthquakes [e.g., *Hill et al.,* 1991]. Earthquake triggering could provide a probe of the stress state and frictional properties of the fault [*Voisin* 2001, *Voisin* 2002]. By identifying the processes that govern dynamic triggering of frictional slip instabilities in laboratory experiments, field observations of triggered events can provide information on the *in situ* critical shear stress state proceeding earthquake failure [e.g., *Brodsky and van der Elst* 2014, *van der Elst et al.,* 2016, *Delorey et al.,* 2016, *Johnson et al.,* 2016]. In laboratory experiments, triggering was found to have a complicated dependence on the frequency of the perturbation; hence fault friction itself has a complex frequency-dependence, exhibiting a range of regimes [e.g., *Savage and Marone* 2007, *Savage and Marone* 2008, *van der Elst and Savage* 2015]. This study focuses on illuminating the frequency dependence of friction experimentally. In order to help interpret and motivate further field measurements, we measure and model the response of a mated rock fracture experiencing forced oscillations through static, zero strain-rate, friction conditions.

Various fracture and fracture network wave propagation phenomena, including tube waves, seismic focusing, interface waves, and guided waves, have been characterized in the lab and field [e.g., *Hardin et al.,* 1987, *Oliger et al.,* 2003, *Shao and Pyrak-Nolte,* 2013, *Shao et al.,* 2015, *Nakagawa et al.,* 2016]. The size and density of fractures that can be seismically imaged in the field depends on the magnitude of the elastic contrast they induce and the wavelength of the probing seismic wave, as well as survey details such as geometry, source type, energy, and repeatability [e.g., *Silver et al.,* 2007]. The detectability of fractures can be estimated based on the reflection, conversion, and transmission of seismic waves; or from the time delay a seismic wave would experience from travelling through the slower region around a fracture. *Schoenberg* [1980] derived solutions for calculating the reflection coefficients from a Linear-Slip Interface Model (LSIM) dependent on fracture specific stiffness, seismic impedance, and frequency, which have been confirmed with measurements of ultrasonic waves across fractures at varying effective stresses [*Pyrak-Nolte et al.,* 1990]. The results are frequency dependent, but were only initially verified in the ultrasonic range. Fracture stiffness, or compliance, has been measured at ultrasonic frequencies over a range of scales, fluid saturations, and pressures, shown to agree broadly with the LSIM theory [e.g., *Trimmer et al.,* 1980, *Worthington and Lubbe,* 2007, *Lubbe et al.,* 2008]. *Pyrak-Nolte and Nolte* [1992] show that frequency dependent fracture stiffness can result from the sampling of fractures with heterogeneous stiffness at a range of wavelengths, but they also point out that there could be dynamic effects, such as locking or friction. Without studying these potential dynamic effects it may be hard to separate them from scaling effects in the field.

Nakagawa [2013] measured frequency dependent normal and shear fracture stiffness in an unmated, fractured Berea sandstone sample (water-saturated and drained) under a range of confining pressures from 0.09 MPa to 1.7 MPa (with pore pressure under a weak vacuum) in the frequency range of 1 - 100 Hz. A poroelastic model was used to show that the measurements were very sensitive to partial saturation; a small amount of gas (saturation 99.5%) was needed to fit the data. To this point, there have been no fracture specific stiffness measurements of 'room-dry' or mated fractures in the field seismic frequency range in order to determine the seismic signature of narrow single fractures in the field.

Isolating single fractures in the laboratory allows quantification of fracture surfaces and thus illuminates the importance of micro-scale asperity mechanics. Surface topography studies in rock have been used to predict the stress states imposed by the interaction of rough surfaces that comprise the two sides of a fracture [*Power and Tullis,* 1991, *Brown and Scholz,* 1985, *Brown et al.,* 1986, *Candela et al.,* 2009]. *Greenwood and Williamson* [1966] were among the first to use statistical distributions of surface roughness to determine the heterogeneous distribution of normal stress along the fracture interface [see also *Hansen et al.,* 2000, *Persson et al.,* 2002, *Schmittbuhl et al.,* 2006] using the framework of Hertzian contact mechanics [*Hertz* 1882]. Variations in the normal stress field are assumed to be a function of the elastic deformation of the contacting topography as they are pressed together [*Johnson* 1985]. Understanding the heterogeneous distribution of normal stress has proved important since it can determine local shearing strength of a fracture surface in the context of contact mechanics [*Archard* 1961, *Bowden and Tabor,* 2001, *Scholz* 2002, *Afferrante et al.,* 2012, *Campana et al.,* 2011, *Pohrt and Popov,* 2012]. A better understanding of the strength heterogeneity along fracture surfaces is crucial in predicting a fracture's constitutive parameters (e.g., shear modulus) in natural settings.

Constitutive models determining how asperities form are complicated due to the self-affine nature of the fracture surface topography [*Candela et al.,* 2009, *Brodsky et al.,* 2016]; individual contacts (asperities) may form due to elastic, elasto-plastic, or fully plastic interactions [*Johnson* 1985] and depend on the length scales at which they are analyzed [*Persson* 2006]. In this study, we use pressure sensitive film [*Selvadurai and Glaser,* 2015a, *Selvadurai and Glaser,* 2015b] to empirically measure asperity contact formation as the fracture is subjected to increased normal stress. The pressure film allows us to measure changes in both the real contact area and local variations in the normal stress field as gross normal stress is varied.

We have adapted a low-frequency (0.1 - 100 Hz) sub-resonance apparatus, designed for shear modulus and attenuation measurements [*Bonner and Wannamaker* 1991a, *Bonner and Wannamaker* 1991b, *Saltiel et al.,* 2017a] to explore the seismic signature of fractures and understand the mechanics of asperity contacts under low normal stresses and a range of shear strains. Our instrument is unique in its capacity to measure low frequency seismic properties at low normal stresses, simulating 'open' fractures in shallow or high fluid pressure reservoirs, which often dominate the permeability and may be the most likely source of induced seismicity. The equivalent effective stress experienced on a fracture due to fluid pressure and overburden can be calculated using a measured or inferred Biot's coefficient [*Biot* 1941]. We present

calibration data that shows the accuracy of our instrument, as well as measurements of roughened polymethyl methacrylate (PMMA) interfaces in contact, artificially fractured granite samples (with different degrees of mating), and a fractured dolomite reservoir core (from a carbon sequestration target). The fracture surfaces are characterized with an optical profilometer and pressure sensitive film, which measures the surface topography and normal stress distribution, respectively. The combined measurements of contact formation and their shear mechanics show an exponential dependence of fractured shear modulus on real contact area. We construct a simple model which helps explain these measurements, while neglecting the more complex effects of facture finite width, asperity geometry, and interaction [*Boitnott et al.,* 1992, *Moore and Lockner,* 1995, *Yoshioka* 1997, *Misra and Huang,* 2012, *Morris* 2015].

We calculate the conditions under which these fractures should be directly detectable through seismic wave reflection and transmission. As fractures open up, decreasing modulus and Q (the inverse of attenuation), with less uniaxial load, more seismic energy will be reflected and seismic velocity will decrease causing larger travel times. Both of these effects will increase the seismic signature in the field. In this way, we estimate the normal stress dependence of seismic visibility of fractures (with different degrees of mating) in hard rock such as granite and dolomite. Although we are not measuring the direct effect of pore fluid, fracture measurements under 'room dry' conditions, where room humidity insures some adsorbed water on grain surfaces [*Clark et al.,* 1980], are important for understanding the stress dependence of seismic properties as well as simulating dry environments from compressed air [e.g., *Majer et al.,* 1997] or supercritical CO_2 injection. Dry frame properties are also important for rock physics interpretation in general, such as understanding the added effects of fluid substitution [*Mavko et al.,* 1998]. More measurements of natural fractures with pore fluid, incorporated into fracture network wave propagation models, are necessary to predict the seismic signature of increased pore pressure in fractures; expected with large volume injection of supercritical CO_2 for geologic carbon storage.

We focus on fracture measurements at the lowest normal stresses and highest strain amplitudes, just before full slip occurs on the interface. These are the conditions where our fractures initiate partial slip, with displacements at the micron scale. Quantifying the nonlinear elasticity and frictional attenuation of rock fractures allows us to obtain information about friction on fractures in the field. Making these measurements during reservoir engineering manipulations such as fluid injection will also improve our understanding of the poro-mechanical changes that lead to micro-seismicity, and help predict the stress and displacement conditions when full slip will nucleate into an earthquake. Time-series and frequency-dependent measurements of nonlinear elasticity offer the hope to interpret this signal for more frictional information from fractures *in situ*. Fitting the measurements with dynamic friction constitutive relations will help constrain the general frictional behavior of rock fractures and larger scale faults in the subsurface, providing valuable information about the potential for future seismicity.

2. METHODS AND MATERIALS

2.1 Shear modulus and attenuation apparatus

Our approach utilizes a forced torsional oscillator [e.g., *Berckhemer et al.,* 1982, *Jackson et al.,* 1984, *Gribb and Cooper,* 1998, *Jackson et al.,* 2011], operating without wave propagation and at sub-resonance conditions, to directly measure the complex shear stress and strain of solid right cylindrical rock samples (9 mm diameter with various lengths (see Table 1)). The apparatus (Figure 1), is a segmented torsional spring. One end includes a non-contact driver consisting of six electromagnets and six Nd-Fe B permanent magnets mounted on the central rotor (labeled 1. in Figure 1), which twists the entire bar of the apparatus in series from a fixed point at the other end (2). Since all the components of the apparatus are assumed elastic on the time scales of interest, the torque (and shear stress) is transmitted evenly throughout the bar's entire length and by measuring the amount (~tens of micro-radians) and timing (~tenths of a microsecond) of the twist at various locations along this bar, we can calculate the shear modulus and attenuation of the sample.
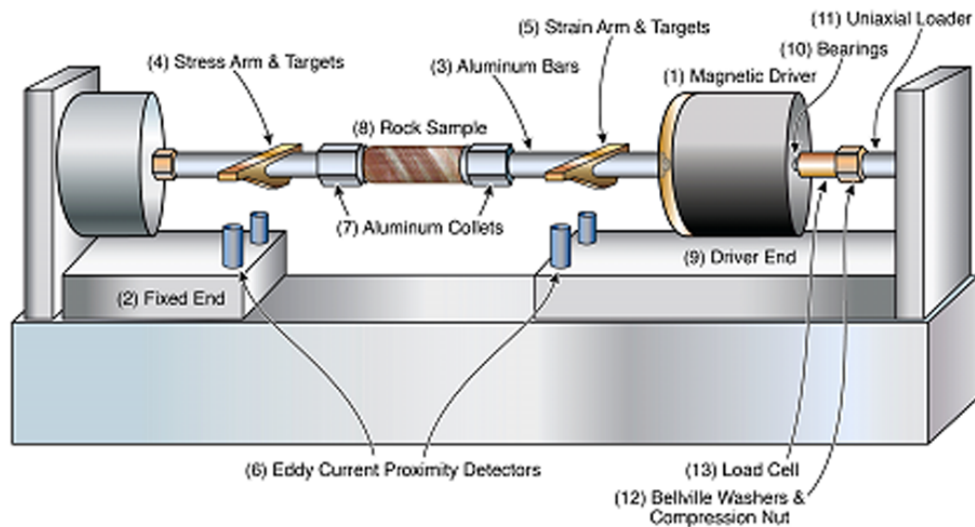
Figure 1. Schematic diagram and photograph of instrument, with parts labeled as in text: 1) Magnetic driver, without black magnetic shielding in photograph. 2) End of apparatus held fixed. 3) Aluminum bars that transmit stress, fixed end bar is hollow. 4) Arm and targets for measuring twist on fixed side of sample, calibrated to be shear stress. 5) Arm and targets for measuring twist on driver side of sample, calibrated to be shear strain. 6) Eddy current proximity detectors that measure displacement, and thus twist, of the two sets of arms and targets. 7) Aluminum collets that hold sample. 8) Fractured rock sample, aluminum in photograph. 9) Driver end that is free to twist. 10) Hardened ball bearings that limit non-torsional motion in the driver and insure purely uniaxial force from loader. 11) Uniaxial loader that applies normal stress to fractures. 12) Bellville washers expand like a spring as compression nut is tightened. 13) Load cell measures applied uniaxial stress with a calibrated strain gauge.

The magnetic driver applies a zero frequency "pre-twist" and then applies an oscillating torque around that point. This "pre-twist" allows sinusoidal oscillating torques without twisting past the neutral point, which would possible added hysteresis. The oscillator operates at frequencies between 0.01 and ~100 Hz, with the upper limit dictated by system resonances that depend on sample length and stiffness. The driver is capable of achieving strains ranging from 10^{-7} to 10^{-4}, spanning the linear and non-linear domains of the specimen.

The fixed end (2) of the apparatus is attached to a hollow section of aluminum (3) with arms and targets at each end (4) for eddy current proximity detectors (6) (Kaman Sciences KD 2300-0.5SU and KD2300-2S). The arms on both sides of the specimen allow measurement of specimen twist. The mounted arms (4, 5) are made of a carbon fiber honeycomb material, to minimize weight and maximize stiffness. The detectors (6) are configured to measure differential displacements, which depend only on the elastic deformation of the known aluminum segment (3). These sensors (6) are used to determine the shear stress being applied throughout the apparatus by the magnetic driver (1). A set of aluminum collets (7) (Acura-Flex collet chucks with straight shanks) holds the rock sample (8), attaching it in series with the aluminum bars (3) of the apparatus on each side. The twist is again measured on the driver end (5) of the sample, which captures the shear strain in the rock.

By taking a Fourier transform of the measured signals using a dynamic signal analyzer (Stanford Research Systems SR785), we can isolate the response at the driving frequency and obtain the complex shear stress and strain. Following classical anelasticity theory [*Zener* 1948, *Norwick and Berry,* 1961, *Gordon and Davis,* 1968, *Lakes* 2004], the ratio between real parts of stress and strain gives the shear modulus and the tangent of the difference in phase angles (imaginary parts) provides the shear attenuation. We process the stress-strain curves for a range of amplitudes and frequencies to calculate the shear modulus and analyze the linearity and dispersion properties of the rock samples. Signal averaging is used to improve signal to noise ratio; this is especially important for measuring phase angles accurately. All data acquisition and control functions are automated using a National Instruments LabView code, written for this instrument.

In torsion, shear strains are not uniform throughout the cylinder of rock and increase linearly with radius. The outside of the sample experiences the largest strains, thus is overrepresented in the measurements of macroscopic modulus and attenuation.

For this reason we calculate and present the maximum strain values experienced at the outside surface of the sample. As long as these maximum strains are lower than about 10^{-6}, the cross-sectional variation in strain in the sample remained in the linear regime (verified by the linear stress-strain relationship) and should not bias our results. The cylindrical geometry is also taken into account when calculating the shear stress by using the moment of inertia for a solid cylinder; see equation 1.

Un-lubricated hard bearings inside the driver (10) suppress flexural modes, ensuring we deform the samples purely in torsion. There is also a uniaxial loader (11), a spring-loaded fixture with another hardened ball bearing (10) at the far end of the driver that allows the application of up to 20 MPa of uniaxial stress along the centerline of the apparatus. Bellville washers and a compression nut (12) generate the restoring force, ensuring that it is linear with normal displacement. A load cell (13), including a calibrated strain gauge, measures the axial strain of a known aluminum piece, and is calibrated to provide the applied uniaxial stress. This loader provides a normal stress to close cracks oriented in the plane of the cylinder's diameter (those that most affect the torsional response). The hardened bearing (10) provides a point contact to minimize the torsional damping due to the uniaxial loading assembly, making it small compared to that of a fractured sample; use of this feature of the apparatus still raises the lower bound of attenuation we can reliably measure, which will be addressed later in the error analysis section.

We follow a specific protocol to measure each sample, before and after tensile fracturing, under a range of strain amplitudes, frequencies, and normal stresses. First the intact sample is measured without uniaxial stress at 1 Hz, gradually increasing strain amplitude from about 10^{-6} to 5×10^{-5} over 1000 measurements. This is repeated for 2, 4, 8, 16, 32, and 64 Hz to explore the sample's frequency dispersion. The protocol is then repeated with increasing applied uniaxial stresses (up to about 15 MPa). The static load is changed directly to the next value, but the DC shear stress is removed while the new uniaxial load is set. The sample is then fractured using the method described below, and measured at the same uniaxial stress conditions, this time starting at the highest normal stresses and slowly decreasing normal stress until the fracture slips completely and it can no longer be measured with our method. Due to the large amount of data in the time series of thousands of oscillations, these experiments are analyzed using a Fourier Transform of the stress and strain signals, only retaining the response at the forcing frequency, the fundamental mode. This assumes that the material is relatively linear (negligible harmonic generation). To study the nonlinear and dynamic response we record the entire low-frequency time-series oscillations for each sample only at their lowest measurable normal stresses and highest shear amplitudes, where slip and frictional effects are enhanced. Graphing the stress and strain oscillations against each other provides stress-strain hysteresis loops. This time-series approach provides more information about the strain-rate dependence and allows detailed analysis of relevant frictional processes.

For perfectly linear anelastic materials, hysteresis is caused by a phase delay between the stress and the strain; the resulting hysteresis loop is an ellipse, the area of which is a measure of the energy dissipated, or the attenuation [*Zener* 1948]. These materials would have stress and strain signals only at the driving frequency, or

fundamental, since any harmonic generation of a nonlinear material will cause distortion in the shape of the hysteresis loop [*Guyer and Johnson* 2009]. In this way, the harmonic distortion and hysteresis shape are directly related to each other and the nonlinearity of the material. Harmonic distortion in electronics, as well as acoustics, is commonly measured by the Total Harmonic Distortion (THD %) [*Ramirez* 1985], we calculate it from the square root of the power of the first 4 harmonics over the square root of the power in the fundamental.

The instrument is well suited for the study of fractured rocks and nonlinearity for several reasons. The uniaxial stress assembly provides normal stress to close up fractures and slowly open them with decreasing normal load. This can simulate, using the Biot's coefficient [*Biot* 1941], important processes in fractured reservoirs such as effective stress changes from injection or production. However, our study does not directly probe matrix/fluid interactions such as Biot [*Biot* 1956] or Squirt [*Mavko and Jizba,* 1991] type effects. Our apparatus is particularly well suited for very low normal stress measurements, which is inherently difficult for other instruments that rely on confining pressure of at least 10 MPa, and jacketing, to make frictional contact with the sample [e.g., *Jackson et al.,* 2011, *Li et al.,* 2014]. The magnetic driver's range of shear stresses allows measurement under higher strains where nonlinearity is more pronounced and frictional sliding initiates on fracture surfaces. The driver can also be controlled with high precision, allowing us to bring the surfaces just to the brink of fully slipping (e.g., partial slip), while maintaining relatively small displacements. In this way, we can use the driver to induce slip or even propagate new fractures, while probing the response throughout the process. The apparatus can also be used to explore fatigue damage, by measuring how the response changes over millions of cycles. Lastly, the instrument can be adapted for different environmental controls, including temperature, humidity, and reactive fluid flow.

2.2 Calibration

The shear stress applied to a specimen was calibrated by hanging weights on a radius arm coming out from the center of the apparatus. The full range of the calibrated sensors were tested and sensor output and applied torque fit by linear least squares, $R^2 =$ 0.99. This torque was converted to a force on the periphery of the sample (at radius $r = r_0$), which was then used to calculate the shear stress by dividing by the polar moment of inertia of the sample [*Timoshenko and Goodier,* 1951]:

$$\tau = \frac{Tr_0}{J} = \frac{Tr_0}{\frac{1}{2}\pi r_0{}^4} = \frac{2T}{\pi r_0{}^3} \tag{1}$$

where τ is the shear stress (Pa), T is the torque (Nm) converted from sensor output through the calibration, r_0 is the radius of the sample (m), and J is the polar moment of inertia ($\frac{1}{2}\pi r_0{}^4$ for a solid cylinder). This equation was then used to convert the sensor output (mV) to shear stress (Pa).

The same method was used to calibrate the applied uniaxial load measurement. A purpose-built aluminum load cell was loaded in series with the apparatus, and strain measured with four electrical resistance strain gauges in a bridge configuration (Micro-Measurements EA-06-125TQ-350). The strain measurement was calibrated to determine a linear relationship between the uniaxial load and strain gauge output. The uniaxial load

was divided by the sample cross-section that it was applied over to give a stress value (MPa). The linear relationship ($R^2 = 0.99$) over a range of 30 MPa was obtained by measuring the strain with a series of known weights as well as a hydraulic press with a range of 227 kg as determined with a calibrated Bourdon tube pressure gage.

A similar relationship was obtained for shear strain by calibrating the sensor output with known displacement inputs and then calculating the strain that this represents. The equation for shear strain on the periphery of the sample is [*Timoshenko and Goodier,* 1951]:

$$\varepsilon = \frac{d}{L} = \frac{\gamma r_0}{L} \tag{2}$$

where ε is the shear strain, d is the displacement (m) at the outside end of the sample converted from the sensor output, γ is the angular twist (radian) at the free end of the sample, and L is the 'active' length (m) of the sample that is being measured. This calibration has to take into account the strain in the apparatus itself, which was subtracted to isolate the strain in the sample. We obtained the strain offset due to the instrument by comparing the measurement of two T6 6061 aluminum samples of different lengths (19.3 and 38.1 mm). Assuming that the shear strain is linearly proportional to the length of the sample, we calculated the strain of a zero length sample as a function of applied stress. This is also a linear function, which provided the amount of strain that is subtracted for a given stress. We calculated this relationship for datasets at different frequencies, but it varies little over the instrument's frequency range (since aluminum is not highly dispersive), so we used a single slope for simplicity. Using these two relationships, we converted our proximity sensor voltages to the absolute measures of shear stress (Pa) and strain (unitless), the ratio of which gives the shear modulus (G) in GPa [*Timoshenko and Goodier,* 1951]:

$$G = \frac{\tau}{\varepsilon} = \frac{2TL}{\gamma \pi r_0^4} \tag{3}$$

Attenuation was determined by the phase lag between torque and twist [*Gordon and Davis,* 1968], which is independent of sample size. Using the small angle approximation, we directly took the phase delay (in radians), instead of the tangent of the phase delay, between stress and strain signals at the oscillating frequency as the attenuation in the sample. There is attenuation in the instrument (system Q), but this represents the minimum attenuation measurable, while most attenuating rock samples are well above these values, particularly at low normal stress states. We obtained an estimate of this minimum attenuation by measuring a low attenuation sample, aluminum alloy 6061-T6 (for reference Q of another aluminum alloy 24ST was measured as 2.5×10^5 at 840 Hz by *Zemanek and Rudnick* [1961]). We found that the instrument attenuation was higher at low frequencies (< 2 Hz), because of low frequency electronic drift and 1/f noise, as well as at low strains (< 10^{-6}), where the signal to noise ratio was poorer. Even for those measurements, the system phase delay was less than 0.001 radians (Q equals 1000). This is at least an order of magnitude less than rock attenuation values for samples of interest, particularly for fractured rocks.

2.3 Error analysis

There are two different sources of error in our measurements, random error in the measurements themselves due to electrical and numerical noise, and systematic errors from imperfect calibration. We minimize the electrical and numerical noise by taking 1000 repeated measurements at each stress condition with all of the samples. Each source of systematic error has also been quantified and compared to the variance in the measurements. We choose to give error bars based on the standard deviation, because this gives a better comparison between our measurements of the same rock sample under different stress conditions.

Repeated measurements of modulus and attenuation both follow a normal distribution, as evaluated by the Anderson Darling Test [*Anderson and Darling,* 1954] (see Figure 2 for histograms of repeated modulus and attenuation measurements). Modulus has a significantly smaller standard deviation than attenuation, as a percentage of the value. The standard error on the median of these distributions decrease with the square root of the number of samples taken, improving the reproducibility of our measurements by taking 1000 samples at each frequency; this is especially important for the attenuation measurement. This number was chosen because standard deviation appears to asymptote at about 1000 measurements. These measurements cover a range of amplitudes and aid in assessing the linearity of the stress-strain curves. The linear least squares method gives an error on the slope for each line in our calibration; by propagating this error we can see the relative effect of each source on the measurement of shear modulus made using equation 3.
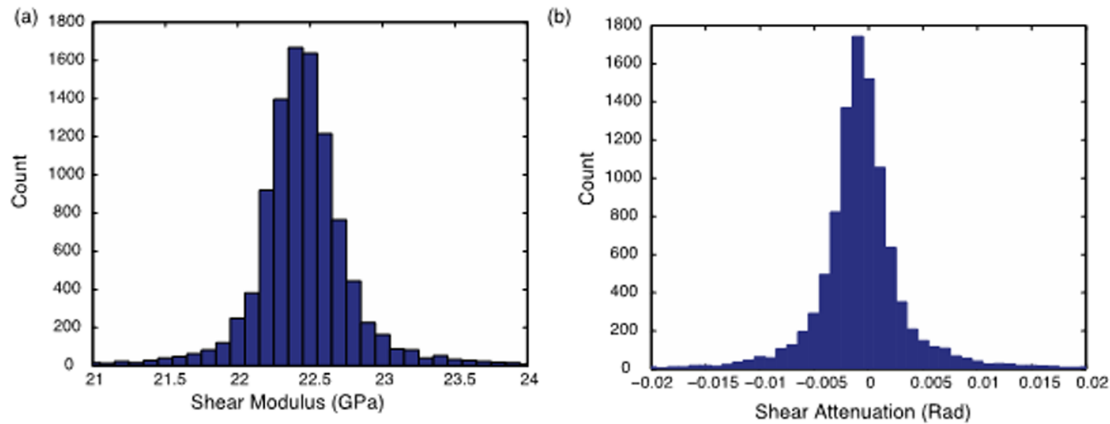

Figure 2. Histograms show the normal distribution of 10,000 repeated measurements for aluminum alloy 6061-T6 of a) shear modulus and b) attenuation. These measurements were made at 8 Hz and under 5 MPa of uniaxial stress. Bins of attenuation histogram are limited by rounding error in the signal analyzer and the modulus bins were chosen to roughly match the count at the mean value. Error bars in Figures 3, 4, 6, 8, 10 and 13 are taken as the standard deviation of deviation of these normal distributions, but with only 1000 repeated measurements.

The hanging weight calibration of shear stress was performed nine times to improve the statistics and contributes a ±0.104% error to the shear modulus. The strain sensors were calibrated with a purpose-made micrometer, which moves the eddy current sensor in known increments relative to a metal target, and contributed ±0.062% to the

modulus error. Both of these errors (together ±0.166%) can be improved by making repeated measurements, but the error due to measurement of the active length L of the calibration sample is more difficult to minimize. The sample was held by tightened aluminum collets and the active length L was the part of the sample that is actively deforming, which can differ slightly each time the sample is loaded due differences in how far it sat in the collets. To minimize this source of error, the sample was only unloaded and reloaded when necessary, such as for fracturing. We measured the active length by marking where the sample fits in the collets while it was loaded, and then measuring the deforming length of the sample between the collets after the sample was removed. There is some added uncertainty in the active length due to edge effects, it has been suggested that the effective length is less than the distance between clamping points [*Cooper* 1979]. Given these difficulties we estimate 93.4% accuracy in measuring the "active length" of the smallest calibration samples (error of ±0.127 cm from a length of 1.93 cm), which propagates to 6.6% error in the calculation of modulus for these smallest samples (the error is much smaller as a percentage for the longer samples). The measurement of "active length" is also a part of the zero length offset calculation, but only contributes a ~3% error to the modulus through this calibration.

Another source of systematic error are the collets. We are careful to tighten the collets to the same torque with every loading. If they are not sufficiently tightened the sample will slip within the collet, which is immediately apparent in the amount of strain recorded. If the collets are tightened too much they will potentially open microcracks, or create a through going fracture, in the rock sample, also apparent in the measurements. For all of these reasons it is crucial that the loading is done very carefully and as infrequently as possible. There are further environmental sources of variability, such as humidity and temperature changes, which are only partially controlled in our laboratory environment, and are included in the variability of the 1000 measurements over ~1.5 hours that we average.

2.4 Surface characterization

To better understand the micromechanics of our fracture surfaces and how they change with normal stress, we employed a novel stress distribution imaging technique [*Selvadurai and Glaser,* 2015b]. A Fujifilm prescale® medium range (12-50 MPa) pressure sensitive film measured the contacting asperities formed between the interacting surfaces under a range of applied normal stresses. The pressure sensitive film is polyethylene-based and has a thickness of approximately 90 μm. The film has embedded microcapsules, which have a spatial resolution and were digitized to 20 μm x 20 μm. When compressed the capsules crush and release ink with colors proportional to the applied pressure (~ 1.5 Pa resolution). According to the manufacturer the film used in this study is rated for normal pressures between 12 to 50 MPa, and has been validated independently by *Selvadurai and Glaser* [2015b] using a spherical indentation test. The pressure film is first placed between the fracture surfaces and compressed between the samples where it develops for a period of ~ 120 s. A specialized jig was constructed to ensure the repeatability of the pressure film measurements. Characterizing the fracture using the pressure film involved squeezing the film between the fracture surfaces under known uniaxial loads.

The pressure film offered a 'one-time' estimate of the maximum normal stress – once a microcapsule becomes discolored it does not return to its original state. For this reason, a new piece of pressure film is employed to characterize the interface for each level of uniaxial loads. No shear stress (i.e. torque) was applied during compression since we are not interested in film-mediated sliding. The pressure film measures the same asperity configuration as our shear measurements, where the equivalent uniaxial load is applied to press together the mated surfaces before any torque is applied.

After loading, the film was removed and optically digitized using an image scanner (MUSTEK ScanExpress A3 USB 2400 Pro Scanner). Algorithms in MATLAB were created to isolate, size and catalogue all contacting asperities in the static state. The light intensity of each microcapsule was converted to normal stress (σ_{pix}) using the calibration curve documented in *Selvadurai and Glaser* [2015b]. Once the image was converted to stress estimates, a lower threshold contact stress value was obtained in an iterative manner [*Selvadurai and Glaser,* 2012, 2015a]. We assumed that the contact occurred only along the *r-Θ* plane (see Figure 12a) and that the force on each pixel was exactly perpendicular to the plane of the fracture (i.e. *z*-direction). For all pixels experiencing stresses above the threshold, a total reactive force F_r was calculated (i.e., measured stress on pixel multiplied by the area of a pixel). The threshold was then varied iteratively until F_r balanced the applied far-field uniaxial load, i.e., $F_r = F_n = \pi r_0^2 \sigma_0$. With the threshold determined, we were able to accurately measure the asperity contact area and normal stress, including mapping of the actual size, shape, and spatial distributions observed over the entire fracture surface [*Selvadurai and Glaser,* 2013].

For geometric comparison, surface topography was also directly measured using an optical scanning profilometer (Nanovea PS50/3000μm optical pen). The spatial resolution in the *r-Θ* plane was 50 μm along the fracture surface and 0.5 μm in height. The surface topography of the fractures varies significantly between our samples, depending on grain size and fracturing method, and the scans are useful for characterizing the tilt of the fracture and surface roughness. A profile across the center of the sample diameter is used to describe the topographic trend of the surface (either tilted, bowed, or with multiple ridges/valleys), as well as a sense of the surface roughness (Figure 3). These profilometer images are not in the same orientation as the film images shown below. While the initial contact conditions measured from the pressure sensitive film should ultimately determine the physical properties of the fracture (e.g. shear stiffness [*Berthoude and Baumberger,* 1999]), the surface topographies were measured to provide a better understanding of the fracture and help validate some of the assumptions made when employing the pressure sensitive film.
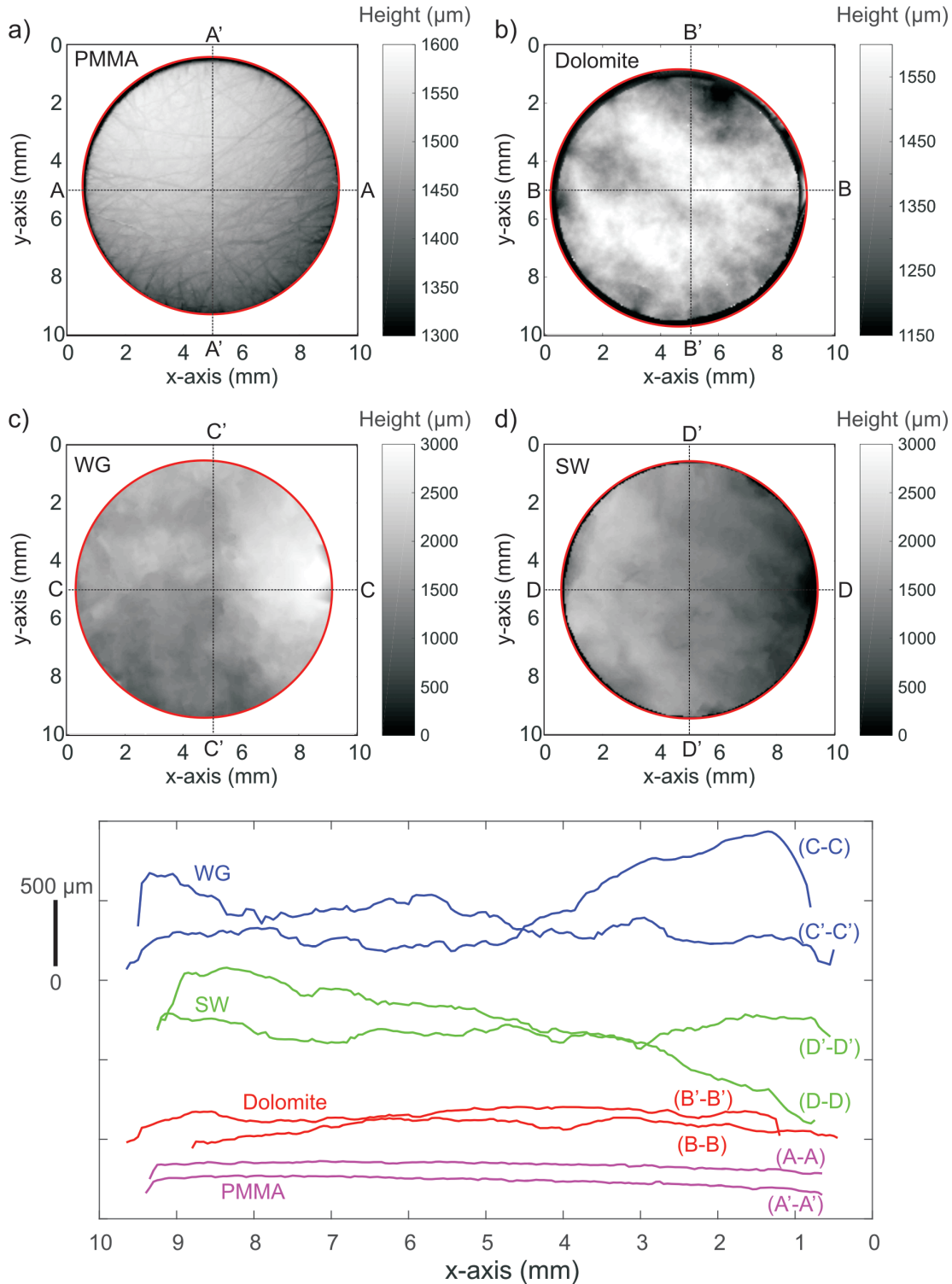
Figure 3. Optical profilometry measurements of surface topography of a) PMMA, b) Duperow dolomite, c) Westerly granite (WG), and d) Sierra White (SW) granite samples. e) The roughness profiles of the perpendicular centerlines of each sample as marked on topography images, sample surfaces have decreasing roughness from top to bottom.

2.5 Comparison of standards

We compare our measured modulus values with those obtained by ultrasonic pulse transmission method for intact samples of aluminum, polymethyl methacrylate (PMMA or acrylic), ABS plastic, Duperow dolomite, and Westerly, Sierra White, and Montello granites (Table 1). Ultrasonic tests were conducted using 5 MHz shear wave transducers (Panametrics V155), minimal manual contact pressure and ultrasonic couplant, and subtracting the 'face to face' piezoelectric rise time. The ultrasonic waves were shot across the diameter of the cylindrical samples, the transducers in line contact with the sample, to avoid TI anisotropy in aluminum from the extrusion process, which the torsional measurements average. The moduli measured at low frequencies are systematically lower than at ultrasonic frequency for the more attenuating samples, which also show some dispersion within the frequency range of our apparatus. PMMA has well known dispersion due to unwinding of complex polymer chains [*Ferry* 1980], while 'room-dry' rocks and metals can show dispersion from adsorbed water or other viscous/frictional regions on microcracks or grain surfaces [*Zener* 1948, *Cooper* 1979]. In contrast aluminum 6061-T6 shows no difference within the error bars between measurements at different frequencies, since it has negligible attenuation as discussed in the calibration section above. The difference in modulus between measurement techniques is likely due to a combination of these dispersion characteristics of each material and the added importance of the outside of the sample in our measurements, due to the torsional configuration's increased peripheral strains determined with equation 2. The outside rind of the sample is likely to have a lower modulus than the sample in bulk because of open micro-cracks generated during the coring process, these cracks are likely to be open because all of these comparison measurements were made without uniaxial load. Our 'room-dry', atmospheric pressure, low-frequency shear modulus measurements of Westerly granite, 17-19 GPa, are consistent with the scarse available literature data of comparable conditions. *Cooper* [1979] measured the torsional resonance at frequencies between 0.649 and 0.685 Hz, giving shear moduli of 16-18 GPa, in different directions to show its slight anisotropy. *Simmons and Brace* [1965] found even larger (~50%) discrepancies beyond the expected error between dynamic and static measurements at atmospheric pressure, attributing them to open cracks that effect strain gauge measurements across the entire sample more than ultrasonic wave propagation, which may bypass cracks.

Standard Sample material	Literature dynamic shear modulus (GPa)	Ultrasonic (5 MHz) shear modulus (GPa)	64 Hz shear modulus (GPa)	8 Hz shear modulus (GPa)	1 Hz shear modulus (GPa)	Active length (mm) in our apparatus
Aluminum 6061-T6	24 ± 0.48 [1]; 26.2 [2]	26.520 ± 1.615	25.704 ± 0.208	25.316 ± 0.170	25.154 ± 0.454	38.1 ± 1.27
PMMA	2.16 [3]; 2.24 [4]	2.328 ± 0.142	1.430 ± 0.033	1.294 ± 0.020	1.1148 ± 0.034	58 ± 1.27
Westerly Granite	33.42 [5]; 20. ± 0.4 [6]	23.284 ± 1.418	18.947 ± 0.270	17.783 ± 0.289	16.949 ± 0.180	34 ± 1.27
Sierra White Granite		22.723 ± 1.384	16.938 ± 0.098	15.926 ± 0.112	15.103 ± 0.262	15 ± 1.27
Duperow Dolomite		29.967 ± 1.825	16.749 ± 0.361	15.851 ± 0.238	15.354 ± 0.613	25.8 ± 1.27
Montello Granite		35.888 ± 2.186	31.028 ± 0.547	30.298 ± 0.325	29.917 ± 0.692	34.8 ± 1.27

Citations: [1] *Carnevale et al.,* [1964] at 1 MHz; [2] *Oberg et al.,* [2008]; [3] *Capodagli and Lakes,* [2008] at 200 kHz; [4] *Nakagawa* [2011] at 280-450 kHz; [5] *Schock et al.,* [1974]; [6] *Simmons and Brace,* [1965]

Table 1. Comparison of standards shear moduli measured and from literature at ultrasonic and seismic frequencies, all measurements were performed with no confining pressure or uniaxial load.

We found that PMMA provides the best low-frequency standard when compared to published modulus and attenuation results from a range of historic and modern systems [*Nakagawa* 2011, *Capodagli and Lakes,* 2008, *Tisato and Madonna,* 2012, *Yee and Takemori,* 1982, *Koppelmann* 1958]. Although this material often varies in absolute mechanical properties from batch to batch due to variable fabrication procedures, the overall frequency dispersion characteristics of the material are fairly reproducible between batches. In Figure 4, we compare our measurements of PMMA to those published by other low frequency or wide-bandwidth instruments. Noting that absolute shear moduli of PMMA can vary significantly between batches, the similarities in the dispersion characteristics we measure with those measured in the literature provide confirmation of our system and calibration protocol.
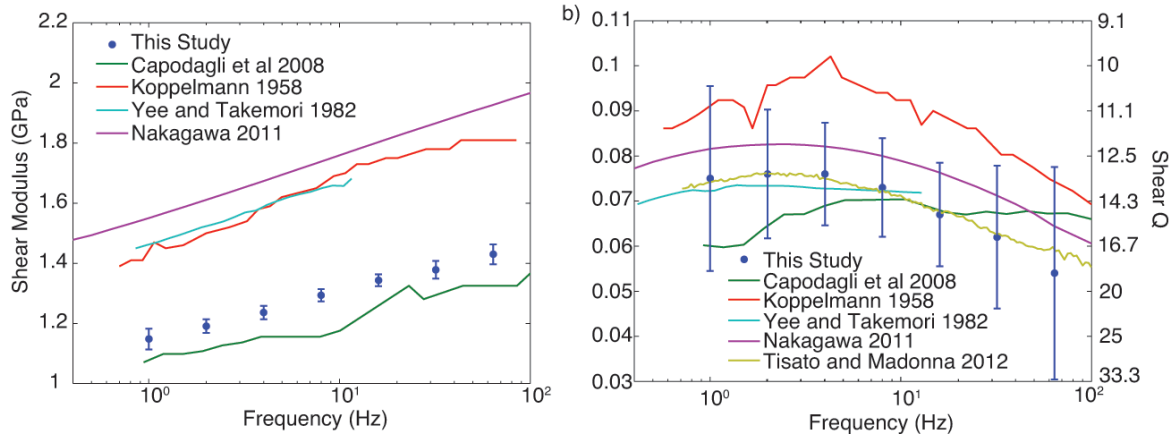
Figure 4. Measured frequency dependence of PMMA compared to published values, batch to batch differences are expected but dispersion is consistent. Error bars are calculated by standard deviation of 1000 measurements at each frequency. a) Shear modulus with logarithmic frequency scale. b) Shear attenuation with logarithmic frequency scale.

2.6 Fracturing technique

We employed a custom machined holder to created a tensile fracture across the diameter of the sample. The holder has twelve sharpened screws positioned into a groove carved around the periphery of the sample. As the screws are slowly tightened evenly around the diameter they force open a tensile fracture that remains perpendicular to the diameter of the cylindrical sample. This results in a well-mated tensile fracture with relatively smooth and low topography (Figures 3 and 5). No visible material was lost during fracturing from the dolomite and granite samples, but the rhyolite sample lost a section about a sixth of the cross-sectional surface area, as seen by the depression on the upper-left of the topography (Figure 5a). The loss of this material in the rhyolite sample is likely due to microcracks from the process zone reaching the fracture surface [*Moore and Lockner* 1995]. The rhyolite may have larger microcracks due to its brittle nature or the cracks may be more likely to reach the surface due to its smaller grain size. Optical profilometry and pressure sensitive film [*Selvadurai and Glaser* 2015b] were used to characterize fracture surfaces.
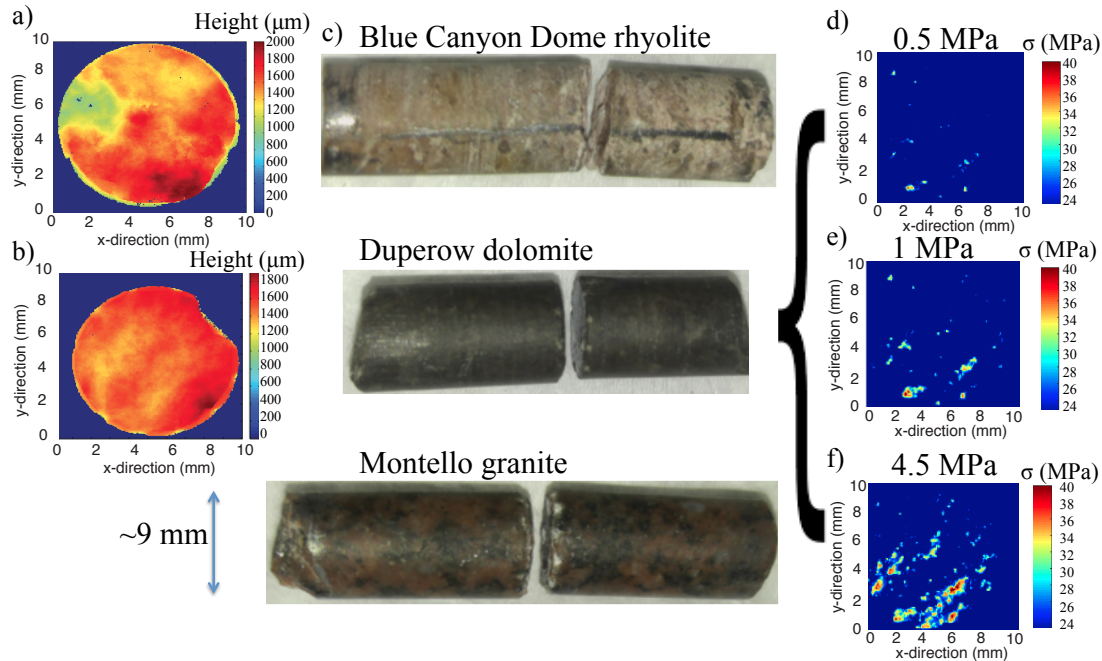
Figure 5. Characterization of fracture surfaces shows tensile fracturing created a relatively flat face across the sample. Optical profilometry of surface topography of **a)** Blue Canyon Dome rhyolite and **b)** Duperow dolomite. **c)** Photos of each fractured sample, on the same scale, each has a diameter of about 9 mm and slightly varying lengths. Local normal stress distribution from the calibrated pressure sensitive film are shown for the Duperow dolomite fracture under normal stresses of **d)** 0.5 MPa, **e)** 1 MPa, and **f)** 4.5 MPa.

2.7 Sample descriptions

We focused on measuring an artificially fractured dolomite (dolostone) core from the Duperow formation, a carbon sequestration target in north-central Montana. The sample was cored from the Danielson well (API 811151), at a depth of 3,337.7 feet. An adjacent plug (34B) was found to have a density of 2.716 g/cc, permeability of 0.01 mD, and porosity of 2.51% [*Spangler* 2014]. We also measured the ultrasonic P- and S-wave velocities for the plug at 5,340 ± 160 and 3,300 ± 100 m/s, respectively [*Saltiel et al.,* 2017a]. The cores, as well as preliminary surface seismic and well log data, suggest that this reservoir has relatively low matrix permeability but many open, healed, and partially healed natural fractures. Preliminary modeling [*Zhou et al.,* 2013] suggests that the pore pressure change associated with large-scale supercritical CO_2 storage would be significant and likely generate the largest seismic property alteration during proposed injection activities; existing open fractures should be the most sensitive to such increases in pore pressure. A picture of the dolomite sample and surface characterization of its artificial fracture face are shown in Figures 3 and 5.

To show the generality of the observed behavior and its dependence on rock type or surface geometry, we also tested artificial tensile fractures in Westerly, Sierra White, and Montello granites as well as Blue Canyon Dome rhyolite samples (Figure 5). Westerly is a standard granite from Rhode Island. Sierra white is a course-grained

granite from California and Montello is competent, fine-grained granite, from a quarry in Wisconsin. Westerly is one of the most commonly measured rock formations, allowing better comparisons to other studies. The existing fracture in our Sierra White sample had large topography, showing the effect of a poorly mated interface. The Montello was selected because it has few microcracks, so the effect of the throughgoing fracture dominates any stress dependence from the rest of the intact rock. The Blue Canyon Dome rhyolite is a fine-grained, competent igneous rock. Our sample was cored from an experimental pilot site in central New Mexico; the site is utilized as a shallow analog for testing enhanced geothermal stimulation techniques and relevant monitoring approaches [*Knox et al.,* 2016].

3. SHEAR MECHANICS AND DETECTABILITY UNDER A RANGE OF NORMAL STRESSES

3.1 Fractured rock results

In this chapter, we document some of the first results showing the stress-dependent moduli of fractured materials at seismic frequencies and normal stress states between 0 and 16 MPa. The measurements were made at the highest normal stresses first (often approaching intact behavior), with subsequent lower stresses representing fracture opening.

Besides serving as a standard for comparing our measurements to literature values, we also used PMMA to test our ability to probe the elastic properties of fracture surfaces. To simulate a roughened fracture, the ends of our PMMA samples were sanded with P80 grit emery cloth (~ 201 micron particle size). A single piece of PMMA was used to measure the intact modulus and attenuation, shown by blue circles in Figures 6a and 6c respectively. Next, two pieces of PMMA were combined to study the roughened 'fracture' surface between them. This measurement gives the fractured shear modulus and attenuation, shown by red circles also in Figures 6a and 6c respectively. By subtracting the shear compliance, $\eta = 1/G$, of the intact sample from the shear compliance of the fractured sample at every level of uniaxial stress, using the principle of superposition for linear elasticity, we can estimate the shear compliance of the fracture itself [*Jaeger and Cook,* 1969]. In Figure 6b, we show measures of PMMA shear compliance for the intact sample (blue circles), fractured sample (red circles) and of the fracture only (green circles). Because PMMA is relatively compliant and attenuating compared to rock, the effect of the fracture is somewhat masked. The fractured sample reaches the modulus of an intact sample at high normal loads, implying a negligible compliance for the fracture itself (Figure 6b). As the fracture opens due to decreasing normal stress there is a clear effect on shear modulus (Figure 6a) and shear attenuation (Figure 6c). The frequency dispersion does not change significantly with normal stress; therefore we only graph the value at 8 Hz for each stress condition.
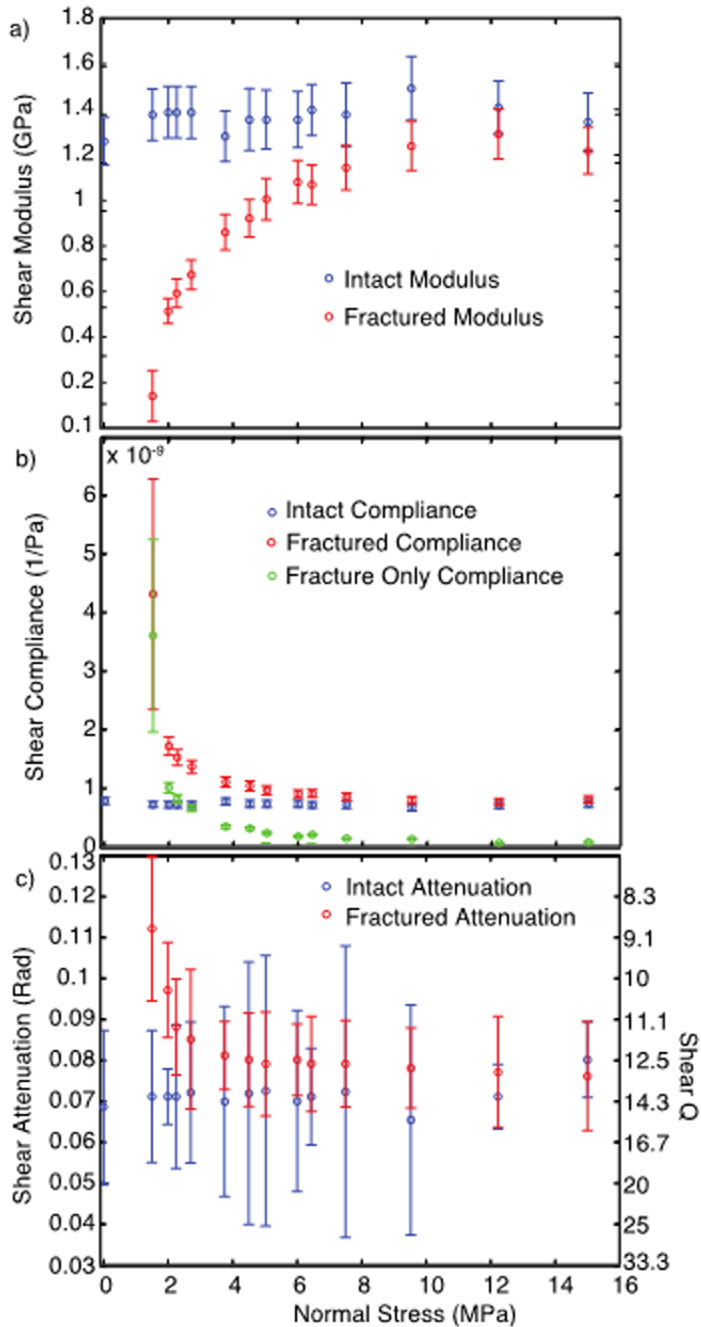
Figure 6. Fractured and intact PMMA. **a)** The shear modulus of fractured and intact samples. **b)** Measured shear compliances with calculated compliance of the fracture alone. **c)** Shear attenuation or 1/Q.

The closing and stiffening of the fracture with normal load correlates with the increase in real contact area (A_r), as calculated from the pressure film (Figure 7a). Local normal stress distribution was also measured with the film; the images for uniaxial loads from 1 to 9.5 MPa are shown in Figures 7b-f. The contact surface was dominated by the slightly beveled topography of one of the surfaces, giving a growing circular contact at the center that grows linearly with normal stress.
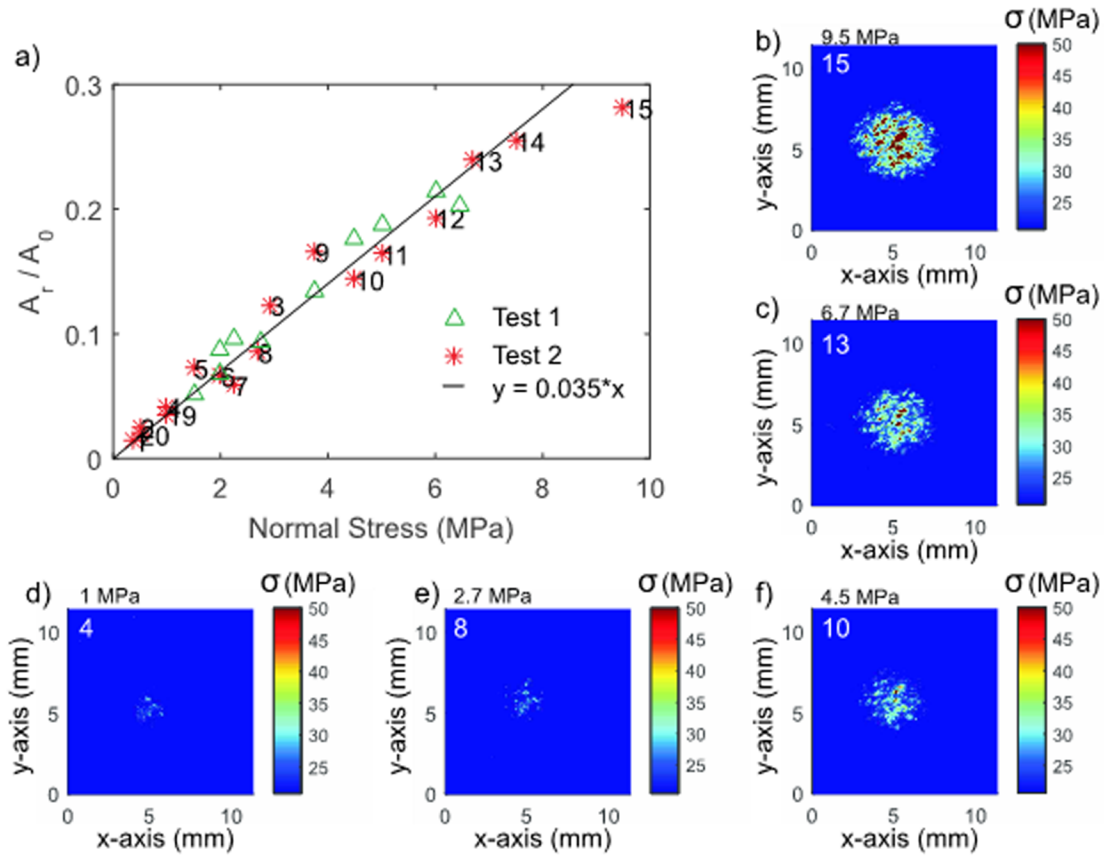
Figure 7. Pressure sensitive film measurement of PMMA. **a)** Measurements of the fractional real contact area (A_r/A_0) for each applied normal stress for two separate tests (red stars and green triangles) are shown. The data is fit with a linear relationship. The numbers correspond to individual contact measurements taken at the associated normal stress and the images are associated with test 2 (red stars). Local normal stress distribution from the calibrated pressure sensitive film are shown for normal stresses of **b)** 9.5 MPa, **c)** 6.7 MPa, **d)** 1 MPa, **e)** 2.7 MPa, and **f)** 4.5 MPa.

To investigate the behavior of a mated rock surface, we measured the properties of a Westerly granite sample before and after inducing a fracture. We first measured the intact shear modulus and attenuation of the sample, while compliance was calculated, each plotted in blue in Figures 8a, b, and c. No measurements were taken for stresses between 0 and 4 MPa while the specimen was intact because it was uncertain whether the fractured sample could be tested at such low normal stress without the fracture slipping. Low stress values for the intact sample were estimated with linear extrapolation from the higher stress measurements trend. We introduced a fracture perpendicular to the centerline of the cylindrical sample at a central location of the active length (i.e. *L*/2). The periphery of the sample was scored at a central location then a fracture was propagated using three-point bending with a hydraulic jack assembly. Although it is commonly assumed that a leading zone of microcracks initiate fracture nucleation in brittle rocks [*Reches and Lockner,* 1994], almost no material was lost from our fracture faces during the fracturing process, suggesting that the damage zone of precursor cracks

is on the order of a grain diameter in thickness. By using the same sample for intact and fractured measurements, the calculation to remove the compliance of the intact segments of the sample becomes more accurate. At lower normal stresses, the intact granite is considerably stiffer than the fracture, with a higher Q (Figures 8b and c). The granite sample also shows little change in dispersion over the range of frequencies; the reported value was measured at 8 Hz.
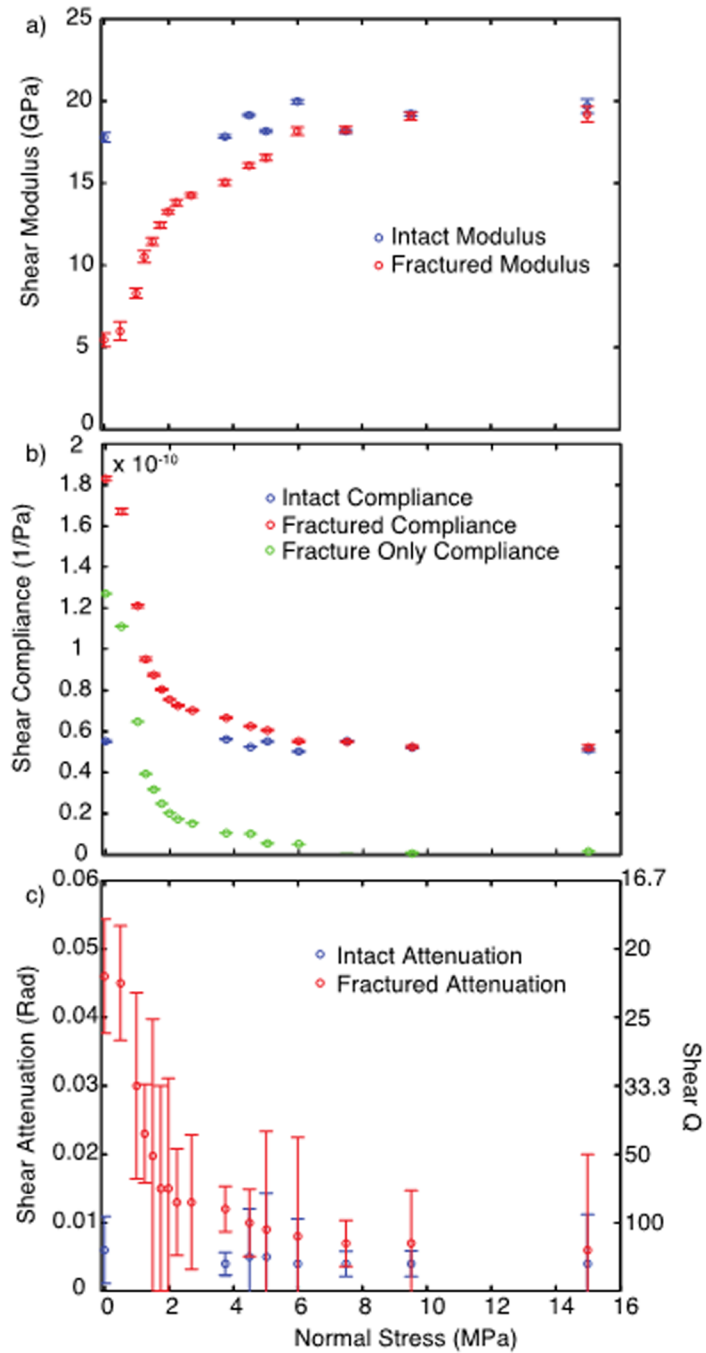
Figure 8. Westerly granite sample before and after fracture. **a)** Shear moduli. **b)** Measured shear compliance with calculated compliance of the fracture itself. **c)** Shear attenuation.

The topography of the Westerly granite surface was much rougher than the PMMA sample, due to the grain scale heterogeneity of the rock and the fracturing approach, as can be seen in the optical topography scan (Figure 3). Figure 9 shows the results from the pressure sensitive film used to characterize the Westerly granite fracture. The results are presented in a manner similar to Figure 7 that described the PMMA-PMMA interface. Figure 9a displays the relationship between the normal stress and the measured ratio of real contact area to nominal contact area (A_r / A_0). The inset images (Figures 9b-f) show processed pressure film scans that display the normal stress distributions (assuming a planar fracture) for various uniaxial stresses mentioned in the caption. The increased topography is mostly visible as a ridge along the bottom of the sample, which dominates the contact area throughout the range of normal loads measured (Figures 7b-f). This ridge provided interlocking surfaces that are not perfectly perpendicular to the cylinder, possibly translating some of the shear stress into normal stress and helping to hold the fracture together. Our induced fracture was very well-mated and reached completely clamped conditions, same shear modulus as for the intact sample, at normal stresses of 7.5 MPa (Figure 8a).
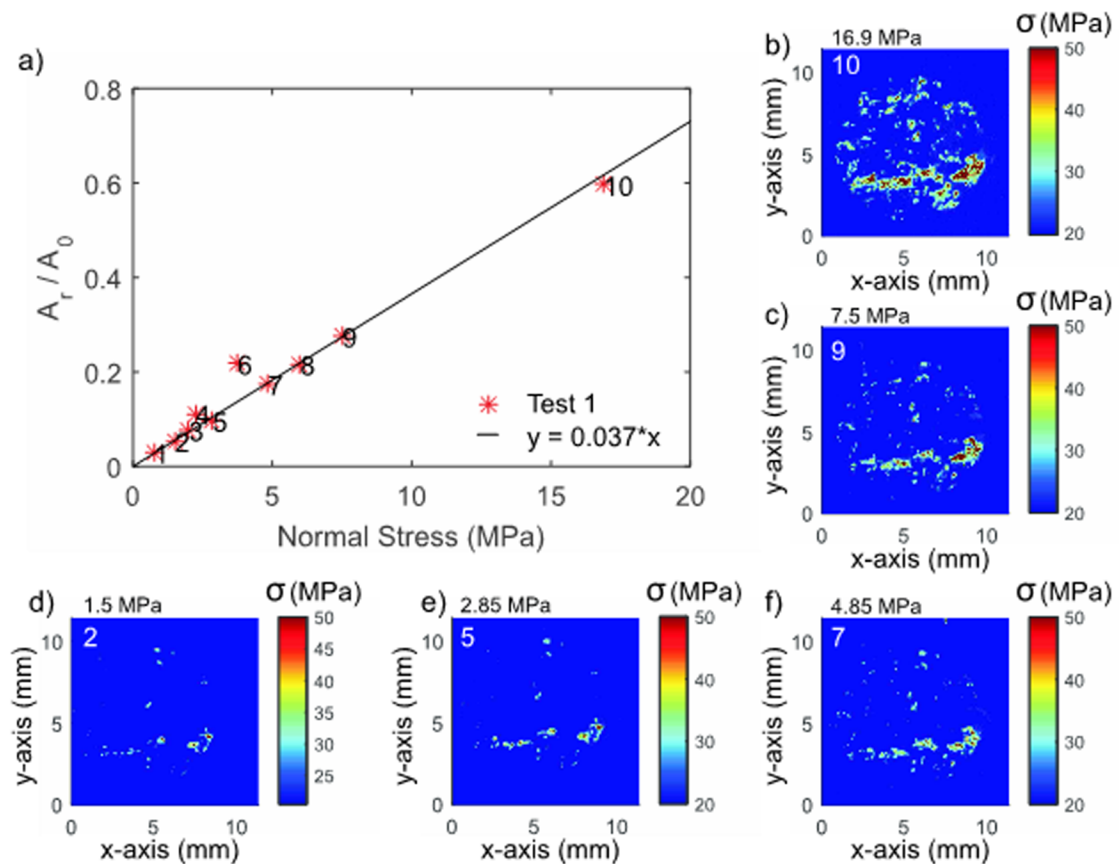

Figure 9. Pressure sensitive film measurement of Westerly granite. **a)** Fractional real contact area with each applied normal stress, fit with a linear relationship. Local normal

stress distribution from the calibrated pressure sensitive film are shown for normal stresses of **b)** 16.9 MPa, **c)** 7.5 MPa, **d)** 1.5 MPa, **e)** 2.85 MPa, and **f)** 4.85 MPa.

In contrast, we measured an existing fracture in Sierra White granite. This granite is a coarser grained (~1 mm vs ~0.2 mm), and the fracture was not as well-mated or interlocking as the induced fracture in Westerly granite. Figure 10a shows the intact values of the shear modulus (blue circles) and the fractured modulus (red circles). We see that the fracture shear modulus never recovers to the intact modulus in the experimental range of uniaxial normal stresses. Since the fracture now contributes a measurable compliance even at the highest normal loads, we now show the calculated fracture only shear modulus in green on Figure 10b. In contrast the shear attenuation for the fractured Sierra White granite does reach the intact value at high normal stress, increases gradually with lower normal stress until it increases dramatically at ~ 4 MPa, shown in Figure 10c.
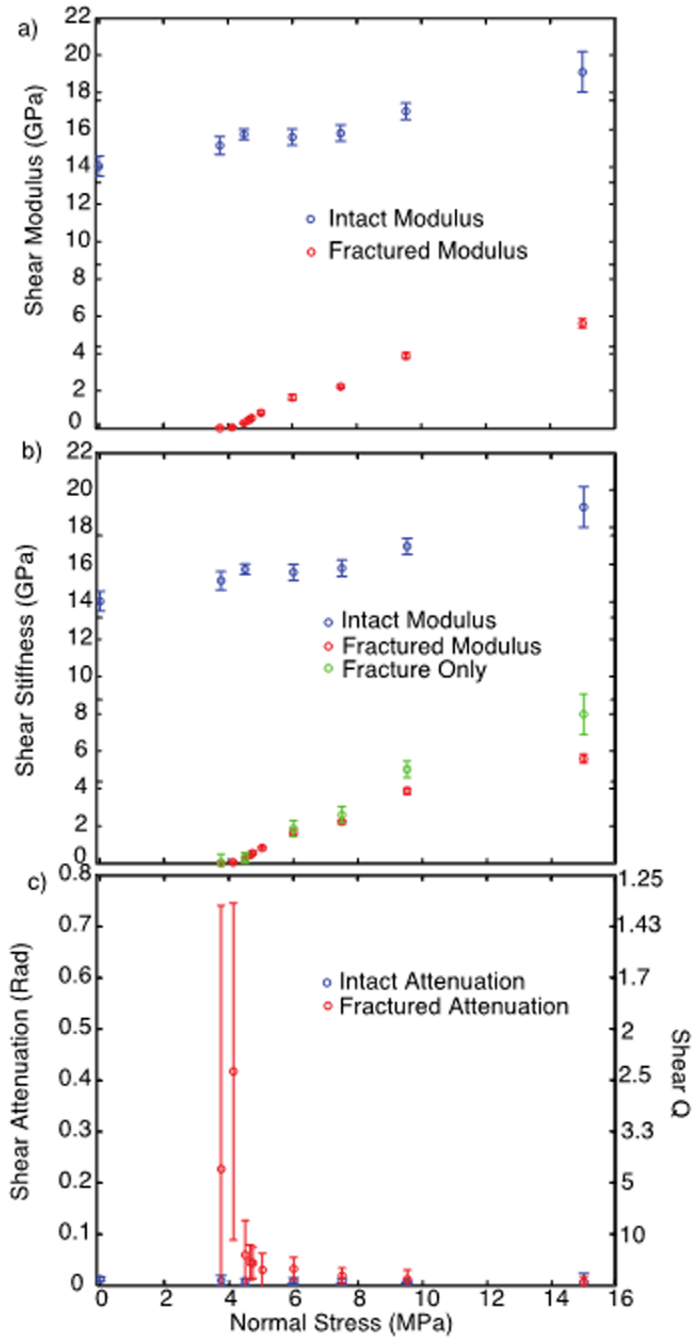
Figure 10. Fractured and intact Sierra White granite. **a)** Although the slopes look similar, the shear modulus of fractured sample increases almost twice as much with normal stress as the intact sample. **b)** Measured shear moduli with calculated modulus of the fracture itself. **c)** Shear attenuation.

The relationship between real contact area and normal stress measured from the pressure film for Sierra White granite is shown in Figure 11a and visual distributions of local normal stresses are shown in Figures 11b-f. Unlike the other samples, the Sierra White sample preferentially formed new real contact area at the center of the interface

(Figures 11b-f)) where the shear strains are lower in our testing configuration as described by equation 2, and thus have less impact on the fracture's shear modulus.

Figure 11. Pressure sensitive film measurement of Sierra White granite. **a)** Fractional real contact area with applied normal stress, fit with a linear relationship. Local normal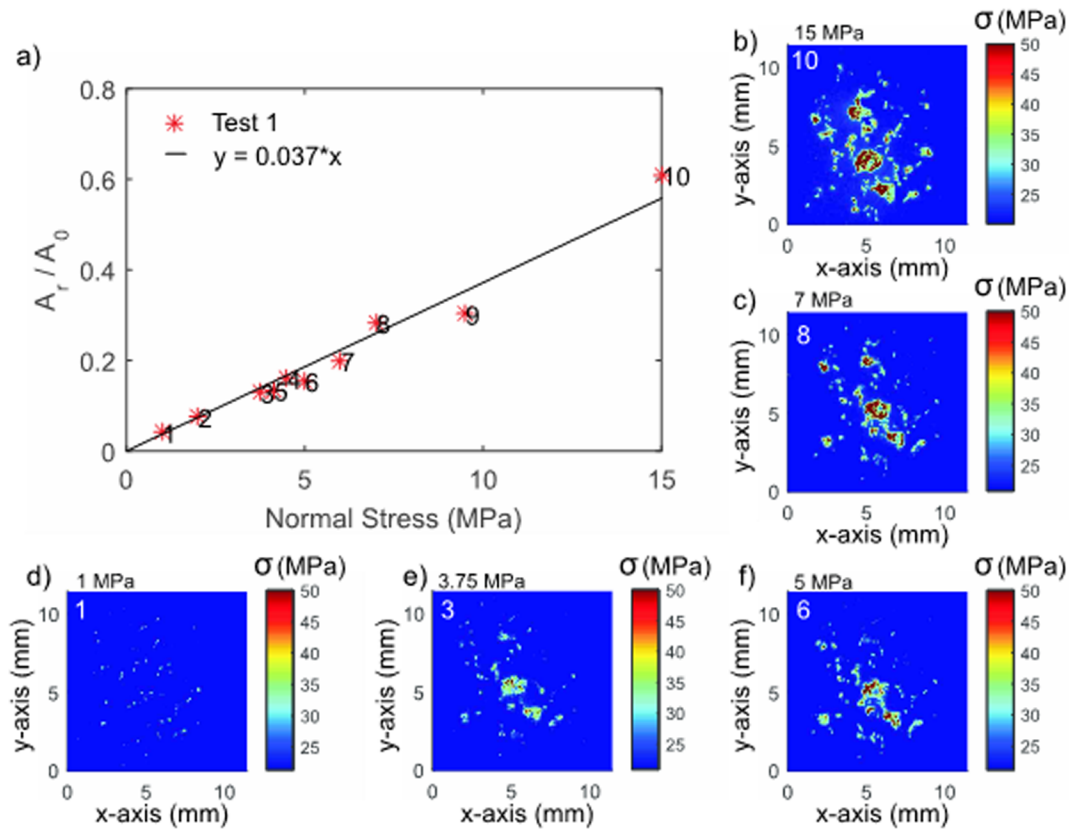 stress distribution from the calibrated pressure sensitive film are shown for normal stresses of **b)** 15 MPa, **c)** 7 MPa, **d)** 1 MPa, **e)** 3.75 MPa, and **f)** 5 MPa.

The fracturing technique for the Duperow dolomite differed from the Westerly granite. Our custom machined holder created the tensile fracture, where twelve sharpened screws are positioned into a groove carved around the diameter of the sample. As the screws were slowly tightened evenly around the diameter they forced open a tensile fracture that remained perpendicular to the diameter of the cylindrical sample. The result was a well-mated, fine-grained tensile fracture that had a smoother topography than the granite fractures created by bending (Figure 3). Studying the shear properties of the dolomite was done using the same approach as the previous samples; the intact modulus and attenuation were measured at various uniaxial loads (Figures 12a and c). The dolomite's intact, fractured, and fracture only shear compliances are presented in Figure 12b.
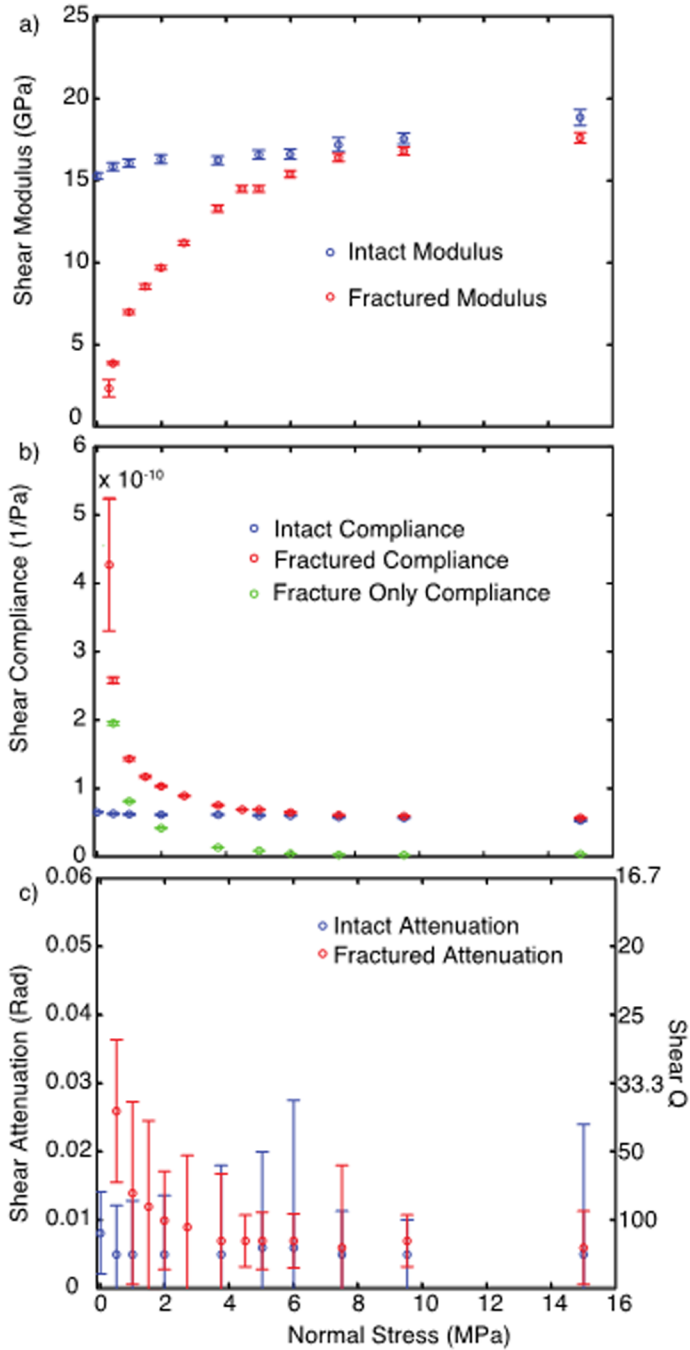
Figure 12. Duperow dolomite sample before and after fracture. **a)** Shear moduli. **b)** Measured shear compliance with calculated compliance of the fracture itself. **c)** Shear attenuation.

Figure 13 shows the pressure film measurements for the Duperow dolomite fracture. The relationship between the real contact area and uniaxial stresses are shown in Figure 13a while the insets (Figure 13b-f) show snapshots of the local normal stress distribution at the indicated normal stresses. The relatively flat surface contributes many evenly spaced asperities across the sample cross-section, which converge into larger asperities at higher normal stresses. Based on our shear measurements, we find that the

fracture was almost entirely closed until about a 6 MPa normal load was applied, but opened gradually, lowering shear modulus and Q, with decreasing normal stress (Figure 12a and c). This behavior suggests that the fracture was well-mated, similar to the Westerly granite fractured sample discussed previously, even though it had less interlocking topography.
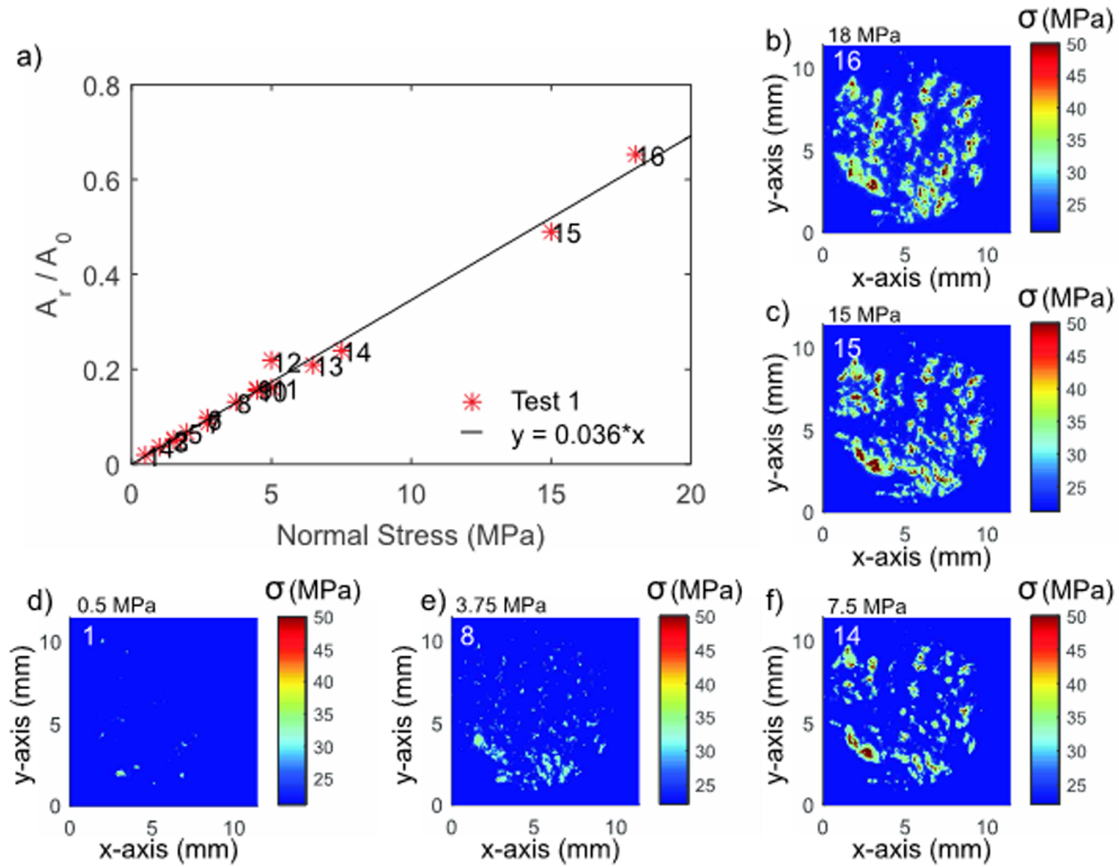
Figure 13. Pressure sensitive film measurement of Duperow dolomite. **a)** Fractional real contact area with applied normal stress, fit with a linear relationship. Local normal stress distribution from the calibrated pressure sensitive film are shown for normal stresses of **b)** 18 MPa, **c)** 15 MPa, **d)** 0.5 MPa, **e)** 3.75 MPa, **f)** 7.5 MPa.

3.2 Numerical model

Most of the fracture results (except from the Sierra White granite) follow a consistent pattern, suggesting the relationship between real contact area and shear modulus could be described with a simple model. We attempted to model this relationship with the simplest configuration possible: a sample with real contact area on the fracture represented by an infinitely thin circular bonded area in the center of the cross sectional area.

The finite element modeling was performed using the commercial software package ABAQUS/implicit (ABAQUS 2004). We attempted to develop a model that captures the stress transfer across the fracture for a range of real contact areas. The model is a cylindrical torsion bar with radius r_0 and a discontinuity along the cross-section

located at $z = L/2$. The discontinuity is used to simulate the fracture. The body is given a shear modulus, G, and Poisson ratio, ν, and behaves elastically, modeled as a classical Hookean isotropic elastic medium [*Timoshenko and Goodier*, 1951, *Davis and Selvadurai*, 1996]. The incremental strains are given by:

$$d\varepsilon_{ij} = \frac{d\sigma_{ij}}{2G} = \frac{\lambda^* \cdot d\sigma_{kk} \delta_{ij}}{2G(3\lambda + 2G)},$$

(4)

where λ^* is the Lamé's first parameter and summation is implied over repeated indices.

A cylindrical sample of length L and radius r_0 was elastically modeled using finite elements in ABAQUS, as described by equation 4. The discontinuity in the body at $z = L/2$ is denoted as a positive (+) and negative (-) surface, which was necessary for defining the boundary conditions at this location. The entire model was composed of 76,200 8-node linear brick elements (C3D8R) and was refined more finely at the bonded/frictional interface (Figure 14b). Boundary conditions are as follows:

$$u_r(r = 0, \theta, z) = 0,$$

(5)

$$u_z^{(+)}(0 < r \leq r_0, \theta, z = L/2) = u_z^{(-)} = 0, \quad \text{(no dilatation)}$$

(6)

$$\tau_{rz}^{(+)}(r^* < r \leq r_0, \theta, z = L/2) = \tau_{rz}^{(-)} = 0, \quad \text{(frictionless)}$$

(7)

$$\tau_{rz}^{(+)}(0 < r \leq r^*, \theta, z = L/2) = \tau_{rz}^{(-)}(0 < r \leq r^*, \theta, z = L/2), \quad \text{(bonded)}$$

(8)

$$u_r^{(+)}(0 < r \leq r^*, \theta, z = L/2) = u_r^{(-)}(0 < r \leq r^*, \theta, z = L/2), \quad \text{(bonded)}$$

(9)

$$u_r(0 < r \leq r_0, \theta, z = 0) = \gamma r, \quad \text{(twist)}$$

(10)

$$u_r(0 < r \leq r_0, \theta, z = L) = -\gamma r, \quad \text{(twist)}$$

(11)

where γ is the angular twist (0.004 radians).

Figure 14a shows the general configuration of the model, and the numerical mesh is shown in Figure 14b. Using the numerical model we calculated the torque T at the ends ($z = 0$ and L) generated from the application of the boundary conditions described by equations 5-11 above. The error in the numerically calculated torque T, which can be used to estimate the maximum theoretically shear stress τ_{max} (at $r = r_0$) using equation 1, was only -0.05 to 0.2% of the maximum shear stress calculated numerically.
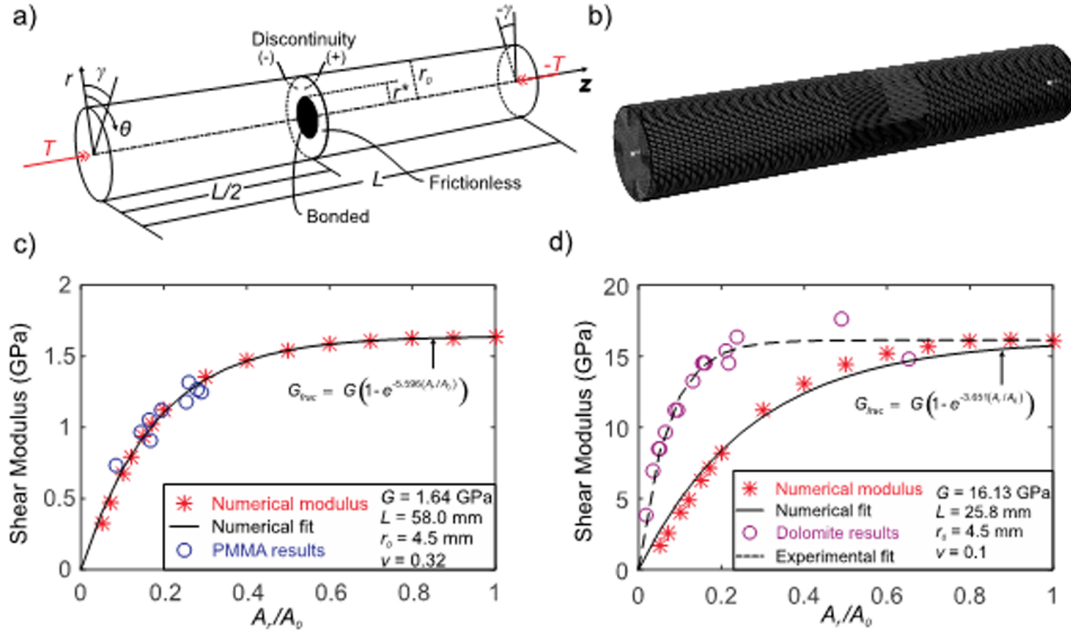
Figure 14. ABAQUS/implicit (ABAQUS, 2004) numerical model used to measure fractured shear modulus of a torsional beam with a circular cross-section. **a)** Shows the schematic representation of the geometry and boundary conditions (equations 5-11) used to perform numerical calculations. **b)** The mesh discretization of the finite element model. **c)** The fractured shear modulus for sample with dimensions and properties of the PMMA sample. The numerical results (red stars) roughly follow an exponential relationship (equation 4). The model was fit to the measurements of the fractured PMMA (blue circles). **d)** Numerical results for the model with dimensions and material properties of Duperow dolomite (red stars) and measurements of dolomite (magenta circles). The equations for the exponential fits to the experimental data are in Figure 15.

In Figure 14c the red stars represent the numerical results using material properties measured for the PMMA (Table 1): $L = 58$mm, Poisson's ratio $v = 0.32$ and intact shear modulus of $G = 1.64$ GPa, both of which were measured independently. The numerically calculated torque T was determined for various ratios of A_r/A_0 and converted to a fractured shear modulus using equation 3. We see that as the ratio of real to nominal contact approaches 1 (i.e. $r^* \rightarrow r_0$) the model converges to the intact shear modulus G and, conversely, as $r^* \rightarrow 0$ the shear modulus tends towards zero. For this reason, we attempt to characterize the numerical model using an exponential relation of the form:

$$G_{frac} = G\left(1 - e^{-\lambda(A_r/A_0)}\right), \tag{12}$$

where G_{frac} is the fractured shear modulus (see Figures 6, 8, 10 and 12) and λ is a variable that describes the manner in which stresses are transferred across the discontinuity (interface) and is likely determined by the sample geometry and the Poisson's ratio in the model. In the experiments, fractures with more heterogeneous, out-of-plane, or interacting asperities reach higher moduli at lower real contact areas, which is captured by a higher λ fitting parameter in this formulation.

In Figure 14c, we show that the numerical model (red stars) for the PMMA parameters could be fitted using equation 2 (black line) using a value of $\lambda = 5.596$ ($R^2 = 0.99$) and assuming $G = 1.64$ GPa. Comparing these results to the experimental data from the PMMA tests (blue circles), we see that the model provides a reasonable understanding of the evolution of the fractured PMMA shear modulus for a range of real contact area. The effectiveness of the model may be due to the rounded high in the center of the sample's surface topography (Figure 3) causing the circular real contact area to increase radially outwards as the uniaxial normal stress is increased (Figure 7) – geometrically similar to the numerical model described in Figure 14a.

To determine if the model could successfully replicate rock-rock interfaces, we attempted to model the dolomite experiment in a similar manner. A new numerical model was formulated to match the active length of the dolomite samples $L = 25.8$ mm. A Poisson's ratio of $v = 0.1$ (measured at ultrasonic frequencies) and the intact shear modulus of $G = 16.13$ GPa (measured under the highest normal stresses) were prescribed. The relationship calculated for the dolomite parameters is different than that for PMMA (red stars in Figure 14d vs 14c): the dolomite model requires higher levels of real contact to recover the intact shear modulus (at $r^*=r_0$), characterized by a lower value of $\lambda = 3.651$ ($R^2 = 0.9804$). The calculated relationship also differs from the experimental results from the Duperow dolomite (magenta circles) characterized by $G = 16.13$ GPa and $\lambda = 14.13$ ($R^2 = 0.9688$). The comparison of numerical to experimental results shown in Figure 14d indicates that the dolomite shear modulus approached its intact modulus at lower real contact areas than the numerical model predicted.

In Figure 15 we plot the relationship between fractured shear modulus and fractional real contact area for PMMA, as well as the well-mated Westerly granite and Duperow dolomite. The exponential behavior of the both the Westerly granite and Duperow dolomite were quite similar and both would not be well characterized by the model that was able to predict the behavior of the PMMA surface. The Westerly granite and Duperow dolomite increase modulus more with increasing contact area than the model predicts; this is likely due to the effects of the heterogeneous rock surface, finite width damage zone, asperity interaction, and non-normal, 'shear interlocking', fracture surfaces [*Selvadurai and Yu,* 2005]. Surface topography has been shown to affect the constitutive behavior of fractures, including a variety of behavior due to the ratio of normal to shear fracture stiffness and local asperity interactions [*Boitnott* 1992, *Selvadurai and Yu,* 2005, *Campañá et al.,* 2011, *Mirsa and Huang,* 2012]. Local stress transferred through these asperity interactions could cause the fracture surface to behave as if it has a higher contact area. These effects could be accounted for with a model that includes the complex fracture surface geometry [e.g., *Morris* 2015], which could be input from the measured topography (Figure 3) or images of stress distribution at increasing normal load (Figures 9, 11, and 13).
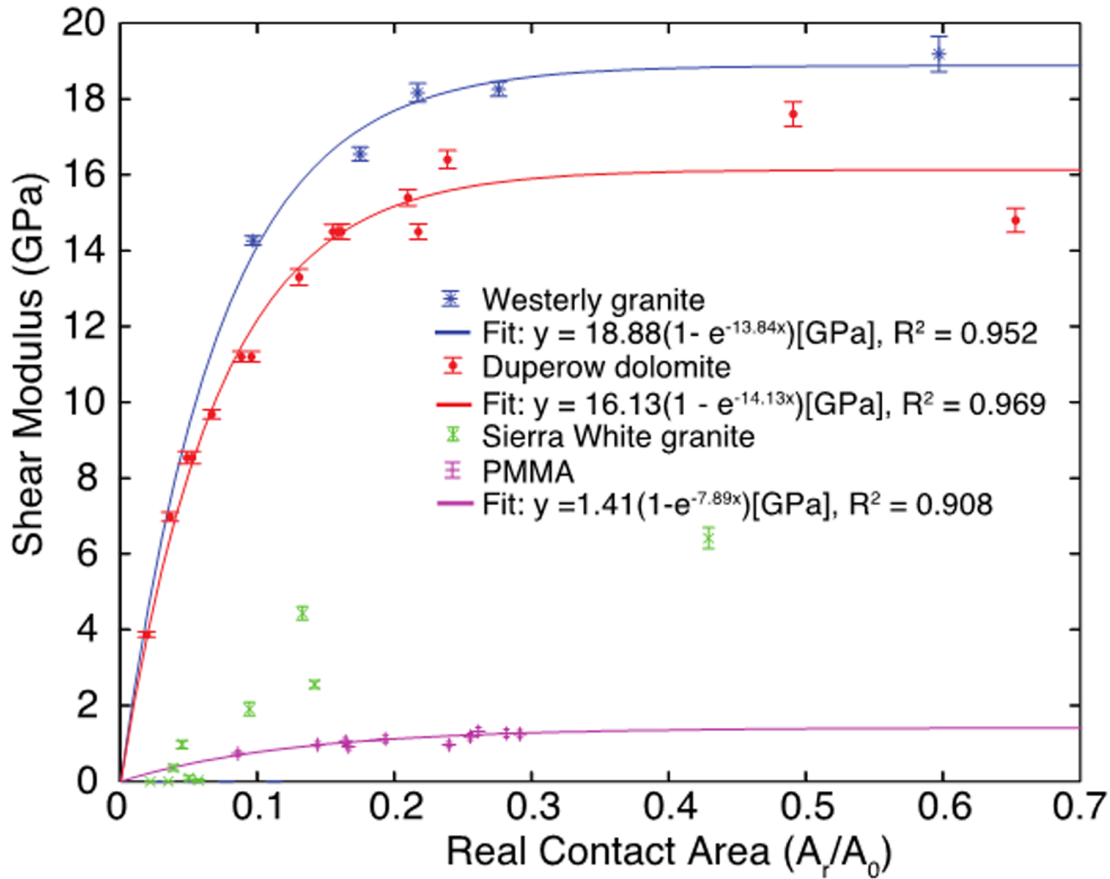
Figure 15. The fractional real contact area measured by the pressure sensitive film for various normal stresses and the shear modulus of the fractured sample measured at those normal stresses, fit with exponential functions. The Sierra White relationship does not fit an exponential because it appears to have different regimes of behavior at different contact areas.

The model assumes that the fracturing process represents the creation of a single, infinitely thin, through-going fracture between the two sides of intact rock. This ignores the effect of the process zone of precursor microcracks, some of which coalesced into the fracture, while others were left isolated on either side of the fracture surface [*Reches and Lockner,* 1994]. As stated in the fractured results section above, the fact that few grains were broken off from fracturing suggests that these microcracks extended on the order of a full grain diameter (~0.2 mm for Westerly granite) into the rock surfaces. *Moore and Lockner* [1995] observed extensive microcracking ~10 mm away from a controlled, not through-going, shear fracture in Westerly granite, under much higher stress conditions - 50 MPa of confining pressure. Direct observation or modeling of this damage zone is beyond the scope of this work, but we believe that the microcracking was much less extensive in our case, because the tensile fracture was under much less stress, limited only by the tensile strength of the rock, and because it propagated much faster through our entire sample. Still, the existence of these microcracks in the rock fracture zones (as opposed to PMMA) could also help explain why the rock fractures cannot fit the modeled contact area vs modulus relationships (Figure 14d). The fractured rock modulus will

increase more with normal stress as these other cracks close up, adding to the effect from increasing contact area that we model. For reference, the modulus change due to stress induced microcrack closure is shown in the stress dependence of the intact rock sample (blue lines on Figures 8a, 10a, and 12a). This represents a lower bound on the magnitude of the effect, as the microcrack density has been found to increase by a factor of 3 or more in the damage zone [*Moore and Lockner,* 1995].

The topography of the Westerly granite surfaces, and Duperow dolomite to a lesser degree, were significantly rougher than the PMMA surfaces as seen quantitatively by the height variations shown in Figure 3. We believe that was due to the grain scale heterogeneity of the rock and the different fracturing approaches. The induced fractures appeared very well-mated and reached completely clamped conditions (i.e. same shear modulus as intact sample), at normal stresses greater than or equal to about 7.5 MPa for the Westerly granite and 6 MPa for Duperow dolomite. In contrast, an existing fracture in Sierra White granite was not as well-mated or interlocking as the induced fractures. The Sierra White was the only fractured sample that was limited to a shear modulus of about 50% of the intact shear modulus at the highest normal stresses (Figure 10a). It was also the only sample that seemed to preferentially add contact area close to the center of the sample cross-section (Figure 11), where the shear strains are lowest and thus affects the fracture shear modulus the least. Our model could be adapted to match the radius at which contact area is added, as measured with the pressure sensitive film, which should affect the rate at which the fractured shear modulus starts to asymptote towards the intact value. The Sierra White behavior also does not fit an exponential relationship because it appears to show different stiffening regimes at different normal loads. Less well-mated rock fractures likely need a more advanced model to account for frictional partial slip [*Cattaneo* 1938, *Ciaveralla* 1998, *Selvadurai and Glaser,* 2015a]; they do not satisfy the assumption of completely bonded contact in the low normal stress regime.

3.3 Detectability calculation

Following *Pyrak-Nolte et al.* [1990], we calculated the reflection and transmission coefficients for a S-wave normal incident on our dry fractures over a range of normal stresses at seismic frequencies. They derived expressions for these coefficients using a Linear-Slip Interface Model [*Schoenberg* 1980] with a single, infinitely thin, fracture represented as a displacement discontinuity between two elastic half-spaces (of seismic impedance Z). The model does not include the effect of other parallel microcracks, which would add to the reflectivity of the damage zone. It also assumes that stress is continuous across the fracture but that displacement is discontinuous. This is a reasonable assumption for our experiment for all but the most open fractures (lowest normal stress conditions on less mated Sierra White), where we observe partial slip and stress transmission is incomplete and unpredictable across the fracture. At this point the fractures are very compliant and should reflect enough energy to be detectable. Analysis of the highest normal stress measurements was also problematic; the calculation of fracture specific shear stiffness is inaccurate when the fractured modulus is close to the same as the intact modulus, because the fracture approaches infinite stiffness. These fractures have very small apertures, and reflect little seismic energy, thus are not the focus of this study.

Pyrak-Nolte et al. [1990] derive a general solution for all angles of incidence, but focus on normal incidence as it represents the highest reflection:

$$R_{S\theta}(\omega) = -i\omega/[-i\omega + 2(\kappa_\theta/Z_S)] \tag{13}$$

$$T_{S\theta}(\omega) = 2(\kappa_\theta/Z_S)/[-i\omega + 2(\kappa_\theta/Z_S)] \tag{14}$$

where $R_{S\theta}$ and $T_{S\theta}$ are the reflection and transmission coefficients for S-waves, respectively, ω is the frequency of the probing wave, κ_θ is the fracture specific shear stiffness measured in rotation, and Z_S is the seismic impedance measured at frequency ω also in rotation. The imaginary part of the equation is used to calculate phase delays but can be ignored in our case. *Pyrak-Nolte et al.* [1990] derived these expressions to account for anisotropy between SH and SV waves, but our measurement is in torsion, which combines motion in the x- and y-directions. $R_{S\theta}$ should be equivalent to R_{SH} and R_{SV} for an isotropic medium and planar fracture.

We calculated fracture specific stiffness values, κ_θ, from our measurements by subtracting out the compliance of the intact sample, the same calculation described above. This allowed us to effectively estimate the displacement on the fracture itself for a given applied shear stress. We believe this is equivalent to a measurement of stress-displacement curves commonly used to calculate fracture specific stiffness [*Pyrak-Nolte et al.,* 1990]. To convert our specific stiffness values to commonly used units (Pa/m), we divided by the circumference of the sample, which converts our shear strain back to displacement on the outside of the sample radius; strain is based on an angular displacement (see equation 2) only across the fracture. We used shear modulus measurements of the intact rock to calculate the impedance of the elastic half-space in the seismic frequency range.

Pyrak-Nolte et al. [1990] also derived an extension of the model to capture fluid filled fractures with viscous coupling and dissipation, where there is a discontinuity in velocity as well as displacement across the fracture. Although we do not directly address this scenario here, these expressions can be used to see the effect of different fluids using our fracture measurements, by assuming that the fluid itself has no effect on the fracture stiffness in shear.

Although we are interested in the seismic signature of many fractures in a reservoir as effective stress changes with injection, we analyze the effect of a single fracture from our measurements. Further analysis is necessary to understand the effect of a natural or engineered fracture network and other details of wave propagation in this setting. Figure 16a shows the calculation of reflectivity as a function of normal stress for each of the fractured rock samples, with the Sierra White fracture shown at each frequency measured. The Sierra White fracture becomes more reflective at higher normal stresses and reaches a larger value of reflectivity than the other materials, likely because it is less well-mated and thus the joint more compliant.
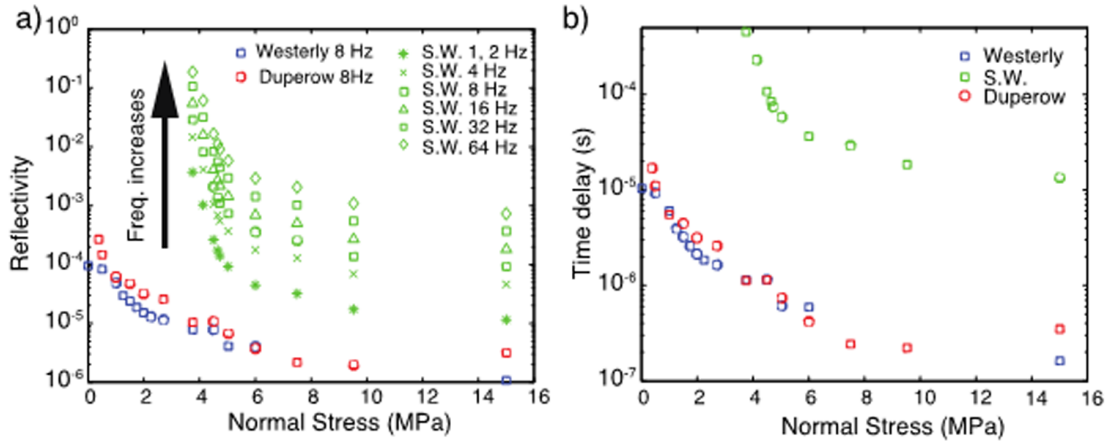
Figure 16. a) Calculated reflection coefficients for coarse grained Sierra White granite (S.W.), fine grained Westerly granite and fine grained Duperow dolomite fractures under a range of normal stresses and frequencies, using equation 13 from *Pyrak-Nolte et al.* [1990]. Westerly granite and Duperow dolomite fracture have low reflectivity because they are well-mated. **b)** Time delay calculated for a shear wave across the fractured sample relative to the intact sample. Repeatable cross-well sources can detect time delays as low as 6 nanoseconds when stacked sufficiently [*Silver et al.,* 2007], this calculation suggests all of these delays could be seismically detectable.

Another way to determine the effect of fractures on seismic measurements is the direct time delay of S-wave arrivals due to the lower velocity of the fracture and damage zone. The time delay was calculated using measured modulus and active length to give a travel time across the entire fractured sample, including any damaged zone, minus that in the intact sample. Figure 16b presents the time delay calculation for each rock sample (there is very little frequency dependence) as a function of normal stress. Detectability of time delays as low as 6 nanoseconds has been achieved with well-calibrated semi-permanent deployments of repeatable sources at higher frequencies in a cross-well configuration [*Silver et al.,* 2007] or at low frequencies from surface sources [*Dou et al.,* 2016]. Even the well-mated single fractures at our highest normal stresses have calculated time delays more than two orders of magnitude above this instrumental limit. In practice, most deployments are not capable of such sensitivity but microsecond repeatability is straightforward to measure with piezoelectric or magnetostrictive sources. These calculations are only meant as an illustration for how these measurements could be used to guide field predictions and interpretation, more detailed wave propagation models through fracture networks and further measurements of natural fractures are necessary to more accurately predict the seismic signature in a fractured reservoir.

3.4 Conclusions

We present a technical description of a low-frequency (0.01 - 100 Hz) shear modulus and attenuation instrument adapted to measure fractured rock samples in a torsional configuration. We provide details of the calibration and error estimation methods using a sample of PMMA that conforms to shear measurements made in the literature. Our apparatus is well-suited for the measurement of fractured samples under a range of normal stresses, from fully clamped (intact) to nearly open fractures. We

observe very different behavior for two granite samples that have different surface topography and degrees of mating as measured with an optical profilometer. We highlight the importance of the out-of-plane topographic geometry in the shear behavior of a fracture by comparing the experimental results to a simple numerical model. We combine our measurement of elastic changes due to normal load with a novel surface characterization technique that employs a pressure sensitive film to image the normal stress distribution on the fracture interface. This provides a better understanding of the effect of microstructure and heterogeneity on seismic properties.

A simple numerical model is able to explain the exponential relationship between real contact area and fractured shear modulus. We were able to match the data from PMMA interfaces with the model because of their relatively simple surface topography, while the rock specimens exhibited more complex behaviors. The well-mated fractures in Westerly granite and Duperow dolomite specimens followed an exponential relationship but stiffen more at lower contact area then the model suggested. We propose that the out-of-plane asperity geometry and interaction for the more heterogeneous surfaces become important when understanding the shear and seismic behavior of fractures at small length scales.

We then apply our fracture measurements to theory developed to calculated reflection and transmission coefficients for normally incident seismic waves in a field setting. These calculations, as well as estimations of shear wave time delays due to the fractures, are useful for determining under what stress and fracture mating conditions a fracture is seismically visible. These results are limited, representing only the specific, single fractures we measured, which are likely better mated than corresponding fracture networks in the field. Further measurements of natural fractures from the reservoir and more detailed wave propagation models through realistic fracture networks can help guide seismic monitoring, such as needed during injection of supercritical CO_2 for geologic carbon storage.

The images of stress distribution on fracture faces in combination with sensitive measurements of large modulus changes at low normal loads provide a detailed look into underlying mechanics of seismic waves incident on fractures. Further experiments are needed to probe the range of phenomena present in fracture systems, especially at low normal loads. These laboratory measurements could be used to extract more information from open fractures in the field, but understanding the results will require further model development, both capturing the geometry of asperity contacts and frictional partial slip on contacts at lower normal stresses.

4. NONLINEAR STRAIN-SOFTENING AND ATTENUATION

4.1 Low normal stress nonlinear measurements

While intact and fractured under higher normal stresses, the samples show linear stress-strain curves, with comparatively little nonlinearity. We now focus on the nonlinear effects at the lowest measurable normal stresses, before full slip occurs. We were unable to measure the rhyolite sample at lower normal stresses because, as described previously, a piece was lost from the interface during the fracturing process, limiting the amount of contact area available, especially at low normal stresses. The 1000 measurements for each sample were taken by progressively increasing the oscillation amplitude over the course of about 3 hours (Figure 17). The samples show little hysteresis when remeasured at the lowest amplitudes (not shown). Stress-strain curves, and strain-dependent moduli and attenuation changes were measured in all three of the rock types with differing slopes (Figure 17). The single effective asperity partial slip model, described below, is fit for each stress-strain curve and plotted on the measurements in black (Figure 17a). Equations for linear fits are given on the modulus versus strain plots (Figure 17b).

The different rocks' strain-dependent softening slopes vary by about a factor of five (Table 2). The nonlinear parameter (α) is calculated from the change in modulus with increasing strain, following the equation:

$$\frac{\Delta G}{G} = \alpha\, \varepsilon, \tag{15}$$

where ΔG is the change in modulus, normalized by the low strain amplitude modulus, G, and ε is the strain, in units of μstrain. The nonlinear parameter has been measured for a range of micro-cracked rocks to have comparable values. For example, $\alpha \sim 0.012$ μstrain^{-1} was measured in extension for intact Berkeley Blue granite [*Rivière et al.,* 2015] and $\alpha \sim 0.0028$ μstrain^{-1} was measured for Berea sandstone in torsion [*Remillieux et al.,* 2016]. In contrast, granular media, such as fault gouge, have been measured to have stress-strain curves that roll over completely, giving a negligible shear modulus at high strains [e.g., *van der Elst and Savage,* 2015]. We expect that throughgoing fractures will exhibit strain-dependent behavior approaching unconsolidated granular media when under lower normal stresses or higher shear amplitudes.

We also solve for the proportionality between attenuation and strain amplitude (Table 1), which can be compared to consolidated data for various intact, micro-cracked, rocks given in *Mavko* [1979]. As expected, the fractured rocks we measure have about an order of magnitude greater attenuation (Q order 100 for Montello granite fracture versus order 1000 for intact Chester granite) and amplitude dependence (~400 radians/strain for the Montello granite fracture versus ~40 radians/strain for intact Chester granite) than comparable intact rocks [*Gordon and Rader,* 1971]. This is not a perfect comparison, because the intact Chester granite measurements were made in

longitudinal compression, but the order of magnitude difference is robust [*Gordon and Rader*, 1971]. We also found that the attenuation saturates at high strains for the Duperow dolomite fracture, as seen Figure 2c. This behavior has been observed in high strain measurements of frictional attenuation in intact rocks, such as Fredrick diabase [*Cooper* 1979].
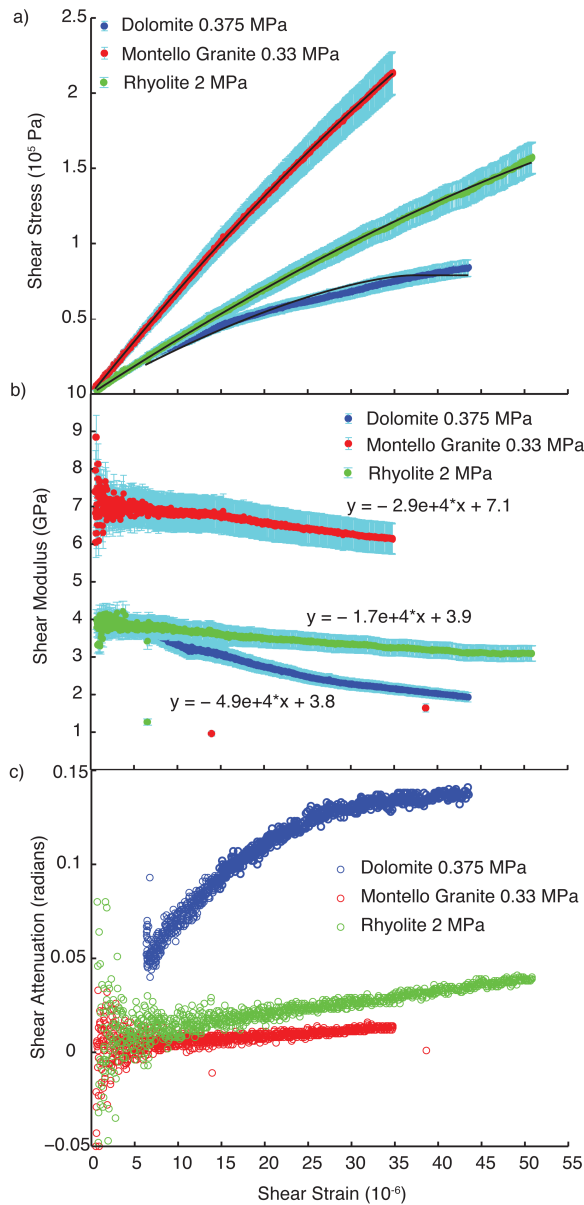
Figure 17. Strain dependent **a)** shear stress, **b)** shear modulus, and **c)** shear attenuation for all three tensile rock fractures at their lowest measurable normal stress conditions. Duperow dolomite at 0.375 MPa is shown in blue, Montello granite at 0.33 MPa in red, and Blue Canyon Dome rhyolite at 2 MPa in green, error bars are estimated from the systematic error (as described in text) and plotted in cyan. **a)** The best-fit single effective asperity partial slip model is plotted with black line on each measured stress-strain curve and **b)** the equation for linear fit of modulus versus strain is given, where the slope is a

measure of the nonlinearity, and the y intercept is the modulus at infinitesimal-strain. The nonlinear parameter α is this slope normalized by the modulus.

4.2 Partial Slip Model

These measurements provide evidence of partial slip on the fracture interface. The departure from linear stress-strain relationship, where the modulus is a constant, is caused by the initiation of slip on the outside of the asperity contacts; this is referred to as partial slip because the centers of the asperities remain stuck. As the strain amplitude increases, the stuck section of the contacts shrink and the slipping regions grow, causing a smaller resistance to shear or lower measured shear modulus. This softening continues until the asperities are completely slipping and the stress-strain curve is flat because slip continues without increasing the stress. We associate the displacement where the full slip condition is reached with the critical slip distance (d_c), a rate-and-state friction parameter [*Ruina* 1983].

The measured shear stress-strain curve (Figures 17a and 18) resemble other experiments and models of micron-scale initial displacements due to direct shear on frictional interfaces [e.g., *Boitnott et al.,* 1992]. The data and model fit values, described below, are comparable to those found for Westerly granite fracture faces under higher normal stresses of ~10 MPa [*Boitnott et al.,* 1992]. This suggests our displacements are in the range dominated by partial slip, before many asperities are fully slipping, and is consistent with measurements of flat stress-strain curves when asperities fully slip.

In order to model the measured nonlinear stress-strain constitutive relationship, we implement an effective single asperity partial slip model. *Mindlin* [1949] solved the mixed boundary value problem for two spheres in contact assuming a simple friction strength law:

$$t_s = \mu_f t_N, \tag{16}$$

where t_S is the maximum magnitude of the shear traction on a patch of real contact area, t_N is the magnitude of the normal traction at the same location, and μ_f is the constant friction coefficient. The resulting single asperity force - displacement relationship can be expressed as:

$$t_s = \mu_f t_N [1 - \left(1 - \frac{16 G a \delta}{3(2-\nu)\mu_f t_N}\right)^{3/2}], \tag{17}$$

where G is the intact rock shear modulus, a is the radius of the asperity contact, δ is the shear displacement, assumed uniform everywhere, and ν is the intact rock Poisson's ratio. The shear force and displacement is then converted to stress and strain given the measured sample geometry. We use this equation to calculate the shear stress for our measured range of shear strains, giving a stress-strain relationship that can be compared to the observations.

We make several assumptions in using this simplified model. First we use a single effective circular contact to represent the complex asperity geometry (Figures 5a and 5b), making the inverted parameters effective values, which represent the heterogeneous properties of the entire surface. Also the model is designed for linear slip geometry, while

we are slipping in torsion, but each of the asperities individually are deforming linearly in the tangential direction, given our small angular displacements.

By integrating this single asperity shear force - displacement relationship over a statistical population of asperities on a planar fracture [*Boitnott et al.,* 1992] or a spherical grain pack with a given porosity and coordination number [*Duffaut et al.,* 2010] nonlinear, friction coefficient dependent, constitutive relations for partial slip have been derived and compared to laboratory data. More complex modeling, using surface characterization methods to constrain the asperity and surface geometry, could also be implemented to better understand the frictional properties of the interface but are outside the scope of this letter. The current pressure sensitive film cannot resolve the low normal stresses on asperities at the lowest measurable applied uniaxial loads, but more sensitive film measurements could also be combined with numerical models to understand the effect of asperity interaction and geometry.
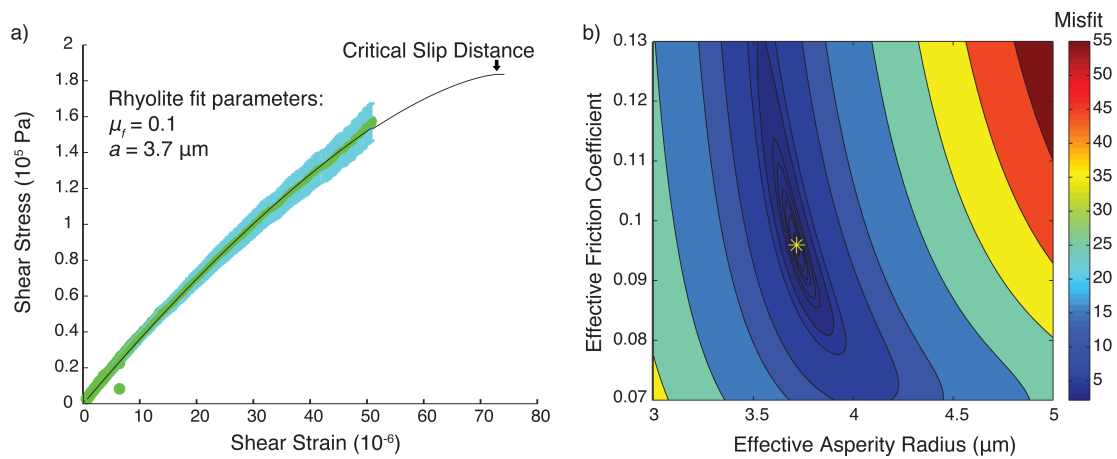

Figure 18. a) Measured shear stress - strain curve, with error bars in cyan, for the Blue Canyon Dome rhyolite fracture, and the single asperity partial slip model fit, converted from shear force (t_S) and displacement (δ) in equation (3). Measured values were used for the normal force ($t_N = 127$ N), intact shear modulus ($G = 15.4$ GPa), and Poisson's ratio ($v = 0.08$) while the friction coefficient ($\mu_f = 0.1$) and asperity radius ($a = 3.7$ μm) are optimum fit values. **b)** The sensitivity of the fit, with misfit plotted in color as function of effective friction coefficient and effective asperity radius, showing the tradeoffs between the two fit parameters. The range of asperity radius is relatively small (~3.5 – 4.5 μm) while the friction coefficient is less sensitive and has a minimum value (~0.07); the optimal fit is shown as a star.

The simple single asperity model can be fit to the observed nonlinear strain softening behavior for all three of the fractures (Figure 17a), using measured rock elastic properties, normal stress conditions, and fitting two free parameters – asperity radius (a) and friction coefficient (μ_f) – which effectively represent the entire surface. Figure 18 shows the fit in detail for the Blue Canyon Dome rhyolite fracture, and the model misfit surface for combinations of the fit parameters, calculated using equation 17. As can be seen, while the fit seems to have a higher sensitivity to asperity radius, both parameters are effectively constrained. As stated previously, the fitted asperity contact area cannot be compared directly to the measured contact area from pressure sensitive film measurement (Figure 5d), but the calculations are consistent with the upper bound on real contact area

provided by the film under slightly higher normal stresses. It is expected that, even for very smooth surfaces, the real contact area is much less than the total cross sectional area [*Scholtz* 2002]. These fits are effective values, thus also include the affect of asperity interaction, which has been shown to increase the effective contact area, relative to the measured real contact area, and stiffen rock fracture surfaces [*Saltiel et al.,* 2017a].

The parameter fits for all three fractured samples, as well as the modulus and attenuation slopes with strain are given in Table 1. The fit for the dolomite sample is not as robust as those for the other samples due to the larger variations in slope with time during the experiment. The model fits presented are used to show that the proposed process explains the measurements' general features, not to interpret the parameter values in detail. A more complex asperity model is likely necessary to fully fit the data and understand the friction coefficient for each rock type.

Rock Type, Bulk Normal Stress (MPa)	Strain-softening, Nonlinearity, slope α (μstrain^{-1})	Attenuation – Strain Proportionality (radians/strain)	Fit Effective Friction Coefficient	Fit Effective Asperity Radius (μm)
Duperow Dolomite, 0.375 MPa	0.018	4,200	0.2	3
Blue Canyon Dome Rhyolite, 2 MPa	0.0044	600	0.1	4
Montello Granite, 0.33 MPa	0.0041	400	0.9	3

Table 2. Fit strain-softening slopes, attenuation-strain proportionality, and single asperity partial slip model parameters for each of the three measured fractured rock types under lowest measurable normal stress.

By fitting our data for the initiation of partial slip (the first ~1.8 microns of displacement) for the Blue Canyon Dome rhyolite, we extrapolate the curve to calculate the shear displacement (d_c = 2.57 µm), or strain (7.34 x 10^{-5}) and force (t_{Scr} = 11.68 N), or stress (183.6 kPa), where the effective asperity is fully slipping, a proxy for the critical slip distance. The calculation of critical slip distance is more robust than the fitting parameters, because it only relies on extrapolating the shape of the curve, not on any quantitative input values. The force-displacement curve for the rhyolite sample appears to stiffen slightly at the very highest strains; this may be due to ploughing in those asperities that are fully slipping, as was suggested by *Boitnott et al.,* [1992].

These comparisons and model fits support our hypothesis that we are measuring frictional attenuation and partial slip. The data also show that these signals are enhanced

in rocks with larger, throughgoing fractures. Although frictional attenuation mechanisms and nonlinear effects are not seen as dominant signals for seismic-amplitude strains on micro-cracked, intact rocks, these findings suggest that they could be important and useful on macro-scale reservoir fractures or faults with high amplitude waves, such as near repeatable cross-well sources. Although humidity insures adsorbed water on fracture surfaces, bulk fluids in the subsurface would likely modify the friction, potentially through lubrication or by increasing the area under frictional contact [*Cooper* 1979]. Future experiments will address the effect of fluids on these measurements.

Measurements of this kind in a wide range of rock types, fluid conditions, and fracture geometries could help in understanding the evolving frictional properties and how they respond to reservoir and fault processes. For example, monitoring reservoir injection for these signals could elucidate the effect of elevated pore pressures in opening fractures and changing their frictional response. One possibility is constraining the lubrication effect of injectants (e.g. $scCO_2$) and their chemical interaction with fracture surfaces *in situ*. This new frictional information could be especially useful in explaining injection-induced seismicity and provide needed feedback to operators. The potential to measure the approach towards critical stress states directly would be an important tool in reservoir stress management and limiting induced seismicity hazards.

5. NONLINEAR HYSTERESIS AND FREQUENCY-DEPENDENCE

5.1 Fundamental frequency dispersion

At the lowest normal stress (0.375 MPa), we also used a range of driving frequencies from 1 to 64 Hz. The intact dolomite shows normal dispersion, i.e. increasing modulus with frequency (Figure 19a). The fractured sample showed modulus decreasing with increasing frequency in the low frequency range (1 - 4 Hz), and normal dispersion, as seen at higher normal stresses, resumes at higher frequencies (8 - 64 Hz) (Figure 19b). This inverse dispersion behavior is not expected for linear anelastic materials, where dispersion is directly related to dissipation [*Zener* 1948], suggesting the fracture is exhibiting nonlinear hysteresis. It also suggests there may be a nonlinear process occurring at low frequencies (< ~8 Hz) in open fractures which is not present at higher frequencies (> ~8 Hz) or in closed fractures, or intact, micro-cracked rocks.
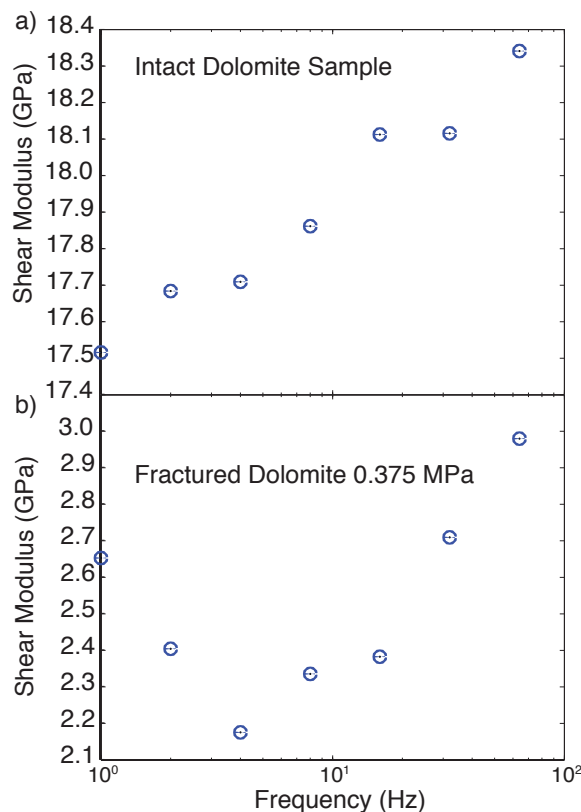

Figure 19. Shear modulus dispersion results for dolomite both **a)** intact and **b)** fractured under 0.375 MPa normal stress with fundamental frequency data. Driving frequency varies from 1 – 64 Hz. **a)** The intact sample shows normal dispersion, increasing modulus (or velocity) with frequency, while **b)** the fractured sample shows inverse dispersion at

frequencies below about 8 Hz and normal dispersion above about 8 Hz. This is similar to the frequency dependence of the hysteresis loops explained below, suggesting a low frequency stiffening mechanism that seems to disappear above 8 Hz.

5.2 Time-series data: nonlinear hysteresis loops

In addition to using the Fourier transform to isolate the response at the driving frequency, we analyze the time-series data of the stress and strain oscillations (Figure 20). Graphing the stress and strain against each other over time provides the stress-strain hysteresis loop, plotted in the inset of Figure 20. If the stress and strain were perfectly periodic, with the strain phase delayed by the attenuation as expected in linear anelasticity, than the hysteresis loop would be an ellipse (periodic fits shown with black lines in Figure 20). Without phase delay the stress-strain curve would be a straight line with the slope given by the modulus, but because the strain follows the stress, the curve starts above this line and returns below the line, creating an ellipse. Throughout the oscillation, the strain-rate is also oscillating, so changes in the response due to rate dependence would cause further structure, steepening or becoming shallower (and their associated changes in modulus) with the changing strain-rate.
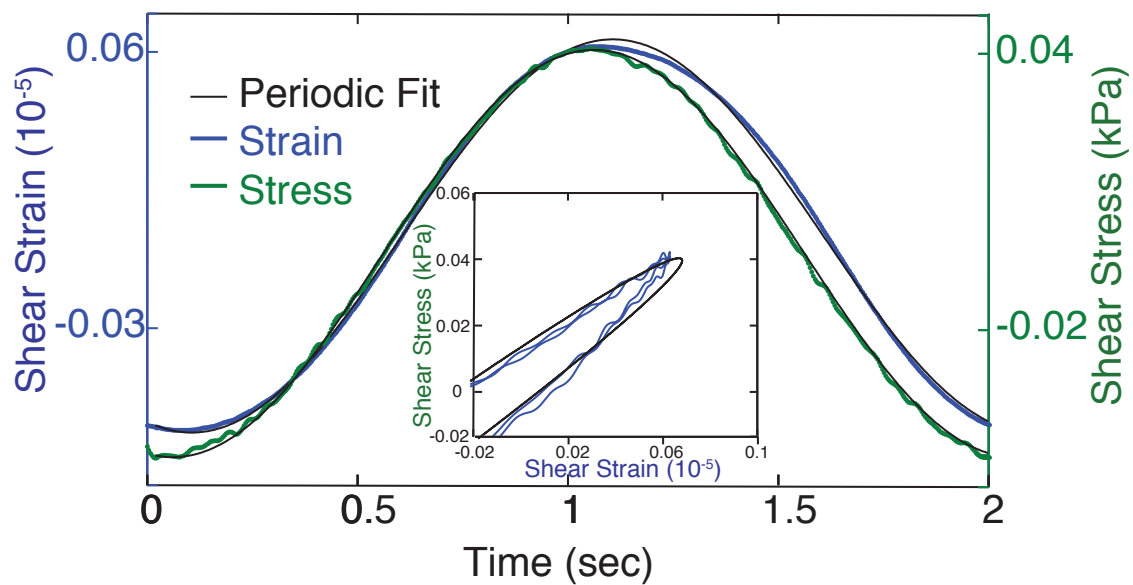
Figure 20. Stress (green) and strain (blue) time-series for the Duperow dolomite fracture under 0.375 MPa normal stress and forced with a 0.5 Hz driving frequency. The periodic fit, captured in the fundamental mode data, is plotted in black. The inset shows the stress-strain hysteresis loop, when stress and strain are plotted against each other over time. The data is to first order periodic, but shows further structure provided by the harmonics that are generated by nonlinearities and rate-dependence. The high frequency fluctuations are mainly due to 60 Hz electronic noise.

The stress-strain curve for the intact dolomite without uniaxial load exhibits much less hysteresis or nonlinearity (Figure 21a), likewise the stress and strain spectra show no clear harmonic generation (Figure 21b). Although we do expect some strain dependent softening and hysteresis due to attenuation for the micro-cracked rock, it is much smaller and not visible on the scale of our measurements. The intact rock also does not show any

strain-rate dependent effects, allowing us to assume that the observed behavior in the fractured rock is due primarily to the fracture and not the intact part.

To best visualize the nonlinear hysteresis shape, we preform a low-pass filter to remove high frequency noise, which is dominated by 60 Hz power noise. This filtered stress-strain hysteresis loop for the fractured dolomite is graphed in blue in Figure 21c. We find a nonlinear hysteresis shape in the stress-strain loops is accompanied by large harmonic generation (Figure 21d). The added structure in the shape appears most clearly as curled up (stiffening) cusps at the ends of the loop, the stress and strain sinusoid peaks. These cusps are different from those observed in intact, micro-cracked rocks at higher strain levels [*Gordon and Davis* 1968, *McKavanagh and Stacey* 1974] because they curl up as well as sharpen to a point at the end. For this reason we refer to them as 'stiffening cusps'. Hysteresis loops with stiffening at the high strain end have been observed in intact, micro-cracked rocks under quasi-static uniaxial compression [*Holcomb* 1981], but the interpretation is different, stiffening is expected due to closure of progressively stiffer cracks with compression. Since our measurements are pure shear, we do not expect a direct strain dependence to cause the observed stiffening, in fact the direct strain dependence was shown to cause softening (Figure 17a and b).

The hysteretic loop for linear elastic materials without harmonic generation, caused purely by phase delay is an ellipse (graphed in black on Figure 21c), and the area inside the loop is a measure of the energy dissipation or attenuation. The cusped shape comes from harmonic generation in the strain measurement (Figure 21d), and modifies the classical attenuation caused purely by phase delay. The frequency domain stress signal, graphed in green in Figure 21d, does not have harmonics, demonstrating that the source of the nonlinearity is in the rock fracture and not the electronics or magnetic driver. The relative effect of the harmonics that cause the nonlinear part of the hysteresis is a few percent of the total strain amplitude, a second order effect to the anelastic behavior of the sample.
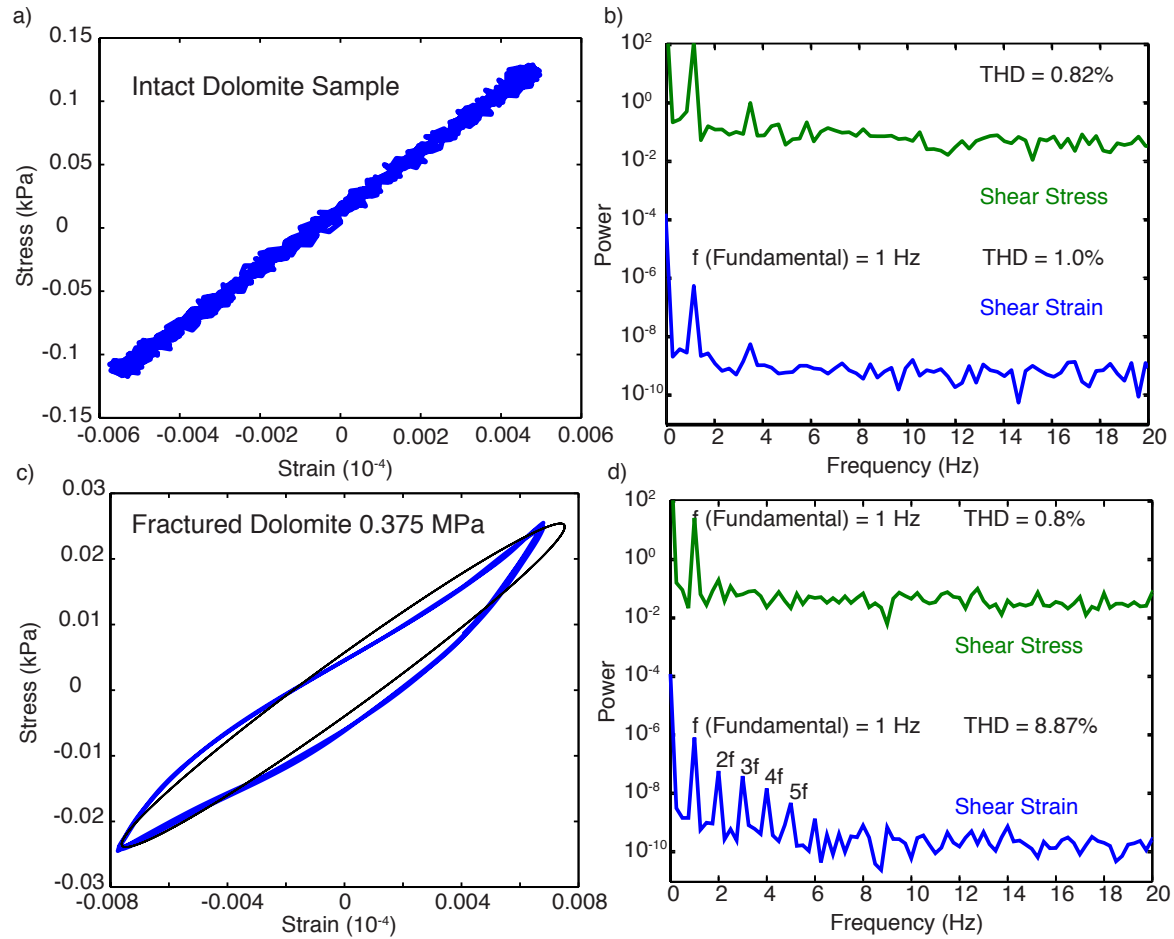
Figure 21. a) Measured stress-strain loop, in blue, of intact dolomite sample under no uniaxial stress with 1 Hz driving frequency shows no nonlinearity, cusp, or hysteresis. **b)** The frequency spectrum also shows no harmonic generation. **c)** While the stress-strain loop, in blue, when the dolomite sample is fractured under 0.375 MPa normal stress shows nonlinear hysteresis. The fundamental frequency data, only including the phase delay between stress and strain, would be the black ellipse, predicted by linear anelasticity. **d)** The fractured dolomite's frequency-spectrum shows large harmonic generation in the strain, while the stress stays linear. The odd harmonics are slightly enhanced relative to the expected power law decay. This harmonic generation is associated with the nonlinear hysteresis shape and sideband production.

5.3 Frequency-dependence and harmonic generation

Although the times-series and hysteresis loops are the most illuminating of the physical processes occurring at the rock interface, they are not possible to measure in the field. Harmonic generation and frequency dependent behavior are more accessible parameters for field scale measurement techniques. Another measurable effect of this nonlinearity is the production of sidebands, using amplitude modulated driving waveforms. When two waves of different frequencies are summed they do not include the sum and difference of these frequencies, or sidebands. In other words, a frequency space representation of this signal will not have peaks at these sum and difference

frequencies. However if this signal is sent through a nonlinear function, the rock in this case, then the sidebands are produced. Thus measuring sideband production is another metric for nonlinearity, and is related to nonlinear wave mixing phenomena [e.g., *D'Angelo et al.,* 2008, *Johnson and Shankland* 1989, *Meegan et al.,* 1993, *Lawrence et al.,* 2008] and harmonic generation. We measure the harmonic generation with the Total Harmonic Distortion (THD %) [*Ramirez* 1985], defined as the square root of the power of the first 4 harmonics over the square root of the power in the fundamental mode. By quantifying the harmonic generation that determines the stiffening cusp shape and the amount of wave mixing with this degree of nonlinearity, we can interpret nonlinear signals from the field for the physical processes and properties discovered in the more complete data available through lab measurements.

We found the stiffening at the static end of sinusoidal oscillations at all low measured frequencies (0.1 - 6 Hz) (Figure 22a). The cusping effect and harmonic generation diminishes at frequencies greater than or equal to about 8 Hz, a threshold frequency (Figure 22b). The stiffening at the cusp is quantified in blue x's on Figure 22b as the percentage difference in the maximum measured strain and the maximum strain of a periodic fit (at the fundamental frequency) to the data. Also graphed in Figure 22b, in green circles, is the total harmonic distortion (THD %) from the first 4 harmonics, which shows similar frequency dependence. The fact that the stiffening occurs below an equivalent frequency threshold to the change in dispersion described above (Figure 19b) suggests that they may be due to the same frequency dependent mechanism. Although the dispersion data in Figure 19b only includes the fundamental mode, it could be that the low frequency cusp behavior causes a higher measured modulus when present, and thus is responsible for the inverse dispersion below the threshold frequency. This is similar to findings of frictional strength decreasing with frequency below a critical frequency [*Savage and Marone* 2007].
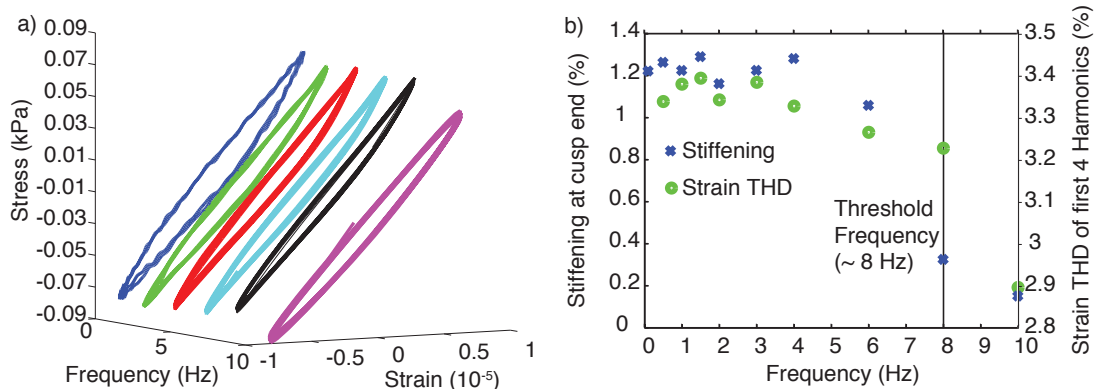
Figure 22. a) Stress-strain hysteresis loops show stiffening cusps at low frequencies, into the page, but not at 10 Hz, in front. **b)** The stiffening (% of periodic fit strain), in blue, and strain total harmonic distortion (THD %), in green, drop around the threshold frequency, ~8 Hz, close to the frequency when dispersion switches in the fundamental data shown in Figure 4b.

As was shown in Figures 21 and 22 above, the harmonic generation occurs under the same conditions as the stiffening cusp shape in the stress-strain hysteresis loop. In fact the shape is caused by the relative power in these harmonics. They are the same

observation; harmonic distortion shows in frequency space what the hysteresis shape shows in time space. Quantitative interpretation of the harmonic signature is outside of the scope of this study, but we note that Figure 21b shows enhanced odd harmonics relative to the expected even harmonics from power law decay. The odd harmonics have a symmetric effect on the hysteresis shape, while even harmonics are not symmetric, so the enhanced odd harmonics are consistent with the predominantly symmetric hysteresis shape.

5.4 Related rock fracture results

Montello granite and Blue Canyon Dome rhyolite were also investigated to evaluate which parts of these behaviors are general and what varies with the rock type and fracture surface geometry. Each of these rocks represents a fractured reservoir or fault of interest, described in methods and materials sections above. The qualitative behavior of the stress-strain hysteresis shape and harmonic generation, the focus of this study, were observed in all the samples at their lowest measurable normal stresses (Figure 23), suggesting these kinds of measurements could be used in a range of rock types. We did observe quantitative differences, for example in the threshold frequency under which the behavior is observed. Past studies have shown qualitatively different frictional behavior for dolomite samples [*Weeks and Tullis* 1985], which will impact the parameterization of the data, but the general behavior is still observed in all of our measured samples under these conditions.
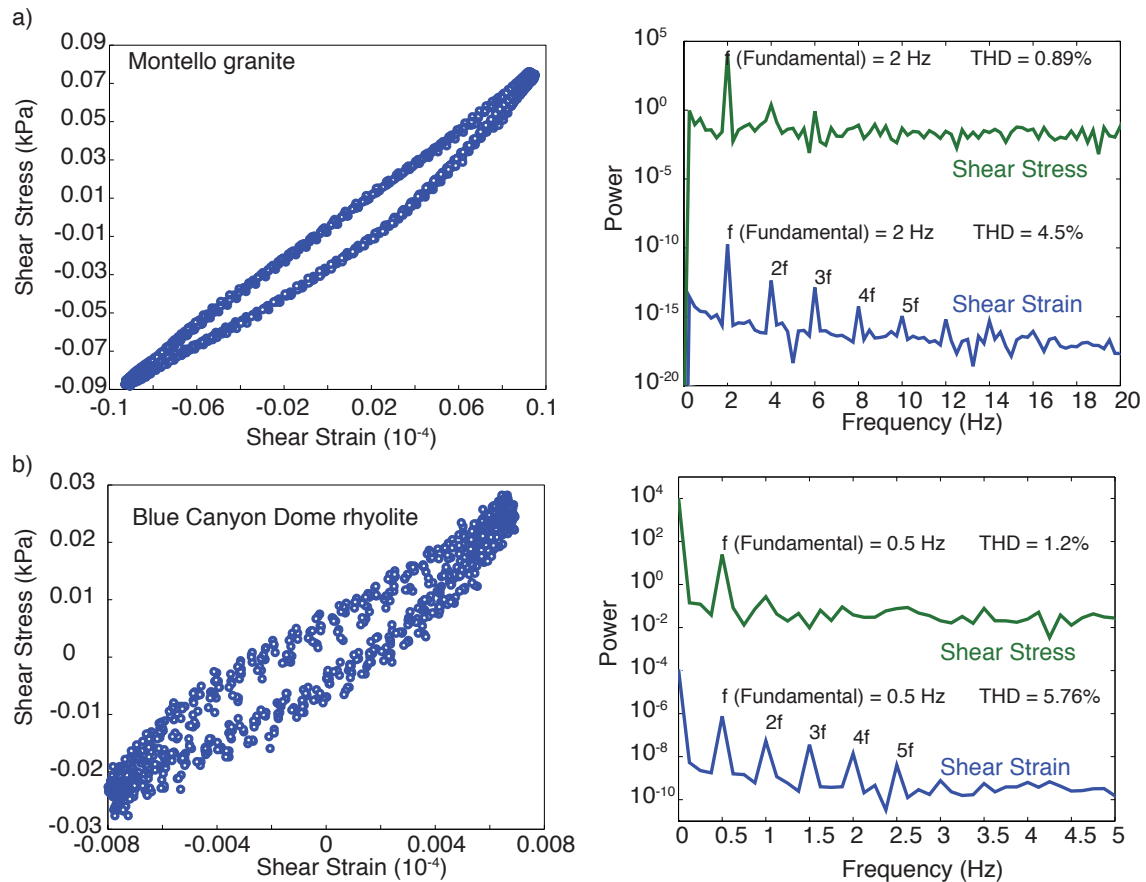
Figure 23. Stress-strain hysteresis loops show similar stiffening cusp behavior for **a)** Montello granite and **b)** Blue Canyon Dome rhyolite. They both also show harmonic generation in the strain, but not in the stress.

6. DYNAMIC FRICTION MODEL

6.1 Mechanism: dynamic to static friction transition

In Chapter 4 we implemented a simple partial slip friction model to fit our fundamental frequency observations of strain-dependent softening with nonlinear constitutive relations (Figures 17a and 18a), but since this type of friction model has no time dependence it cannot explain the rate-dependent observations of our time-series and harmonic generation measurements.

Our hypothesized mechanism comes directly from the time-series measurements of strain (Figure 24a). As the strain-rate oscillates throughout the sinusoidal forcing, the slipping parts of the fracture surface are expected to transition in frictional value related to the rate-dependent friction value of a dynamic friction model. This can be idealized as, and dominated by, transitioning from dynamic to static friction at the zero strain-rate static ends of the sinusoid. The transition to static friction would cause an increase in measured modulus, seen as the bent up cusp at the static end of the stress-strain curve. As the strain-rate increases, partial slip re-nucleates, and the frictional strength of the fracture drops due to the lower value of dynamic friction. This hypothesized mechanism also fits with the observed frequency threshold, where the fracture surface needs to spend sufficient time at low strain-rate for static friction to have an effect.

These measurements take place under partial slip conditions, where regions of the surface asperities are stuck and behave like a linear anelastic material. As the time-series data (Figure 24a) shows, the strain response is dominated by a phase-delayed periodic signal, so the frictional effects on the measured strain are of second order. It is also clear that the loops are closed, returning to the same initial conditions and not drifting over time, even though the stress has an offset, always pushing in the same direction and oscillating the stress on top of this offset. This means the displacement is growing and shrinking but always positive, while the velocity is negative half of the time. For this reason, the stuck regions must be included in the force balance to provide the restoring force that pulls back the slipping regions.

A simple slider-block model best illustrates the force balance, where each component of the system response is represented by an element that has its own parameterization in the equation. To accommodate the stuck asperities, we include a spring holding back the slider block and held fixed on the far side, as shown in Figure 24b. The spring supplies a restoring force in the form of Hooke's law. The slider block represents the frictional resistance on the slipping sections of interface asperities. A dynamic friction model parameterization, described below, is implemented on the block to capture the changes in friction we observe. The slider block is forced with a periodic stressing, which is balanced, mostly, by the spring, representing the stuck asperities, and to second order by friction on the slider block. We model the behavior using a single

block and spring, but these elements each represent many locked and sliding regions. This force balance is expressed in the following equation:

$$\gamma F_d = kx + F_f(v, \theta, model\ parameters) \qquad (18)$$

where γ is a stress concentration factor that scales the bulk shear stress to the shear stress felt by the smaller area asperities, F_d is the periodic driving force, which is converted from our stress data, k is the spring constant that represents the stuck asperities, x is the displacement of the block, which we will be solving for, and F_f is the friction force on the block, a function of slip velocity, v, a state variable, θ, both of which evolve over time, and other model parameters. We use a modified Dahl friction formulation, described below, to solve for the friction force on the sliding block.

The model makes a few key assumptions and simplifications to distill the dynamic frictional behavior of interest. First the inertial term is dropped, because acceleration is assumed small. This is a reasonable assumption since we are using subresonant frequencies. It is inertia that causes resonance; since we are driving the system at low frequencies, the acceleration of the block is negligible. This is the same assumption that is made for all subresonance measurements, equivalent to saying that the stress is transmitted evenly across the sample; see Chapter 2 above. Next, the model is designed for linear slip geometry, while we are slipping in torsion, but each of the asperities individually are deforming linearly in the tangential direction, given our small angular displacements. Although each asperity is experiencing a different forcing depending on its placement on the fracture surface, as shear stress and strain scale with radius, and its interaction with neighboring asperities, these effects are not directly addressed, contributing to the effective nature of parameters in the model fit. The only place in the model that treats the size of asperities is the stress concentration factor, γ, which should depend on the real contact area that stresses are transferred through compared to the total cross-sectional area over which we calculate the bulk stress. The pressure sensitive film measurements give an estimate of the normal stress concentration factor of ~80, where we resolve ~40 MPa normal stresses on individual asperities when the entire fracture is under 0.5 MPa normal stress (Figure 13d). The model fit, described below, requires a stress concentration factor of ~72, consistent with the estimate provided by the pressure sensitive film.
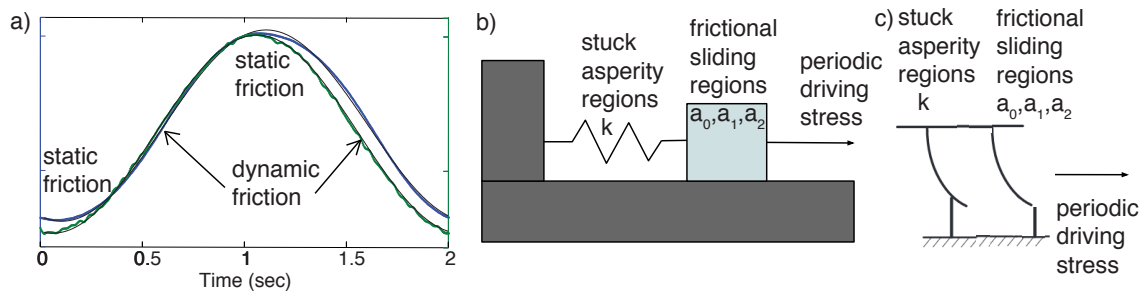
Figure 24. a) Time-series data shows the oscillations in strain-rate that cause transitions between static and dynamic friction. **b)** The slider-block model of the force balance. The periodic driving stress is mostly balanced by a spring representing the stuck centers of the asperities. The spring pulls back on the slider block, which parameterizes the frictionally sliding asperity exteriors. **c)** Our model can also be conceptualized as two effective

bristles, a commonly used analogy for the Dahl model we implement. The stuck regions are represented by bristles that stay elastic; while the slipping areas are represented by bristles that deform elastically at the static ends of the oscillation, and slide when the strain-rates are high enough.

6.2 Modified Dahl model: bristle analogy

Rate-dependent frictional behavior observed in fault friction community from velocity-step experiments is commonly parameterized with the rate-and-state friction model [*Dieterich* 1979, *Ruina* 1983]. This model has also been analyzed using stability theory, predicting the boundary between steady sliding and unstable stick-slip based on the rheological critical stiffness [*Gu et al.,* 1984]. However the rate-and-state formulation is unable to capture static friction or reverse slip because it is numerically unstable at zero or negative slip velocities [*Dieterich* 1979, *Ruina* 1983]. Rate-and-state uses a logarithm of velocity dependence ($F_f \sim \log(v/v_0)$), which means that solving for negative velocities is not possible. Other fault friction models, such as the Brittle-Ductile friction model [*Trugman et al.,* 2013], use a slightly different formulation ($F_f \sim \log(v-v_0/v_0)$), but they still are not symmetric about zero velocity, even giving the frictional force in the wrong direction for reverse slip. Thus a different velocity dependence formulation is necessary to model slip velocity reversals and the effect of static friction.

Other friction models, such as in *Dahl* [1976], have been formulated by the control and dynamics engineering communities to capture reverse slip and zero velocity crossings [*Pennestrì et al.,* 2016, *Péter et al.,* 2014]. The observation of increased static friction at zero velocity is referred to as the Stribeck curve [*Stribeck* 1902] and these models can be modified to capture this behavior [*Canudas de Wit et al.,* 1995]. While it is not the only suitable formulation, the modified Dahl model captures the zero velocity crossing effects, while retaining a form similar to rate-and-state friction. Although it has 6 free parameters, it still has fewer parameters than many other models in this class [*Pennestrì et al.,* 2016]. From our literature search, we found the modified Dahl model to be the simplest model that retains the hypothesized physical processes and whose parameters have some physical interpretation [*Péter et al.,* 2014]. For these reasons, we explore the Dahl friction parameters that would create our observed strain-rate dependent hysteretic stress-strain loops. The focus here is to test whether this model can match the observations, providing support for the hypothesized mechanism and a potential path forward for analyzing the frictional signature in this type of data.

As the Dahl friction formulation is uncommon in the earth science literature we describe a little of its physical basis. The Dahl model is in the class of 'bristle' friction models. These models describe the onset of frictional sliding as the initial elastic deformation and subsequent permanent displacement of a bristle, such as on a brush. This analogy is also useful in describing partial slip. A bristle that never reaches slipping conditions could describe the stuck regions of the asperities, in place of the spring. Our force balance, Figure 24b and equation 18, could be illustrated with two different bristles in series, one of which never slips, equivalent to the spring, while the other sticks at low velocities than slides frictionally above a characteristic velocity, v_s, captured in the slider block's frictional parameterization, Figure 24c. This characteristic velocity defines the

velocity range over which the higher static friction value is applied. The model includes these essential features - a continuous function around zero velocity, which is numerically stable, and velocity dependence that fits the Stribeck curve, which shows higher friction values at low velocities representing the effect of static friction. The modified Dahl model [*Canudas de Wit et al.,* 1995] is given in the following equations:

$$F_f = a_2 \frac{v}{v_0} + \theta \tag{19}$$

where a_2 is the viscous friction parameter, because it gives the proportionality between the friction force and velocity. The state variable (θ), with units of force, evolves based on the following equation:

$$\frac{d\theta}{dt} = \frac{-abs[v]\theta}{L} + a_0 \frac{v}{L} + a_1 \frac{v}{L} e^{-(\frac{v}{v_s})^2} \tag{20}$$

where L is a constant with dimensions of length related to the critical slip distance, v_s is the characteristic (Stribeck) velocity, described above, a_0 is the Coulomb friction parameter, and a_1 is the Stribeck friction parameter, defining the weight of the static friction effect.

6.3 Comparison of model to observations

We want to test if the modified Dahl model is able to capture the general nonlinear shape of our observed hysteresis loops at low frequency, with the right choice of parameters. To solve this set of ordinary differential equations (18-20), we use a real-valued variable-coefficient solver, with fixed-leading-coefficient implementation, VODE in the scipy package [*Brown et al.,* 1989]. Since there is a large parameter space, we used the python package S-timator [*Ferreira* 2015], which implements a differential evolution genetic optimizer [*Storn and Price* 1997]. To find parameters that match the observations we allowed all the slider block model parameters, as well as the initial strain and strain rate, to vary. Only the length constant, L, was held fixed to $3\text{x}10^{-6}$ m (similar to estimates of the critical slip distance from *Saltiel et al.,* [2017b]). The model was driven with a linearized forcing from the measured stress data, Figure 20. This was not a thorough inversion; we focused on confirming the models ability to reproduce the observation using reasonable parameters.

The model results are shown in Figure 25, using the following best-fit parameter values: $a_0 = 2.9\text{x}10^{-6}$ N, $a_1 = 16$ N, $a_2 = 2$ N, $\gamma = 72$, $k = 4.5\text{x}10^6$ N/m, $v_s = 7.3\text{x}10^{-8}$ m/s, and $v_0 = 1.3\text{x}10^{-5}$ m/s. Figure 10a shows the direct comparison between the modeled and observed stress-strain hysteresis loops. The modeled stress and strain oscillations are shown in Figure 10c and the frequency spectrum are shown in Figure 10d. The model is not able to fit both the middle of the oscillation and the cusped ends with the same set of parameters. The key to fitting the cusped part of the data was to fit the strain rate, not the strain, from the data, effectively weighting the ends over the other parts of the sinusoid. The model results mimic the symmetric part of the stiffening shape, resulting only from odd harmonic generation, but cannot generate even harmonics. This suggests that the even harmonics in the observations are due to higher order, non-symmetric, physical mechanism, not captured by this model. A possible non-symmetric mechanism, not included in the model, is the direct strain-dependent softening (Figure 17a). This softening could cause the lower stress values in the center of the experimental hysteresis

loop, compared to that from the model, fully symmetric, results (Figure 25a). The slightly less defined stiffening at the low strain static end compared to the high strain end (Figure 25a) could also be effect of direct strain-dependent softening. A model that also captured this direct strain dependence should generate even harmonics and better fit the observations.

Both through the physical interpretation of the parameters and numerous forward model runs with varying parameters, we find that a_1 and v_s have the greatest effect on the hysteresis shape, while the balance of the other parameters mostly affects the amplitude, saturation, drift, and damping of the resulting strain. The low value of a_0 suggests the minimal importance of Coulomb friction. The velocities between v_s and v_0 are where we expect to see the effect of static friction. Since the model has many parameters, there are many different regimes of parameter space that show varied behavior. The similarity of the results suggests that the model is able to capture the basic processes in our experiments at these conditions.
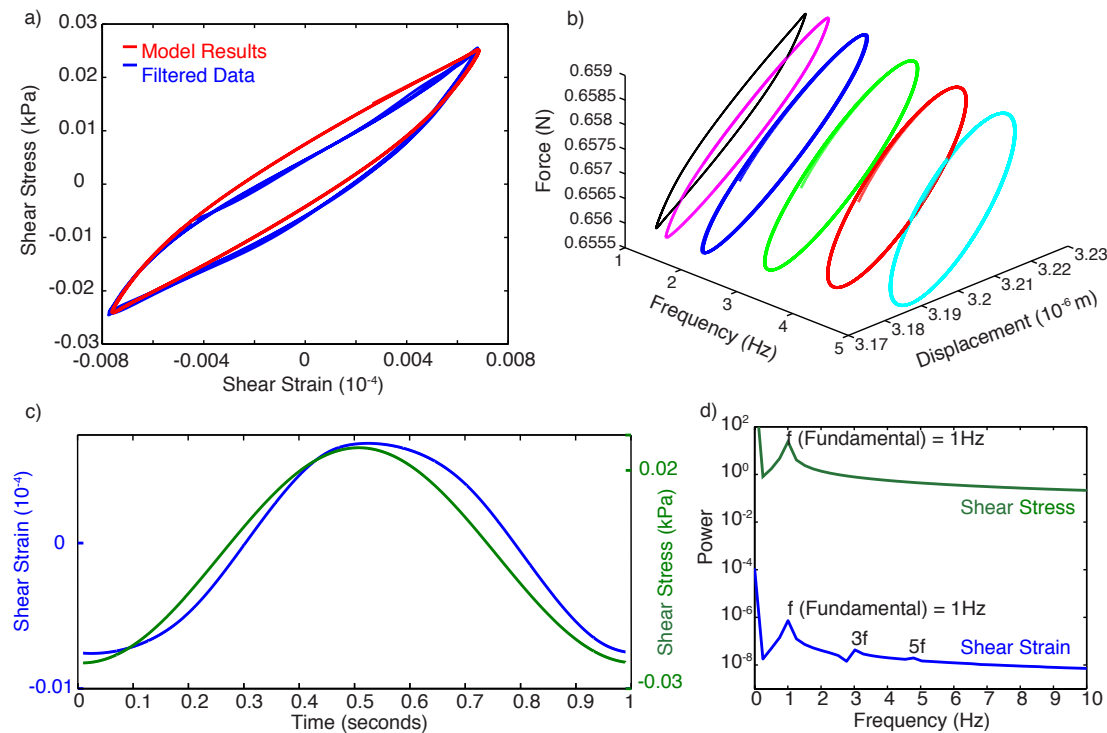
Figure 25. The model results with the best-fit parameters given in text. **a)** Stress-strain hysteresis loop from model (red) compared to our data (blue). **b)** Modeled hysteresis loop shapes show a continuous decrease of cusp shape and increase of phase delay with frequency. **c)** The model predicted time-series of strain (blue) given a periodic driving stress (green) and **d)** the frequency space representations. The strain only exhibits odd harmonic generation, while the stress has no harmonics because a periodic forcing is used. The model generates smaller harmonics than the data and only odd harmonics, suggesting that the even harmonics are due to another, non-symmetric, mechanism.

To better understand the model behavior, we focus on this set of parameters that best fit our data but with different forcing frequencies. The modified Dahl model results also show frequency-dependence (Figure 25b), but the high frequency behavior is different from our experimental results. Instead of exhibiting a threshold frequency, around 8 Hz for the dolomite fracture, the hysteresis loop undergoes a more gradual change in shape with frequency, and it begins at slightly lower frequencies, ~2 Hz, than the data. The stiffening cusp diminishes with frequency as the measurements show, but it is accompanied by a growing phase delay, which is not present in our experimental data. These effects are clear in the high frequency large ellipses (Figure 25b), which eventually grow to circles, phase delay of 45°, at even higher frequencies, not shown. Finding the fitting parameters for the data at each frequency independently could show the frequency dependence of each parameter. Another possibility is that a more complicated model could better capture our experimental high frequency behavior. Higher driving frequencies cause higher slip velocities, greater than v_0, so a compound model with a rate-and-state friction formulation above v_0 and the modified Dahl model for lower slip velocities, at the static friction condition, would change this high frequency behavior. Future work will explore model variations and their parameter regimes, employing stability theory to understand the transitions between regimes and their dependence on the balance of model parameters. Better understanding of the behavior of the many model parameters will allow consistent data parameterization, quantifying the dynamic friction signature of lab and, eventually, field data. To do this properly may also require accounting for the complex surface and asperity geometry.

6.4 Conclusions

We present seismic-frequency torsional oscillations of stress and strain on rock fractures under low normal stresses, conditions that have been shown to produce partial slip on the outside of asperities while the centers remain stuck and elastic. Our results suggest the signature of dynamic friction, variations in friction or stiffness as strain-rate oscillates during the periodic driving stress. This process is most apparent in our measured strain time-series compared to a periodic fit. The largest deviation from the fit is when the strain falls short of reaching the expected peak at the static end where strain-rate goes through zero. The dominant frictional effect is due to static friction at this static end transitioning to and from dynamic friction in the higher strain-rate parts of the cycle. The stress-strain hysteretic loop shape expresses this effect with stiffening cusps at the static ends. This nonlinear hysteresis is accompanied by harmonic generation in the strain, while the stress remains linear, confirming that the driver and electronics are not the source of the nonlinearity. Lastly, the observed frequency dependence also supports this mechanism. We see stiffening cusps, harmonic generation, and modulus decreases with frequency at low frequencies (< 8 Hz), while the higher frequencies retain more linear hysteresis shapes, lower harmonic generation, and normal dispersion. We interpret that this shows longer periods, lower frequencies, are needed to spend sufficient healing time at low strain-rates for the static friction to have an effect. Otherwise, at high frequency, the slipping parts of the fracture keep slipping and the fracture lacks the added nonlinear hysteresis and stiffening. Since low-frequency apparatuses are rare, especially for measuring fractures under low normal stress, these results suggests there may be physical processes that are being missed by higher frequency experiments.

Taking advantage of model development in the dynamics and control engineering communities, we adapt a modified Dahl model to capture the described mechanism and show the parameters necessary for the observed behavior. This 'bristle' model, coupled to a spring describing the stuck parts of the asperities, is able to show the effect of higher static friction as strain-rate is reversed through zero, known as the Stribeck effect. Although not unique given the large number of parameters, the Dahl model produces qualitatively similar strain oscillations and hysteresis loops, given a periodic driving stress. The Dahl model is also attractive because it has a similar functional form to rate-and-state friction, allowing data parameterizations to be compared to rate-and-state friction parameters commonly used to describe fault and earthquake nucleation behavior. The rate-and-state friction model itself cannot be applied to these measurements because it is unable to model zero velocity or velocity reversals. More work on models that include both formulations and stability analysis is needed to parameterize data in a way that allows field measurement of dynamic friction properties.

These results provide a path for using high amplitude, active source seismic methods, such as provided by time reversal techniques, to probe frictional properties in reservoir fractures and faults in the field. There are also implications for the characterization and underlying physical processes of bulk nonlinear elasticity in earth materials, suggesting fast and slow dynamics are related to dynamic frictional effects such as ageing and healing. Although it will be challenging to measure stress-strain time-series or hysteresis loops in the field, the accompanying harmonic and sideband generation could be measurable with repeatable crosswell surveys where strains in the 10^{-5} range can be achieved with appropriate high energy sources. The fact that the frequency-dependence occurs in the seismic frequency band suggests that these effects could be measured directly in the field. Such an approach could potentially provide spatially resolved constraints on the frictional behavior (such as velocity strengthening or weakening properties) of critically stressed faults in the absence of seismicity.

7. REFERENCES

Afferrante, L., Carbone, G., and G. Demelio (2011), Interacting and coalescing Hertzian asperities: a new multiasperity contact model: Wear, 278-279, 28-33.

Aki, K. and P.G. Richards (2002), Quantitative seismology 2nd edition: University Science Books.

Anderson, T.W. and D.A. Darling (1954), A test of goodness-of-fit: Journal of the American Statistical Association, 49, 765–769.

Archard, J.F. (1961), Single contacts and multiple encounters: Journal of Applied Physics, 32, 1420-1425.

Batzle, M.L., D-H. Han, and R. Hofmann (2006), Fluid mobility and frequency dependent seismic velocity - Direct measurements: GEOPHYSICS, 71, N1-N9.

Bear, J. (1972), Dynamics of fluids in porous media: Dover Publications, New York, NY.

Berckhemer, H., Kampfmann, K., Aulbach, E., and H. Schemling (1982), Shear modulus and Q of forsterite and dunite near partial melting from forced oscillation experiments: Physics of Earth and Planetary Interiors, 29, 30-41.

Berthoude P. and T. Baumberger (1999), Shear stiffness of a solid solid multicontact interface: Proccedings of the Royal Society of London A, 454, 1615-1634.

Boitnott, G.N., Biegel, R.L., and C.H. Scholz (1992), Micromechanics of rock friction 2: quantitative modeling initial friction with contact theory: Journal of Geophysical Research, 97, 8965-8978.

Biot, M.A. (1941), General theory of three-dimensional consolidation: Journal of Applied Physics, 12, 155.

Biot, M.A. (1956), Theory of propagation of elastic waves in a fluid saturated porous solid. I. Low frequency range and II. Higher-frequency range: Journal of the Acoustic Society of America, 28, 168-191.

Birch, F. (1960), The velocity of compressional waves in rocks to 10 kilobars: Journal of Geophysical Research, 65, 1083-1102.

Birch, F., and D. Bancroft (1938), Elasticity and internal friction in a long column of granite: Bulletin of the Seismological Society of America, 28, 4, 243-254.

Bonner, B.P., and B.J. Wannamaker (1991a), Acoustic nonlinearities produced by a single macroscopic fracture in granite, *in* D.O. Thompson and D.E. Chimenti, eds., Review of Progress in Quantitative Nondestructive Evaluation Volume 10B: Springer US, 1861-1876.

Bonner, B.P., and B.J. Wannamaker (1991b), Nonlinear attenuation effects outside the zone of macroscopic failure: Monograph on Explosion Source Phenomenology American Geophysical Union, 65, 91-97.

Boitnott, G.N., Biegel, R.L., Scholz, C.H., Yoshioka, N., and W. Wang (1992), Micromechanics of Rock Friction 2: Quantitative Modeling of Initial Friction With Contact Theory, J. Geophys. Res., 97, B6, 8965-8978.

Bowden, F.P. and D. Tabor (2001), The friction and lubrication of solids: Oxford University Press.

Brodsky, E.E., and N.J. van der Elst (2014), The uses of dynamic earthquake triggering, Annual Review of Earth and Planetary Sciences, 42, 317-339, DOI: 10.1146/annurev-earth-060313-054648.

Brodsky, E.E., Kirpatrick, J.D., and T. Candela (2016), Constraints from fault roughness on the scale-dependent strength: Geology, 44, 19-22.

Brown, P.N., G.D. Byrne, and A.C. Hindmarsh (1989), VODE: A variable coefficient ODE solver, SIAM J. Sci. Stat. Comput., 10, 1038-1051.

Brown, S.R. and C.H. Scholz (1985), Broad bandwidth study of the topography of natural rock surfaces: Journal of Geophysical Research, 70, 12575-12582.

Brown, S.R., Kranz, R.L. and B.P. Bonner (1986), Correlation between the surfaces of natural rock joints: Geophysical Research Letters, 13, 1430-1433.

Campañá, C., Persson, B.N.J., and M.H. Müser (2011), Transverse and normal interfacial stiffness of solids with randomly rough surfaces: Journal of Physics: Condensed Matter, 23, 1-9.

Canudas de Wit, C., H. Olsson, K.J. Astrom, and P. Lischinsky (1995), A new model for control of systems with friction, IEEE Transactions on Automatic Control, 40, 3, 419-425.

Capodagli, J., and R. Lakes (2008), Isothermal viscoelastic properties of PMMA and LDPE over 11 decades of frequency and time: a test: Rheologica Acta, 47, 777-786.

Candela, T., Renard, F., Bouchon, M., Brouste, A., Marson, D., Schmittbuhl, J., and C. Voisin (2009), Characterization of fault roughness at various scales: implications for three-dimensional high resolution topography measurements: Pure Applied Geophysics, 166, 1817-1852.

Carnevale, E.H., Lynnworth, L.C., and G.S. Larson (1964), Ultrasonic measurement of elastic moduli at elevated temperatures, using momentary contact: The Journal of the Acoustical Society of America, 36, 1678-1684.

Chen, J. H., B. Froment, Q.Y. Liu, and M. Campillo (2010), Distribution of seismic wave speed changes associated with the 12 May 2008 Mw 7.9 Wenchuan earthquake, Geophys. Res. Lett., 37, 2008–2011.

Clark, V.A., Tittmann, B.R., and T.W. Spencer (1980), Effect of volatiles on attenuation (Q^{-1}) and velocity in sedimentary rocks: Journal of Geophysical Research, 85, 5190-5198.

Cooper, H.W. (1979), Attenuation in igneous rocks at seismic frequencies: PhD Thesis, Massachusetts Institute of Technology.

D'Angelo, R.M., K.W. Winkler, and D.L. Johnson (2008), Three wave mixing test of hyperelasticity in highly nonlinear solids: Sedimentary rocks, J. Acoust. Soc. Am., 123 (2), 622-639; doi: 10.1121/1.2821968.

Dahl, P.R. (1976), Solid friction damping in mechanical vibrations, AIAA J. 14, 1675-1682.

David, E.C., N. Brantut, A. Schubnel, R.W. Zimmerman (2012), Sliding crack model for nonlinearity and hysteresis in the uniaxial stress-strain curve of rock. International doi:10.1016/j.ijrmms.2012.02.001

Davis, R.O., and A.P.S. Selvadurai (1996), Elasticity and geomechanics: Cambridge University Press.

Delorey, A.A., N.J. van der Elst, and P.A. Johnson (2016), Tidal triggering of earthquakes suggests poroelastic behavior on the San Andreas Fault, Earth and Planetary Science Letters, 460, 164-170, doi.org/10.1016/j.epsl.2016.12.014.

Dieterich, J. H. (1979), Modeling of rock friction: 1. Experimental results and constitutive equations, J. Geophys. Res., 84(B5), 2161–2168, doi:10.1029/JB084iB05p02161.

Dou, S., J. Ajo-Franklin, T. Daley, M. Robertson, T. Wood, B. Freifeld, R. Pevzner, J. Correa, K. Tertyshnikov, M. Urosevic, and B. Gurevich (2016), Surface orbital vibrator (SOV) and fiber-optic DAS: Field demonstration of economical, continuous-land seismic time-lapse monitoring from the Australian CO2CRC Otway site: Society of Exploration Geophysics Technical Program Expanded Abstracts 2016, pp. 5552-5556.

Duffaut, K., M. Landrø, and R. Sollie (2010), Using Mindlin theory to model friction-dependent shear modulus in granular media, Geophysics, 75, 3, E143-E152.

Favrie, N., B. Lombard, and C. Payan (2015), Fast and slow dynamics in a nonlinear elastic bar excited by longitudinal vibrations, Wave Motion, 56, 221–238.

Ferrira, A.E.N. (2016), S-timator, http://webpages.fc.ul.pt/~aeferreira/stimator/index.html/ [Online; accessed 2017-03-17]

Ferry, J.D. (1980), Viscoelastic properties of polymers 3rd edition: John Wiley & Sons.

Gliozzi, A., and M. Scalerandi (2014), Modeling dynamic acousto-elastic testing experiments: Validation and perspectives, J. Acoust. Soc. Am., 136(4), 1530–1541.

Gordon, R.B., and L.A. Davis (1968), Velocity and attenuation of seismic waves in imperfectly elastic rock: Journal of Geophysical Research, 73, 3917-3935.

Gordon, R.B., and D. Rader (1971), Imperfect elasticity of rock: Its influence on the velocity of stress waves, in The Structure and Physical Properties of the Earth's Crust, Geophys. Monogr. Ser., vol.14, edited by J.G. Heacock, p. 235, AGU, Washington, D.C.

Greenwood, J.A. and J.B.P. Williamson (1966), Contact of nominally flat surfaces: Proceedings of the Royal Society of London, 295, 300-319.

Gribb, T.T. and R.F. Cooper (1998), A high-temperature torsion apparatus for the high-resolution characterization of internal friction and creep in refractory metals and

ceramics: application to the seismic-frequency, dynamic response of Earth's upper mantle: Review of scientific instruments, 69, 559-564.

Gu, J., J.R. Rice, A.L. Ruina, and S.T., Tse (1984), Slip motion and stability of a single degree of freedom elastic system with rate and state dependent friction, Journal of the Mechanics and Physics of Solids, 32, 3, 167-196.

Gusev, V., and V. Tournat (2005), Amplitude- and frequency-dependent nonlinearities in the presence of thermally-induced transitions in the preisach model of acoustic hysteresis, Phys. Rev. B, 72(5), 54104.

Guyer, R., and P. Johnson (2009), Nonlinear Mesoscopic Elasticity: The Complex Behaviour of Rocks, Soil, Concrete, 395 pp., Wiley Vch Publ., Hoboken, N. J.

Guyer, R., K. McCall, and G. Boitnott (1995), Hysteresis, discrete memory and nonlinear wave propagation in rock, A new paradigm, Phys. Rev. Lett., 74, 3491–3494.

Guyer, R. A., K. R. McCall, G. N. Boitnott, L. B. Hilbert, and T. J. Plona (1997), Quantitative implementation of preisach-mayergoyz space to find static and dynamic elastic moduli in rock, J. Geophys. Res., 102, 5281–5293.

Haimson, B.C. (1975), Deep in-situ stress measurements by hydrofracturing: Tectonophysics, 29, 41-47.

Hansen, A., Schmittbuhl, J., Batrouni, G.G., and F.A. de Oliveira (2000), Normal stress distribution of rough surfaces in contact: Geophysical Research Letters, 27, 3639-3642.

Hardin, E. L., C. H. Cheng, F. L. Paillet, and J. D. Mendelson (1987), Fracture characterization by means of attenuation and generation of tube waves in fractured crystalline rock at Mirror Lake, New Hampshire: Journal of Geophysical Research, 92, B8, 7989–8006.

Hertz, H. (1882), On the contact of firm elastic bodies: Journal Reine Angewandte Mathematik, 92, 156-171.

Holcomb, D.J. (1981), Memory, relaxation, and microfracturing in dilatant rock, J. Geophys. Res., 86, B7, 6235-6248.

Jackson, I. (2000), Laboratory measurement of seismic wave dispersion and attenuation: recent progress: Earth's deep interior: mineral physics and tomography from atomic to the global scale: Geophysical Monograph 117, 265-389.

Jackson, I. and M.S. Paterson (1993), A high-pressure, high-temperature apparatus for studies of seismic wave dispersion and attenuation: Pure and Applied Geophysics, 141, 445-466.

Jackson, I., Paterson, M.S., Niesler, H., and R.M. Waterford (1984), Rock anelasticity measurements at high pressure, low strain amplitude and seismic frequency: Geophysical Research Letters, 11, No.12, 1235-1238.

Jackson, I., Schijns, H., Schmitt, D.R., Mu, J., and A. Delmenico (2011), A versatile facility for laboratory studies of viscoelastic and poroelastic behavior of rocks: Review of Scientific Instruments, 82, 1-8.

Jaeger, J.C., and N.G.W. Cook (1969), Fundamentals of rock mechanics: Chapman and Hall Limited.

Johnson, K.L. (1985), Contact mechanics: Cambridge University Press.

Johnson, P.A., and T.J. Shankland (1989), Nonlinear generation of elastic waves in granite and sandstone: continuous wave and traveltime observations, Journal of Geophysical Research, 94, 17729-17734.

Johnson, P.A., J. Carmeliet, H.M. Savage, M. Scuderi, B.M. Carpenter, R.A. Guyer, E.G. Daub, and C. Marone (2016) Dynamically triggered slip leading to sustained fault gouge weakening under laboratory shear conditions, Geophysical Research Letters 43, 1559-1565, doi:10.1002/2015GL067056.

Katahara, K. W., Manghnani, M. H., Devnani, N., and B. R. Tittmann (1982), Pressure dependence of Q in selected rocks: Advances in Earth and Planetary Science, _12_, 147-158.

Kazimierz, T., T. Jacek, and R. Stanislaw (2004), Evaluation of rock porosity measurement accuracy with a Helium porosimeter: Acta Montanistica Slovaca, 3, 316-318.

Koppelmann, V.J. (1958), Uber die bestimmung des dynamichen elastizitatsmoduls und des dynamischen schubmodulus im frequenzbereich von 10−5 bis 10−1 Hz: Rheologica Acta, 1, 20–28.

Knox, H. A., J. B. Ajo-Franklin, T. C. Johnson, J. P. Morris, M. C. Grubelich, L. A. Preston, J. M. Knox, and D. K. King (2016), Imaging fracture networks using joint seismic and electrical change detection techniques, Proceedings of the 50th US Rock Mechanics Geomechanics Symposium, Houston, TX, American Rock Mechanics Association.

Lakes, R.S., 2004, Viscoelastic measurement techniques: Review of Scientific Instruments, 75, 797-810.

Landau, L., and E. Lifshitz (1986), Theory of Elasticity—Third Edition (Course of Theoretical Physics, Volume 7), 1–195 pp., Butterworth-Heinemann, Oxford.

Lawrence, Z., P. Bodin, C. Langston, F. Pearce, J. Gomberg, P. Johnson, F.-Y. Meng, and T. Brackman (2008), Induced dynamic ground response at Garner Valley, California, Bulletin of the Seismic Society of America, 98, 1412-1428.

Li, Q., T.E. Tullis, D. Goldsby, and R.W. Carpick (2011), Frictional ageing from interfacial bonding and the origins of rate and state friction, Nature, 480, 233-236.

Li, Y., M. Olin, E.C. David, I. Jackson, H. Schijns, and D.R. Schmitt, 2014, Broadband laboratory measurements of dispersion in thermally cracked and fluid-saturated quartzite and a synthetic analogue: The Leading Edge, 33, 936-941.

Lockner, D.A., Walsh, J.B., and J.D. Byerlee (1977), Changes in seismic velocity and attenuation during deformation of granite: Journal of Geophysical Research, 82, 5374-5378.

Lubbe, R., Sothcott, J., Worthington, M.H. and C. McCann (2008), Laboratory estimates of normal and shear fracture compliance: Geophysical Prospecting, 56, 239–247.

Majer, E.L., Peterson, J.E., Daley, T., Kaelin, B., Myer, L., Queen, J., D'Onfro, P., and W. Rizer (1997), Fracture detection using crosswell and single well surveys: GEOPHYSICS, 62, 2, 495-504.

Marone, C. (1998), Laboratory-derived friction laws and their application to seismic faulting, Annual Review of Earth and Planetary Science, 26, 643-696.

Mavko, G., and D. Jizba (1991), Estimating grain-scale fluid effects on velocity dispersion in rocks: GEOPHYSICS, 56, 1940-1949

Mavko, G., T. Mukerji, and J. Dvorkin (1998), The rock physics handbook: tools for seismic analysis in porous media: Cambridge University Press.

Mavko, G.M. (1979), Frictional attenuation: an inherent amplitude dependence, Journal of Geophysical Research, 84, B9, 4769-4775.

Mavko, G., T. Mukerji, and J. Dvorkin (2009), The rock physics handbook: tools for seismic analysis of porous media: Cambridge University Press.

McCann, C., and J. Sothcott, 2009, Sonic to ultrasonic Q of sandstones and limestones: Laboratory measurements at in situ pressures: GEOPHYSICS, 74, 2, WA93-WA101.

McKavanagh, B. and F.D. Stacey (1974), Mechanical hysteresis in rocks at low strain amplitudes and seismic frequencies, Physics of Earth and Planetary Interiors, 8, 3, 246-250.

Mindlin, R. D. (1949), Compliance of elastic bodies in contact, Journal of Applied Mechanics, 6.

Misra, A. and S. Huang (2012), Micromechanical stress-displacement model for rough interfaces: effect of asperity contact orientation on closure and shear behavior: International Journal of Solids and Structures, 49, 111-120.

Moore, D.E., and D.A. Lockner (1995), The role of microcracking in shear-fracture propagation in granite: Journal of Structural Geology, 17, 1, 95-114.

Morris, J.P. (2015), Numerical investigation of the relationship between fracture shear compliance and conductivity anisotropy: Proceedings of 49th US Rock Mechanics Geomechanics Symposium, San Francisco, CA, American Rock Mechanics Association. ARMA 15-554.

Nakagawa, S. (2011), Split Hopkinson resonant bar test for sonic frequency acoustic velocity and attenuation measurement of small, isotropic geologic samples: Review of Scientific Instruments, 82, 1-13.

Nakagawa, S. (2013), Low-frequency (<100 Hz) dynamic fracture compliance measurement in the laboratory: Proceedings of 47th US Rock Mechanics Geomechanics Symposium, San Francisco, CA, American Rock Mechanics Association. ARMA 13-343.

Nakagawa, S., Nakashima, S. and V. A. Korneev (2016), Laboratory measurements of guided-wave propagation within a fluid-saturated fracture: Geophysical Prospecting, 64, 143–156.

Niu, F., P. G. Silver, T. M. Daley, X. Cheng, and E. L. Majer (2008), Preseismic velocity changes observed from active source monitoring at the Parkfield SAFOD drill site, Nature, 454, 204–208.

Norwick, A.S. and Berry, B.S. (1961), Lognormal distribution function for describing anelastic and other relaxation process: I. Theory and numerical computations: IBM Journal of Research and Development, 5, 297-311.

Nur, A., and G. Simmons (1969), The effect of viscosity of a fluid phase on velocity in low porosity rocks: Earth and Planetary Science Letters, 7, 99-108.

Oberg, E., Jones, F.D., Horton, H.L., and H.H. Ryffel (2008), Machinery's handbook, 28th edition: Industrial Press.

O'Donnell, M., E.T. Jaynes, and J.G. Miller (1981), Kramers-Kronig relationship between ultrasonic attenuation and phase velocity, The Journal of the Acoustical Society of America, 69 (3), 696-701.

Oliger, A., Nolte D.D., and L.J. Pyrak-Nolte (2003), Seismic focusing by a single planar fracture: Geophysical Research Letters, 30, 5, 1203.

Paggi, M., R. Pohrt, and V.L. Popov (2014), Partial-slip frictional response of rough surfaces, Scientific Reports, 4, 1-6, DOI: 10.1038/srep05178.

Pecorari, C. (2015), A constitutive relationship for mechanical hysteresis of sandstone materials, Proc. R. Soc. A, 471, 20150369, doi:10.1098/rspa.2015.0369.

Pennestrì, E., V. Rossi, P. Salvini, and P.P. Valentini (2016), Review and comparison of dry friction force models, Nonlinear Dyn., 83, 1785-1801, DOI 10.1007/s11071-015-2485-3.

Persson, B.N.J., Bucher, F. and B. Chiaia (2002), Elastic contact between randomly rough surfaces: comparison of theory with numerical results: Physical Review B, 65, 1-7.

Persson, B.N.J. (2006), Contact for randomly rough surfaces: Surface Science Reports, 61, 201-227.

Peselnick L., and H.-P. Liu (1987), Laboratory measurement of internal friction in rocks and minerals at seismic frequencies: In Methods of Experimental Physics, 24, 349-369.

Pohrt, R. and V.L. Popov (2012), Normal contact stiffness of elastic solids with fractal rough surfaces: Physical Review Letters, 108, 1-4.

Power, W.L. and T.E. Tullis (1991), Euclidean and fractal models for the description of rock surface roughness: Journal of Geophysical Research, 96, 415-424.

Pride, S.R., J.H. Harris, D.L. Johnson, A. Mateeva, K.T. Nihei, R.L. Nowack, J.W. Rector, H. Spetzler, R. Wu, T. Yamomoto, J.G. Berryman, and M. Fehler (2003), Permeability dependence of seismic amplitudes, The Leading Edge, 22, 518–525.

Pyrake-Nolte, L.J., L.R. Meyer, and N.G.W. Cook (1990), Transmission of seismic waves across single natural fractures: Journal of Geophysical Research, 95, 8617-8638.

Pyrake-Nolte, L.J. and D.D. Nolte (1992), Frequency dependence of fracture stiffness: Geophysical Research Letters, 19, 325-328.

Pyrake-Nolte, L.J. (1996), The seismic response of fractures and the interrelations among fracture properties, International Journal of Rock Mechanics, Mining Science, and Geomechanics, 33, 8, 787-802.

Pyrake-Nolte, L.J. and J.P. Morris (2000), Single fractures under normal stress: The relation between fracture specific stiffness and fluid flow, International Journal of Rock Mechanics and Mining Science, 37, 245-262.

Pyrake-Nolte, L.J. and D.D. Nolte (2016), Approaching a universal scaling relationship between fracture stiffness and fluid flow, Nature Comm., 7, 1-6, doi:10.1038/ncomms10663.

Ramirez, R.W. (1985), The FFT: Fundamentals and concepts, Tektronix, Inc., Englewood Cliffs, NJ.

Reches, Z., and D.A. Lockner (1994), Nucleation and growth of faults in brittle rocks: Journal of Geophysical Research, 99, B9, 18159-18173.

Remillieux, M.C., R.A. Guyer, C. Payan, and T.J. Ulrich (2016), Decoupling nonclassical nonlinear behavior of elastic wave types, Phys. Rev. Lett., 116, 115501.

Rivet, D., M. Campillo, N. M. Shapiro, V. Cruz-Atienza, M. Radiguet, N. Cotte, and V. Kostoglodov (2011), Seismic evidence of nonlinear crustal deformation during a large slow slip event in Mexico, Geophys. Res. Lett., 38, L08308, 3-7.

Rivière, J., G. Renaud, R.A. Guyer, and P.A. Johnson (2013), Pump and probe waves in dynamic acousto-elasticity: Comprehensive description and comparison with nonlinear elastic theories, Journal of Applied Physics, 114, 054905.

Rivière, J., P. Shokouhi, R. A. Guyer, and P. A. Johnson (2015), A set of measures for the systematic classification of the nonlinear elastic behavior of disparate rocks, J. Geophys. Res. Solid Earth, 120.

Rivière, J., L. Pimienta, M. Scuderi, T. Candela, P. Shokouhi, J. Fortin, A. Schubnel, C. Marone, and P.A. Johnson (2016a), Frequency, pressure, and strain dependence of nonlinear elasticity in Berea Sandstone, Geophysical Research Letters, 43, 7, 3226-3236.

Rivière, J., P. Shokouhi, R.A. Guyer, and P.A. Johnson (2016b), Fast and slow nonlinear elastic response of disparate rocks and the influence of moisture, The Journal of the Acoustical Society of America, 140, 4, 3326, doi:10.1121/1.4970596.

Ruina, A. (1983), Slip instability and state variable friction laws, J. Geophys. Res., 88, B12, 10,359-10,370

Rutledge, J.T., and W.S. Phillips (2003), Hydraulic stimulation of natural fractures as revealed by induced microearthquakes, Carthage Cotton Valley gas field, east Texas, Geophysics, 68(2), 441-452.

Saltiel, S., P.A. Selvadurai, B.P. Bonner, S.D. Glaser, and J.B. Ajo-Franklin (2017a), Experimental development of low-frequency shear modulus and attenuation

measurements in mated rock fractures: shear mechanics due to asperity contact area changes with normal stress, Geophysics, 82, 2, 1-18. 10.1190/GEO2016-0199.1

Saltiel, S., B.P. Bonner, and J.B. Ajo-Franklin (2017b), Strain-dependent partial slip on rock fractures under seismic-frequency torsion, Geophysical Research Letters, 44, DOI:10.1002/2017GL073108.

Saltiel, S., B.P. Bonner, T. Mittal, B. Delbridge, J. Ajo-Franklin, (2017c), Experimental evidence for dynamic friction on rock fractures from frequency-dependent nonlinear hysteresis and harmonic generation, Journal of Geophysical Research – Solid Earth, DOI: 10.1002/2017JB014219.

Savage, J.C. (1969), Comment on 'Velocity and attenuation of seismic waves in imperfectly elastic rock' by R.B. Gordon and L.A. Davis, J. Geophys. Res., 74, 726-728.

Savage, H.M. and C. Marone (2007), Effects of shear velocity oscillations on stick-slip behavior in laboratory experiments, J. Geophys. Res., 112, B2, DOI:10.1029/2005JB004238

Savage, H.M. and C. Marone (2008), Potential for earthquake triggering from transient deformations, J. Geophys. Res., 113, B5, 1-15, 10.1029/2007JB005277.

Schmittbuhl J., Chambon, G., Hansen, A., and M. Bouchon (2006), Are stress distributions along faults the signature of asperity squeeze?: Geophysical Research Letters, 33, 1-5.

Schock, R.N., Bonner, B.P., and H. Louis (1974), Collection of ultrasonic velocity data as function of pressure for polycrystalline solids: Lawrence Livermore Laboratory, University of California, Livermore, CA. UCRL-51508.

Schoenberg, M. (1980), Elastic wave behavior across linear slip interfaces: Journal of Acoustical Society of America, 68, 1516- 1521.

Scholz, C.H. (2002), The mechanics of earthquakes and faulting 2nd edition: Cambridge University Press.

Scuderi, M.M., C. Marone, E. Tinti, G. Di Stefano, and C. Collettini (2016), Precursory changes in seismic velocity for the spectrum of earthquake failure modes, Nature Geoscience, 9, 695-700.

Selvadurai, A.P.S., and Yu, Q. (2005), Mechanics of a discontinuity in a geomaterial: Computers and Geotechnics, 32, 92-106.

Selvadurai, A.P.S. and A. Glowacki (2008), Permeability hysteresis of limestone during isotropic compression: Ground Water, 46, 113-119.

Selvadurai, A.P.S., Suvorov, A.P., and P.A. Selvadurai (2014), Thermo-hydro-mechanical processes in fractured rock formations during glacial advance: Geoscientific Model Development Discussions, 7, 7351-7394.

Selvadurai, P.A., and Glaser, S.D. (2012), Direct measurement of contact area and seismic stress along a sliding interface: Proceedings of 46th US Rock Mechanics

Geomechanics Symposium, Chicago, IL, American Rock Mechanics Association. ARMA 23-538.

Selvadurai, P.A., and Glaser, S.D. (2013), Experimental evidence of micromechanical processes that control localization of shear rupture nucleation: Proceedings of 47th US Rock Mechanics Geomechanics Symposium, San Francisco, CA, American Rock Mechanics Association. ARMA 13-639.

Selvadurai, P.A., and Glaser, S.D. (2015a), Laboratory-developed contact models controlling instability on frictional faults: Journal of Geophysical Research, 120, 4208-4236.

Selvadurai, P.A., and Glaser, S.D. (2015b), Novel monitoring techniques for characterizing frictional interfaces in the laboratory: Sensors, 15, 9791-9814.

Shao, S., Petrovitch, C.L., and L.J. Pyrak-Nolte (2015), Wave guiding in fractured layered media, from Fundamental Controls on Fluid Flow in Carbonates: Current Workflows to Emerging Technologies, editors S.M. Agar and S. Geiger, Geological Society, London Special Publication, 406, 375-400.

Shao, S., and L.J. Pyrak-Nolte (2013), Interface waves along fractures in anisotropic media: GEOPHYSICS, 78, 4, T99-T112.

Silver, P.G., Daley, T.M., Niu, F., and E.L. Majer (2007), Active source monitoring of crosswell seismic travel time for stress induced changes: Bulletin of the Seismological Society of America, 97, 281-293.

Simmons, G., and W.F. Brace (1965), Comparison of static and dynamic measurements of compressibility of rocks: Journal of Geophysical Research, 70, 22, 5649-5656.

Spangler, L. (2014), Big Sky Carbon Sequestration Partnership – Phase III quarterly progress report, Submitted to: William Aljoe, National Energy Technology Laboratory, Morgantown, WV.

Spencer, J.W. (1981), Stress relaxations at low frequencies in fluid-saturated rocks: attenuation and modulus dispersion: Journal of Geophysical Research, 86, 1803-1812.

Storn, R. and K. Price (1997), Differential evolution–a simple and efficient heuristic for global optimization over continuous spaces, Journal of global optimization, 11, 4, 341-359.

Streltsova, T.D. (1983), Well pressure behavior of a naturally fractured reservoir: Society of Petroleum Engineers Journal, 23, 769-780.

Stribeck, R. (1902), Die wesentlichen eigenschaften der gleit- und rollenlager – The key qualities of sliding and roller bearings, Zeitschrift des Vereines Seutscher Ingenieure, 48, 38-39, 1342-1348, 1432-1437.

Subramaniyan, S., Quintal, B., Tisato, N., Saenger, E.H., and C. Madonna (2014), An overview of laboratory apparatuses to measure seismic attenuation in reservoir rocks: Geophysical Prospecting, 1-13.

Timoshenko, S. and J.N. Goodier (1951), Theory of Elasticity 2nd edition: McGraw-Hill Book Company.

Tisato, N., Quintal, B., Chapman, S., Madonna, C., Subramaniyan, S., Frehner, M., Saenger, E.H., and G. Grasselli (2014), Seismic attenuation in partially saturated rocks: Recent advances and future directions: The Leading Edge, 33, 640-646.

Tisato, N., and C. Madonna (2012), Attenuation at low seismic frequencies in partially saturated rocks: Measurement and description of a new apparatus: Journal of Applied Geophysics, 86, 44-53.

Trimmer, D., Bonner, B., Heard, H.C., and A. Duba (1980), Effect of pressure and stress on water transport in intact and fractured gabbro and granite: Journal of Geophysical Research, 85, B12, 7059–7071.

Vakhnenko, O., V. Vakhnenko, and T. Shankland (2005), Soft-ratchet modeling of end-point memory in the nonlinear resonant response of sedimentary rocks, Phys. Rev. B, 71, 174103.

van der Elst, N.J., and H.M. Savage (2015), Frequency dependence of delayed and instantaneous triggering on laboratory and simulated faults governed by rate-state friction, J. Geophys. Res. Solid Earth, 120, 3406–3429, doi:10.1002/2014JB011611

van der Elst, N.J., A.A. Delorey, D.R. Shelly, and P.A. Johnson (2016), Fortnightly modulation of San Andreas tremor and low-frequency earthquakes, PNAS, 113, 31, 8601-8605, doi: 10.1073/pnas.1524316113.

Vanorio, T., Prasad, M., Patella, D. and A. Nur (2002), Ultrasonic velocity measurements in volcanic rocks: correlation with microtexture: Geophysics Journal International, 149, 22-36.

Vialle, S. and T. Vanorio (2011), Laboratory measurements of elastic properties of carbonate rocks during injection of reactive CO_2-saturated water: Geophysical Research Letters, 38, 1-5.

Voisin, C. (2001), Dynamic triggering of earthquakes: the linear slip-dependent friction case: Geophysical Research Letters, 28, 17, 3357-3360.

Voisin, C. (2002), Dynamic triggering of earthquakes: The nonlinear slip-dependent friction case, J. Geophys. Res., 107(B12), 2356, doi:10.1029/2001JB001121.

Walsh, J.B. (1966), Seismic wave attenuation in rocks due to friction, J. Geophys. Res., 71, 2591–2599

White, J.E. (1966), Static friction as a source of seismic attenuation, Geophysics, 31, 333–339

Willis, M.E., Burns, D.R., Rao, R., Minsely, B., Toksoz, M.N., and L. Vetri (2006), Spatial orientation and distribution of reservoir fractures from scattered seismic energy: GEOPHYSICS, 71, O43-O51.

Winkler, K., Nur, A., and M. Gladwin (1979), Friction and seismic attenuation in rocks, Nature, 277, 528-531.

Winkler, K.W., and A. Nur (1979), Pore fluids and seismic attenuation in rocks: Geophysical Research Letters, 6, 1-4.

Winkler, K.W., and T.J. Plona (1982), Technique for measuring ultrasonic velocity and attenuation spectra in rocks under pressure: Journal of Geophysical Research, 87, 10776-10780.

Worthington, M.H. and R. Lubbe (2007), The scaling of fracture compliance: Fractured Reservoirs, Geological Society of London Special Publication, 270.

Wu, R.S. (1982), Attenuation of short period seismic waves due to scattering, Geophysical Research Letters, 9, 9-12.

Yee, A.F., and M.T. Takemori (1982), Dynamic bulk and shear relaxation in glassy polymers. I. Experimental techniques and results on PMMA: Journal of Polymer Science, Part B, 20, 205–224.

Yoshioka, N. (1997), A review of the micromechanical approach to the physics of contacting surfaces: Tectonophysics, 277, 29-40.

Zemanek, J.J. and I. Rudnick (1961), Attenuation and dispersion of elastic waves in a cylindrical bar: Journal of the Acoustical Society of America, 33, 1283-1288.

Zener, C. (1948), Elasticity and anelasticity of metals: University of Chicago Press.

Zhou, Q., Oldenburg, C.M., Spycher, N., Pan, L., and A. Cihan (2013), Summary of site characterization, data collection and review, development of static geologic model, and preliminary multiphase flow and reactive transport modeling activities: Lawrence Berkeley National Laboratory Deliverable to the Big Sky Carbon Sequestration Partnership: Milestone Report.

Zoback, M. and J. Byerlee (1975), The effect of micro-crack dilatancy on the permeability of westerly granite: Journal of Geophysical Research, 80, 752-755.